

Numerical Relativity and Compact Binaries

Thomas W. Baumgarte^{a,b} and Stuart L. Shapiro^{b,c}

^a*Department of Physics and Astronomy, Bowdoin College, Brunswick, ME 04011*

^b*Department of Physics, University of Illinois at Urbana-Champaign, Urbana, IL 61820*

^c*Department of Astronomy and NCSA, University of Illinois at Urbana-Champaign, Urbana, IL 61820*

Abstract

Numerical relativity is the most promising tool for theoretically modeling the inspiral and coalescence of neutron star and black hole binaries, which, in turn, are among the most promising sources of gravitational radiation for future detection by gravitational wave observatories. In this article we review numerical relativity approaches to modeling compact binaries. Starting with a brief introduction to the 3+1 decomposition of Einstein's equations, we discuss important components of numerical relativity, including the initial data problem, reformulations of Einstein's equations, coordinate conditions, and strategies for locating and handling black holes on numerical grids. We focus on those approaches which currently seem most relevant for the compact binary problem. We then outline how these methods are used to model binary neutron stars and black holes, and review the current status of inspiral and coalescence simulations.

Key words:

Contents

1	Introduction	3
2	Decomposing Einstein's Equations	6
2.1	Foliations of Spacetime	6
2.2	The ADM equations	10
2.3	Electrodynamics	15
2.4	An Illustration in Spherical Symmetry	16
3	Constructing Initial Data	18

3.1	Conformal Decompositions	18
3.2	The Conformal Transverse-Traceless Decomposition	20
3.3	The Thin-Sandwich Decomposition	23
4	Rewriting the ADM evolution equations	26
4.1	Rewriting Maxwell's equations	27
4.2	Hyperbolic formulations	29
4.3	The BSSN formulation	32
5	Choosing Coordinates	37
5.1	Geodesic Slicing	38
5.2	Maximal Slicing	39
5.3	Harmonic Coordinates and Variations	41
5.4	Minimal Distortion and Variations	44
6	Locating Black Hole Horizons	48
6.1	Locating Apparent Horizons	49
6.2	Locating Event Horizons	55
7	Binary Black Hole Initial Data	57
7.1	The Bowen-York Approach	58
7.2	The Thin-Sandwich Approach	64
7.3	Comparison and Discussion	66
8	Dynamical Simulations of Binary Black Holes	68
8.1	Singularity Avoidance and Black Hole Excision	68
8.2	Evolution of Binary Black Holes	74
9	Binary Neutron Star Initial Data	77
9.1	Hydrostatic Quasi-Equilibrium	77
9.2	Corotational Binaries	81

9.3	Irrotational Binaries	85
10	Dynamical Simulations of Binary Neutron Stars	91
10.1	Relativistic Hydrodynamics	91
10.2	The Wilson-Mathews approximation	96
10.3	Fully Self-consistent Simulations	97
10.4	The Quasi-Adiabatic Inspiral of Binary Neutron Stars	103
11	Summary and Outlook	106
	Acknowledgements	108
A	Notation	108
B	Solving the Vector Laplacian	109
C	Conformally Flat or Not?	111

1 Introduction

Promising to open a new window to the universe, a new generation of laser interferometer gravitational wave detectors will soon search for gravitational radiation. The Japanese instrument TAMA is already in operation (Tagoshi *et.al.*, 2001), and the construction of the two LIGO sites in the US and the European instruments GEO and VIRGO is well advanced. Among the most promising sources for these detectors are the inspiral and merger of compact binaries, i.e. binaries of black holes and neutron stars. Even for these sources, the signal strength is expected to be much less than the detectors' noise, so that sophisticated data analysis techniques will be required to extract the signal from the noise (e.g. Cutler *et.al.* (1993)). One such technique is matched filtering, in which the detector output is cross-correlated with a catalog of theoretically predicted waveforms. The cross-correlation between a signal present in the data and a member of the catalog allows observers to detect signals that are otherwise overwhelmed by noise. Clearly, the chances of detecting a generic astrophysical signal depend critically on the size and quality of the signal catalog (Flanagan and Hughes, 1998). The success of the new gravitational wave interferometers therefore depends on accurate theoretical models of compact binary inspiral.

For our purposes, the entire inspiral of compact binaries can be separated into three different phases. By far the longest phase is the initial quasi-equilibrium

inspiral phase, during which the separation between the stars decreases adiabatically as energy is carried away by gravitational radiation. As the separation decreases, the frequency and amplitude of the emitted gravitational radiation increases. Since gravitational radiation tends to circularize binary orbits, and since we will be mostly interested in binaries at very small separation, it is reasonable to focus on quasi-circular orbits. These quasi-circular orbits become unstable at the innermost stable circular orbit (ISCO), where the inspiral gradually enters a *plunge and merger* phase. The merger and coalescence of the stars happens on a dynamical timescale. The final stage of the evolution is the *ringdown* phase, during which the merged object settles down to equilibrium.

Different techniques are commonly employed to model the binary in the different phases. The early inspiral phase, for large binary separations, can be modeled very accurately with post-Newtonian methods (Blanchet *et.al.*, 1995; Damour, Jaranowski and Schäfer, 2000, and references therein). It is generally accepted that the plunge and merger phase has to be simulated by means of a fully self-consistent numerical relativity simulation. During the late ringdown phase, the merged object can be approximated as a distorted equilibrium object, so that perturbative techniques can be applied (Price and Pullin, 1994; Baker *et.al.*, 2001, 2002). In addition to simulating the dynamical plunge and merger phase, numerical relativity may also be required for the late quasi-adiabatic inspiral phase, just outside of the ISCO, where finite-size and relativistic effects may become large enough for post-Newtonian point-mass techniques to break down.

A number of review articles have recently appeared on various aspects of numerical relativity, including Lehner (2001) on numerical relativity in general, Cook (2000) on initial data, Martí and Müller (1999) and Font (2000) on numerical hydrodynamics in special and general relativity, Rasio and Shapiro (1999) on the coalescence of binary neutron stars, Reula (1998) on hyperbolic methods of Einstein's equations, and New (2002) on the generation of gravitational waves from gravitational collapse. While we will refer to these articles in many places, the perspective and focus of this article is very different. It is intended as a review of different numerical relativity approaches to the compact binary problem, and we will focus on those methods of numerical relativity that currently seem most promising for these purposes. Specifically, we will only discuss the so-called Cauchy approach in “3+1”, i.e. three spatial dimensions (“3D”) plus time¹, and we limit matter sources, if present, to perfect fluids. This means that many other promising techniques and important results of numerical relativity will not be covered, including characteristic

¹ We will provide examples of spherically symmetric configurations to illustrate concepts and techniques. These examples, which can be treated in 1+1 dimensions, are clearly marked and set in *italics*.

methods², collisionless matter and scalar wave sources, critical phenomena, and results in spherical or axisymmetry. Simultaneously, we will review numerical relativity approaches to the compact binary problem only, and will not discuss post-Newtonian or perturbative methods.

Even with this fairly focused scope of our article we will omit some important aspects. Perhaps most importantly, we will not cover wave extraction and boundary conditions for outer boundaries, since in most current applications in 3+1 these are only implemented fairly crudely. Some relevant references to more rigorous treatments include Bishop *et.al.* (1996); Abrahams *et.al.* (1998); Friedrich and Nagy (1999); Szilagyi *et.al.* (2000); Calabrese, Lehner and Tiglio (2002); Szilagyi, Schmidt and Winicour (2002). While we will cast equations into a form that is suitable for numerical implementation, we will hardly discuss numerical methods that can be used for their solution. We will similarly ignore related computer science issues, including memory and CPU requirements and computational resources on current parallel computers. Some discussion of these aspects and references can be found in Lehner (2001).

Loosely speaking, this article is organized into two parts. The first part, Sections 2 through 6, introduces concepts and techniques of numerical relativity, both traditional approaches and more recent developments. The second part, Sections 7 through 10, reviews their applications to binary black holes and neutron stars.

The first part starts by introducing the 3 + 1 decomposition and the so-called ADM equations in Section 2. We will see that, like Maxwell's equations, these equations separate into constraint and evolution equations. In Section 3 we discuss strategies for solving the constraint equations and the construction of initial data. In Section 4 we will revisit the ADM equations, and will show that the evolution equations can be brought into a form that is better suited for numerical integrations. Before these evolution equations can be integrated, certain coordinate conditions have to be imposed, which we will discuss in Section 5. In Section 6 we review the definition of black hole horizons, and show how these horizons can be located in numerically generated spacetimes.

In the second part we discuss the construction of binary black holes and neutron stars. Specifically, we review the initial data problem and evolution simulations of binary black holes in Sections 7 and 8 and binary neutron stars in Sections 9 and 10. We briefly summarize in Section 11.

Also included are three short appendixes. Appendix A explains our notation, Appendix B shows how the flat vector Laplace operator, which is encountered in several places in this article, can be solved, and Appendix C discusses some

² Which in fact may be a very promising alternative to the Cauchy approach even for the modeling of compact binaries; see, e.g. Gomez *et.al.* (1998).

arguments which have been made in favor or against the approximation of spatial conformal flatness.

As a last remark we would like to apologize to all those authors and colleagues whose publications we may have missed. While we have put considerable effort into being as complete as possible, without doubt we have missed some important references. We again apologize for these unintended omissions.

2 Decomposing Einstein's Equations

In this Section we briefly summarize the Arnowitt-Deser-Misner or “ADM” decomposition of Einstein's equations. We will state only the most important relations and results and refer to the literature for more complete and rigorous treatments. In addition to the original article by Arnowitt, Deser and Misner (1962) such presentations can be found, for example, in the article by York (1979), the dissertations by Smarr (1975), Evans (1984) and Cook (1990), and in the lecture notes of Baumgarte, Shapiro and Abrahams (1998).

2.1 *Foliations of Spacetime*

The unification of space and time into spacetime is central to general relativity and is one of its greatest aesthetic appeals. For a numerical treatment, however, and similarly for many mathematical treatments, it is more desirable to reverse this unification and recast general relativity into a so-called “3+1” formulation, in which a time coordinate is explicitly split from three spatial coordinates. Putting it differently, the four-dimensional spacetime is “carved up” into a family of three-dimensional spatial “slices”.

In more technical terms, we assume that the spacetime (M, g_{ab}) can be foliated into a family of non-intersecting, spacelike, three-dimensional hypersurfaces Σ . At least locally, these timeslices Σ form level surfaces of a scalar function t , which we will later identify with the coordinate time. The 1-form

$$\Omega = dt \tag{2.1}$$

is obviously closed ($d\Omega = 0$) and has the norm

$$|\Omega|^2 = g^{ab} \nabla_a t \nabla_b t \equiv -\alpha^{-2}, \tag{2.2}$$

where the *lapse function* α is strictly positive (see Appendix A for a summary

of our notation). This implies that the surfaces Σ are spacelike. We now define the timelike unit normal vector n^a as

$$n^a \equiv -\alpha g^{ab} \Omega_b = -\alpha g^{ab} \nabla_b t. \quad (2.3)$$

Here the negative sign has been chosen so that n^a points into the direction of increasing t . The four-dimensional metric g_{ab} now induces the *spatial metric*

$$\gamma_{ab} \equiv g_{ab} + n_a n_b \quad (2.4)$$

on the hypersurfaces Σ .

Any four-dimensional tensor can now be decomposed into spatial parts, which live in the hypersurfaces Σ , and timelike parts, which are normal to Σ and hence aligned with n^a . The spatial part can be found by contracting with the projection operator

$$\gamma^a_b = g^{ac} \gamma_{cb} = g^a_b + n^a n_b = \delta^a_b + n^a n_b, \quad (2.5)$$

and the timelike part by contracting with

$$N^a_b = -n^a n_b. \quad (2.6)$$

We now define the three-dimensional covariant derivative of a spatial tensor by projecting all indices of a four-dimensional covariant derivative into Σ ; for example

$$D_a T^b_c \equiv \gamma_a^d \gamma_e^b \gamma_c^f \nabla_d T^e_f. \quad (2.7)$$

It is easy to show that this derivative is compatible with the spatial metric, $D_a \gamma_{bc} = 0$, as it is supposed to be. The three-dimensional covariant derivative can be expressed in terms of three-dimensional connection coefficients, which, in a coordinate basis, are given by

$$\Gamma^a_{bc} = \frac{1}{2} \gamma^{ad} (\gamma_{db,c} + \gamma_{dc,b} - \gamma_{bc,d}). \quad (2.8)$$

The three-dimensional Riemann tensor associated with γ_{ij} is defined by requiring that

$$2D_{[a} D_{b]} w_c = R^d_{cba} w_d \quad R^d_{cba} n_d = 0 \quad (2.9)$$

for every spatial w_d . In terms of coordinate components, Riemann can be computed from

$$R_{abc}{}^d = \Gamma_{ac,b}^d - \Gamma_{bc,a}^d + \Gamma_{ac}^e \Gamma_{eb}^d - \Gamma_{bc}^e \Gamma_{ea}^d. \quad (2.10)$$

Contracting the Riemann tensor yields the three-dimensional Ricci tensor $R_{ab} = R^c{}_{acb}$ and the three-dimensional scalar curvature $R = R^a{}_a$.

It is intuitive that casting Einstein's equations into a $3 + 1$ form will necessitate expressing the four-dimensional Riemann tensor ${}^{(4)}R_{abc}^d$ in terms its three-dimensional cousin R_{abc}^d . It is also clear, however, that the latter cannot contain all the relevant information: R_{abc}^d is a purely spatial object (and can be computed from spatial derivatives of the spatial metric alone), while ${}^{(4)}R_{abc}^d$ is a spacetime creature which also contains time-derivatives of the four-dimensional metric. This missing information is expressed by a tensor called *extrinsic curvature*, which describes how the slice Σ is embedded in the spacetime M . The extrinsic curvature can be defined as

$$K_{ab} \equiv -\gamma_a{}^c \gamma_b{}^d \nabla_{(c} n_{d)}. \quad (2.11)$$

Note that K_{ab} is spatial and symmetric by construction. An alternative expression can be found in terms of the “acceleration” of normal observers $a_a = n^b \nabla_b n_a$,

$$K_{ab} = -\nabla_a n_b - n_a a_b. \quad (2.12)$$

Since $a^a n_a = 0$, we immediately find for the trace of the extrinsic curvature

$$K \equiv g^{ab} K_{ab} = -\nabla^a n_a. \quad (2.13)$$

In yet another equivalent expression, the extrinsic curvature can be written in terms of the Lie derivative of the spatial metric along the normal vector n^a

$$K_{ab} = -\frac{1}{2} \mathcal{L}_n \gamma_{ab}. \quad (2.14)$$

The Lie derivative in the above equation may be thought of as the geometric generalization of the partial time derivative ∂_t . Introductions to the Lie derivative can be found, for example, in Schutz (1980); Wald (1984); D’Inverno (1992); Baumgarte, Shapiro and Abrahams (1998). Formally, the Lie derivative along a vector field X^a measures by how much the changes in a tensor field along X^a differ from a mere infinitesimal coordinate transformation generated

by X^a . For a scalar f , the Lie derivative reduces to the partial derivative

$$\mathcal{L}_{\mathbf{X}}f = X^b D_b f = X^b \partial_b f; \quad (2.15)$$

for a vector field v^a the Lie derivative is the commutator

$$\mathcal{L}_{\mathbf{X}}v^a = X^b D_b v^a - v^b D_b X^a = [X, v]^a, \quad (2.16)$$

and for a 1-form ω_a the Lie derivative is given by

$$\mathcal{L}_{\mathbf{X}}\omega_a = X^b D_b \omega_a + \omega_b D_a X^b. \quad (2.17)$$

It then follows that for a tensor T^a_b of rank $\binom{1}{1}$ the Lie derivative is

$$\mathcal{L}_{\mathbf{X}}T^a_b = X^c \partial_c T^a_b - T^c_b \partial_c X^a + T^a_c \partial_b X^c. \quad (2.18)$$

Generalization to tensors of arbitrary rank follows naturally. It is easy to verify that in all of the above expressions for the Lie derivative one may replace the partial derivative with a covariant derivative, since all connection coefficients cancel each other.

Equation (2.14) most clearly illustrates the interpretation of K_{ab} as a time-derivative of the spatial metric. It is therefore not surprising that spatial projections of ${}^{(4)}R^a_{bcd}$ will involve the extrinsic curvature and its time derivative.

Given its symmetry properties, ${}^{(4)}R^a_{bcd}$ can be projected in three different ways. Projecting all four indices into Σ yields, after some manipulations, *Gauss' equation*,

$$R_{abcd} + K_{ac}K_{bd} - K_{ad}K_{bc} = \gamma^p_a \gamma^q_b \gamma^r_c \gamma^s_d {}^{(4)}R_{pqrs}. \quad (2.19)$$

Three spatial projections and a contraction with n^a yields the *Codazzi equation*

$$D_a K_{bc} - D_b K_{ac} = \gamma^r_b \gamma^p_a \gamma^q_c n^s {}^{(4)}R_{rpqs}. \quad (2.20)$$

Finally, two spatial projections and two contractions with n^a yield *Ricci's equation*

$$\mathcal{L}_{\mathbf{n}}K_{ab} = n^d n^c \gamma^q_a \gamma^r_b {}^{(4)}R_{rdqc} - \frac{1}{\alpha} D_a D_b \alpha - K^c_b K_{ac}. \quad (2.21)$$

In this equation the derivative of the lapse entered through the identity

$$a_a = D_a \ln \alpha. \quad (2.22)$$

2.2 The ADM equations

In the last Section we simply recorded geometrical identities relating the geometry of the three-dimensional hypersurfaces Σ to the geometry of the embedding four-dimensional spacetime M . According to general relativity, the geometry of the latter is governed dynamically by Einstein's equation

$${}^{(4)}G_{ab} \equiv {}^{(4)}R_{ab} - \frac{1}{2}{}^{(4)}R g_{ab} = 8\pi T_{ab}, \quad (2.23)$$

where ${}^{(4)}G_{ab}$ is the Einstein tensor and T_{ab} the stress-energy tensor. We will now take projections of Einstein's equations into Σ and n^a and will use the Gauss, Codazzi and Ricci equations to eliminate the four-dimensional Ricci tensor ${}^{(4)}R_{ab}$. The result will be the ADM equations, which relate three-dimensional curvature quantities to projections of the stress-energy tensor. One relation that is very useful in these derivations is

$$D_a V^b = \gamma_a^c \nabla_c V^b + K_{ac} V^c n^b, \quad (2.24)$$

which holds for any spatial vector V^a .

Contracting Gauss' equation (2.19) twice with the spatial metric and inserting (2.4) yields

$$2n^a n^b {}^{(4)}G_{ab} = R + K^2 - K_{ab} K^{ab}. \quad (2.25)$$

We now define the total energy density as measured by a normal observer n^a as

$$\rho \equiv n^a n^b T_{ab} \quad (2.26)$$

and, using Einstein's equation (2.23), find the *Hamiltonian constraint*

$$R + K^2 - K_{ab} K^{ab} = 16\pi\rho. \quad (2.27)$$

We can similarly contract the Codazzi equation (2.20) once to find the *momentum constraint*

$$D_b K^b_a - D_a K = 8\pi j_a, \quad (2.28)$$

where

$$j_a \equiv -\gamma_a^b n^c T_{bc} \quad (2.29)$$

is the momentum density (mass current) as measured by a normal observer n^a . The Hamiltonian and momentum constraints are called constraint equations because they only involve spatial quantities and their spatial derivatives. They therefore have to hold on each individual spatial slice Σ – in fact they are the necessary and sufficient integrability conditions for the embedding of the spatial slices $(\Sigma, \gamma_{ab}, K_{ab})$ in the spacetime (M, g_{ab}) .

Evolution equations that describe how data γ_{ab} and K_{ab} evolve in time, from one spatial slice to the next, can be found from equation (2.14) and the Ricci equation (2.21). However, the Lie derivative along n^a , \mathcal{L}_n , is not a natural time derivative orthogonal to the spatial slices, since n^a is not dual to the surface 1-form Ω , i.e. their dot product is not unity but rather

$$n^a \Omega_a = -\alpha g^{ab} \nabla_b t \nabla_a t = \alpha^{-1}. \quad (2.30)$$

Instead, the vector

$$t^a = \alpha n^a + \beta^a \quad (2.31)$$

is dual to Ω for any spatial *shift vector* β^a . The lapse α and the shift β^a together determine how the coordinates evolve from one slice Σ to the next. The lapse determines how much proper time elapses between timeslices along the normal vector n^a , while the shift determines by how much spatial coordinates are shifted with respect to the normal vector.

The Lie derivative along t^a is a natural time derivative, because the duality

$$t^a \Omega_a = t^a \nabla_a t = 1 \quad (2.32)$$

implies that the integral curves of t^a are naturally parametrized by t . As a consequence, all (infinitesimal) vectors t^a originating on one spatial slice Σ_1 will end on the same spatial slice Σ_2 (unlike the corresponding vectors n^a , which generally would end on different slices). This also implies that the Lie derivative of any spatial tensor along t^a is again spatial (see, e.g., Problem 8.14 in Lightman *et.al.* (1975) for an illustration).

Rewriting equation (2.14) in terms of t^a yields the evolution equation for the spatial metric

$$\mathcal{L}_t \gamma_{ab} = -2\alpha K_{ab} + \mathcal{L}_\beta \gamma_{ab}. \quad (2.33)$$

The evolution equation for the extrinsic curvature can be found by combining Ricci's equation (2.21) with Einstein's equations (2.23)

$$\begin{aligned}\mathcal{L}_t K_{ab} = & -D_a D_b \alpha + \alpha(R_{ab} - 2K_{ac}K^c_b + KK_{ab}) \\ & -\alpha 8\pi(S_{ab} - \tfrac{1}{2}\gamma_{ab}(S - \rho)) + \mathcal{L}_\beta K_{ab},\end{aligned}\tag{2.34}$$

where S_{ab} is the spatial projection of the stress-energy tensor

$$S_{ab} \equiv \gamma_{ac}\gamma_{bd}T^{cd},\tag{2.35}$$

and S its trace $S \equiv \gamma^{ab}S_{ab}$.

While the two constraint equations (2.27) and (2.28) constrain γ_{ab} and K_{ab} on every spatial slice Σ , the evolution equations (2.33) and (2.34) describe how these quantities evolve from one slice to the next. It can be shown that the evolution equations preserve the constraint equations, meaning that if the constraints hold on one slice, they will continue to hold on later slices. This structure is very similar to that of Maxwell's equations, as we will discuss in Section 2.3.

So far, we have made no assumptions about the choice of coordinates, and have expressed all quantities in a coordinate-independent way. It is quite intuitive, though, that things will simplify if we adopt a coordinate system that reflects our 3+1 split of spacetime. To do so, we introduce a basis of spatial vectors e_i (where $i = 1, 2, 3$, see Appendix A for a summary of our notation) that span each slice Σ , so that $\Omega_a(e_i)^a = 0$. It can be shown that this condition is preserved if the spatial vectors are Lie dragged along t^a . As the fourth basis vector we pick $(e_0)^a = t^a$, or, in components, $t^a = (1, 0, 0, 0)$. As an immediate consequence, the Lie derivative along t^a reduces to a partial derivative with respect to t . Since $n_i = n_a(e_i)^a = \alpha\Omega_a(e_i)^a = 0$, the covariant, spatial components of the normal vector vanish. Since contractions of any spatial tensor with the normal vector are zero, this implies that the zeroth components of contravariant spatial tensors have to vanish. For the shift vector, for example, $\beta^a n_a = \beta^0 n_0 = 0$, so that we can write

$$\beta^a = (0, \beta^i).\tag{2.36}$$

Solving (2.31) for n^a then yields the contravariant components of the shift vector

$$n^a = \frac{1}{\alpha}(1, -\beta^i)\tag{2.37}$$

and, since $n^a n_a = -1$,

$$n_a = (-\alpha, 0, 0, 0). \quad (2.38)$$

From the definition of the spatial metric (2.4) we find $\gamma_{ij} = g_{ij}$. Since zeroth components of contravariant, spatial tensors are zero, we also have $\gamma^{a0} = 0$. The inverse metric can therefore be expressed as

$$g^{ab} = \begin{pmatrix} -\alpha^{-2} & \alpha^{-2}\beta^i \\ \alpha^{-2}\beta^j & \gamma^{ij} - \alpha^{-2}\beta^i\beta^j \end{pmatrix} \quad (2.39)$$

Using $n_i = 0$, $\gamma_{ij} = g_{ij}$ and $\gamma^{a0} = 0$ it is also possible to show that γ_{ij} and γ^{ij} are inverses $\gamma^{ik}\gamma_{kj} = \delta^i_j$, so that they can be used to raise and lower indices of spatial tensors. Inverting (2.39) we find the components of the four-dimensional metric

$$g_{ab} = \begin{pmatrix} -\alpha^2 + \beta_k\beta^k & \beta_i \\ \beta_j & \gamma_{ij} \end{pmatrix} \quad (2.40)$$

and equivalently the line element

$$ds^2 = -\alpha^2 dt^2 + \gamma_{ij}(dx^i + \beta^i dt)(dx^j + \beta^j dt). \quad (2.41)$$

The entire content of a spatial tensor is encoded in its spatial components alone. We can therefore restrict the constraint and evolution equations to spatial components. Moreover, since in our coordinate system the zeroth components of contravariant, spatial tensors are zero, we can also restrict all contractions to spatial components. The connection coefficients (2.8) reduce to

$$\Gamma_{jk}^i = \frac{1}{2}\gamma^{il}(\gamma_{lj,k} + \gamma_{lk,j} - \gamma_{jk,l}), \quad (2.42)$$

and expressing the Ricci tensor (2.10) in terms of second derivatives of the metric yields

$$R_{ij} = \frac{1}{2}\gamma^{kl}(\gamma_{kj,il} + \gamma_{il,kj} - \gamma_{kl,ij} - \gamma_{ij,kl}) \\ + \gamma^{kl}(\Gamma_{il}^m \Gamma_{mkj} - \Gamma_{ij}^m \Gamma_{mkl}) \quad (2.43)$$

With these simplifications, the Hamiltonian constraint (2.27) now becomes

$$R + K^2 - K_{ij}K^{ij} = 16\pi\rho, \quad (2.44)$$

the momentum constraint

$$D_j K^j_i - D_i K = 8\pi j_i, \quad (2.45)$$

the evolution equation for the spatial metric (2.33)

$$\partial_t \gamma_{ij} = -2\alpha K_{ij} + D_i \beta_j + D_j \beta_i, \quad (2.46)$$

and the evolution equation for the extrinsic curvature (2.34)

$$\begin{aligned} \partial_t K_{ij} = & -D_i D_j \alpha + \alpha (R_{ij} - 2K_{ik} K^k_j + K K_{ij}) \\ & - \alpha 8\pi (S_{ij} - \frac{1}{2} \gamma_{ij} (S - \rho)) \\ & + \beta^k D_k K_{ij} + K_{ik} D_j \beta^k + K_{kj} D_i \beta^k. \end{aligned} \quad (2.47)$$

The shift terms in the last two equations arise from the Lie derivatives $\mathcal{L}_\beta \gamma_{ij}$ and $\mathcal{L}_\beta K_{ij}$. In (2.46) it is convenient to express the Lie derivative in terms of the covariant derivative D_i which eliminates the term $\beta^k D_k \gamma_{ij}$, but in (2.47) the covariant derivative may be replaced with the partial derivative ∂_i in these terms.

Equations (2.44) to (2.47) are commonly referred to as the ADM equations³. As it turns out, these equations are not yet in a form that is generally well suited for numerical implementation. In Section 4 we will see that the stability properties of numerical implementations can be improved by introducing certain new auxiliary functions and rewriting the ADM equations in terms of these functions. Most current numerical relativity codes are based on such reformulations of the ADM equation.

Note that the ADM equations only determine the spatial metric γ_{ij} and the extrinsic curvature K_{ij} , but not the lapse α or the shift β^i . The latter determine how the coordinates evolve from one timeslice to the next and reflect the coordinate freedom of general relativity. Choosing coordinates that are suitable for the situation that one wishes to simulate is central to the success of the simulation. In Section 5 we will discuss strategies for both choosing and numerically implementing various coordinate conditions.

For later purposes it is useful to take the traces of the evolution equations (2.46) and (2.47). Since $\partial_t \ln \gamma = \gamma^{ij} \partial_t \gamma_{ij}$, we find

$$\partial_t \ln \gamma^{1/2} = -\alpha K + D_i \beta^i, \quad (2.48)$$

³ Arnowitt, Deser and Misner (1962) originally derived these equations in terms of the conjugate momenta π_{ij} instead of the extrinsic curvature.

for the determinant of the metric γ , and combining the Hamiltonian constraint (2.44) with the trace of (2.47) yields

$$\partial_t K = -D^2 \alpha + \alpha \left(K_{ij} K^{ij} + 4\pi(\rho + S) \right) + \beta^i D_i K. \quad (2.49)$$

Here $D^2 \equiv \gamma^{ij} D_i D_j$ is the covariant Laplace operator associated with γ_{ij} .

2.3 Electrodynamics

To discuss the structure of the ADM equations it is very instructive to compare them to the equations of electrodynamics. Maxwell's equations in flat space naturally split into a set of *constraint* equations

$$D_i E^i = 4\pi \rho_e \quad (2.50)$$

$$D_i B^i = 0 \quad (2.51)$$

which hold at each instant of time, and a set of *evolution* equations

$$\partial_t E_i = \epsilon_{ijk} D^j B^k - 4\pi J_i \quad (2.52)$$

$$\partial_t B_i = -\epsilon_{ijk} D^j E^k \quad (2.53)$$

which describe the evolution of the electric field E_i and the magnetic field B_i from one instant of time to the next. Here ρ_e and J_i are the charge density and current. Note that the evolution equations preserve the constraints so that, if they are satisfied at any time, they are automatically satisfied at all times.

It is often useful to introduce the vector potential $A_a = (-\Phi, A_i)$ and write B^i as a curl of A_i

$$B^i = \epsilon^{ijk} D_j A_k \quad (2.54)$$

so that B^i satisfies the constraint (2.51) automatically. Maxwell's equations can now be rewritten as two evolution equations for A_i and E_i

$$\partial_t A_i = -E_i - D_i \Phi \quad (2.55)$$

$$\partial_t E_i = -D^j D_j A_i + D_i D^j A_j - 4\pi J_i \quad (2.56)$$

together with the constraint equation (2.50) (see, e.g., Jackson (1975)). The gauge quantity Φ is, like the lapse and shift in the ADM equations, undetermined by the equations, and has to be chosen independently.

Interestingly, the evolution equations (2.55) and (2.56) are quite similar to the ADM evolution equations (2.46) and (2.47), which can be seen by identifying A_i with γ_{ij} and E_i with K_{ij} . Both right hand sides of (2.46) and (2.55) involve a field variable and a derivative of a gauge variable, while both right hand sides of (2.47) and (2.56) involve matter sources as well as second derivatives of the second field variable (which in (2.47) are hidden in the Ricci tensor (2.43)). In Section 4.1 we will further explore these similarities.

2.4 An Illustration in Spherical Symmetry

To illustrate the concepts introduced in this Section, it is useful to work out some of the expressions in spherical symmetry. Throughout this Article we will return to this example.

Example 2.1 *The general form of a spherically symmetric spacetime metric is*

$$ds^2 = -Adt^2 + 2Bdtdr + Cdr^2 + D(d\theta^2 + \sin^2\theta d\phi^2), \quad (2.57)$$

where the coefficients A , B , C and D are functions of time t and radius r only (see, e.g., equation (14.29) in D’Inverno (1992)). We now introduce a new radial coordinate by the transformation

$$r \rightarrow \tilde{r} = (D/C)^{1/2}, \quad (2.58)$$

which, after dropping all tildes, brings the metric into the isotropic form

$$ds^2 = -Adt^2 + 2Bdtdr + C(dr^2 + r^2 d^2\Omega), \quad (2.59)$$

where $d^2\Omega = d\theta^2 + \sin^2\theta d\phi^2$. Comparing with the metric (2.41), we can now identify B with β_r and, since β^r has to be the only non-vanishing component of the shift vector, A with $\alpha^2 - \beta_r\beta^r$. Following convention, we will also rewrite C as ψ^4 , where ψ is called the “conformal factor” (compare Section 3). Defining β as the contravariant component β^r , we have

$$ds^2 = -(\alpha^2 - \psi^4\beta^2)dt^2 + 2\psi^4\beta drdt + \psi^4(dr^2 + r^2 d^2\Omega). \quad (2.60)$$

The only non-vanishing, spatial connection coefficients can now be found to be

$$\begin{aligned}
\Gamma_{rr}^r &= 2\frac{\psi'}{\psi} & \Gamma_{\theta\theta}^r &= -2\frac{r^2\psi'}{\psi} - r \\
\Gamma_{\phi\phi}^r &= \sin^2\theta\Gamma_{\theta\theta}^r & \Gamma_{\phi\phi}^\theta &= -\sin\theta\cos\theta \\
\Gamma_{r\theta}^\theta &= \Gamma_{\theta r}^\theta = \Gamma_{r\phi}^\phi = \Gamma_{\phi r}^\phi = 2\frac{\psi'}{\psi} + \frac{1}{r} & \Gamma_{\theta\phi}^\phi &= \Gamma_{\phi\theta}^\phi = \cot\theta.
\end{aligned} \tag{2.61}$$

Here and in all following examples a prime denotes partial derivative with respect to radius r , and a dot will denote partial derivative with respect to time t . As expected, the connection reduces to that of a flat metric in spherical symmetry for $\psi = 1$. The non-vanishing components of the extrinsic curvature can be computed from equation (2.46) according to

$$\begin{aligned}
K_r^r &= -\frac{2}{\alpha} \left(\frac{\dot{\psi}}{\psi} - \beta \frac{\psi'}{\psi} - \frac{\beta'}{2} \right) \\
K_\theta^\theta &= K_\phi^\phi = -\frac{2}{\alpha} \left(\frac{\dot{\psi}}{\psi} - \beta \frac{\psi'}{\psi} - \frac{\beta}{2r} \right),
\end{aligned} \tag{2.62}$$

and the trace of the extrinsic curvature is

$$\alpha K = -\frac{6}{\psi}(\dot{\psi} - \beta\psi') + \frac{1}{r^2}(\beta r^2)'. \tag{2.63}$$

Note that subtracting the two equations in (2.62) yields an equation for the shift

$$r\beta' - \beta = \alpha(K_r^r - K_\theta^\theta)r \tag{2.64}$$

which can be integrated to yield

$$\beta = r \int \frac{\alpha(K_r^r - K_\theta^\theta)}{r} dr. \tag{2.65}$$

It may seem surprising that we find an equation for the shift, even though we have emphasized on several occasions that Einstein's equations do not determine the lapse and the shift, and that, representing the coordinate freedom in general relativity, they have to be chosen independently. However, we have already used up the spatial coordinate freedom in equation (2.58), by bringing the metric into the isotropic form (2.60). The shift condition (2.65) ensures that the metric remains isotropic for all times, and it can therefore no longer be chosen freely. The lapse, however, is still undetermined.

One could carry the exercise further, and derive, for example, the Ricci tensor R_{ij} from the connection (2.61), which would be straight-forward but quite lengthy. Instead we will postpone this until we develop a formalism in Section 3 that will simplify this exercise significantly.

3 Constructing Initial Data

In this Section we will present strategies for solving the constraint equations (2.44) and (2.45). Since a review of the initial value problem for numerical relativity has appeared very recently (Cook, 2000), we will focus only on the the most important results that are often employed for the construction of binary black holes and neutron stars. In this Section we will review the most common formalisms, and will defer the discussion of particular solutions for binary black holes and neutron stars to Sections 7 and 9. Parts of this Section are based on the lecture notes of Baumgarte, Shapiro and Abrahams (1998).

3.1 Conformal Decompositions

Most approaches to solving the relativistic initial value problem involve a conformal decomposition, in which the physical metric γ_{ij} is written as a product of a *conformal factor* ψ and an auxiliary metric, usually referred to as the *conformally related* or *background metric* $\bar{\gamma}_{ij}$,

$$\gamma_{ij} = \psi^4 \bar{\gamma}_{ij} \tag{3.1}$$

(Lichnerowicz, 1944; York, 1971, 1972). Taking ψ to the fourth power turns out to be convenient, but is otherwise arbitrary. For other purposes it is advantageous to consider conformal transformations of the four-dimensional space-time metric g_{ab} , but here we will only consider conformal transformations of the spatial metric γ_{ij} .

Superficially, we can think of the decomposition (3.1) as a mathematical trick, namely writing one unknown as a product of two unknowns, which makes the solving of some equations a little easier. At a deeper level, the conformal transformation (3.1) defines an equivalence class of manifolds and metrics, which are all related by the *conformal metric* $\bar{\gamma}_{ij} = \gamma^{-1/3} \gamma_{ij}$, where γ is the determinant of the metric γ_{ij} . In this natural definition $\bar{\gamma} = 1$, but other normalizations can be chosen. A metric that is conformally related to the flat spatial metric, $\gamma_{ij} = \psi^4 \eta_{ij}$, is called *conformally flat*.

From (3.1), the connection coefficients transform according to

$$\Gamma_{jk}^i = \bar{\Gamma}_{jk}^i + 2(\delta_j^i \partial_k \ln \psi + \delta_k^i \partial_j \ln \psi - \bar{\gamma}_{jk} \bar{\gamma}^{il} \partial_l \ln \psi), \quad (3.2)$$

from which it is easy to verify that $\bar{D}_k \bar{\gamma}_{ij} = 0$. For the Ricci tensor (2.43) we find

$$\begin{aligned} R_{ij} = \bar{R}_{ij} - 2 \left(\bar{D}_i \bar{D}_j \ln \psi + \bar{\gamma}_{ij} \bar{\gamma}^{lm} \bar{D}_l \bar{D}_m \ln \psi \right) \\ + 4 \left((\bar{D}_i \ln \psi)(\bar{D}_j \ln \psi) - \bar{\gamma}_{ij} \bar{\gamma}^{lm} (\bar{D}_l \ln \psi)(\bar{D}_m \ln \psi) \right), \end{aligned} \quad (3.3)$$

and for the curvature scalar

$$R = \psi^{-4} \bar{R} - 8\psi^{-5} \bar{D}^2 \psi. \quad (3.4)$$

Here $\bar{D}^2 = \bar{\gamma}^{ij} \bar{D}_i \bar{D}_j$, \bar{R}_{ij} and \bar{R} are the covariant Laplace operator, Ricci tensor and scalar curvature associated with $\bar{\gamma}_{ij}$. \bar{R}_{ij} can be computed by inserting $\bar{\gamma}_{ij}$ into equation (2.43).

Example 3.1 *Returning to Example 2.1, we now see that the spatial part of the metric (2.60) is a conformal factor ψ^4 times the flat metric η_{ij} in spherical coordinates. Since any spherically symmetric metric can be brought into the form (2.60) without loss of generality, we have shown that any spherically symmetric metric is (spatially) conformally flat.*

Instead of computing curvature quantities from the spatial metric γ_{ij} , it is now much easier to employ the above formalism. The connection coefficients (2.61), for example, can be found by adding the connection coefficients $\bar{\Gamma}_{jk}^i$ of a flat metric in spherical coordinates to spatial derivatives of ψ according to (3.2). Since $\bar{\gamma}_{ij} = \eta_{ij}$ is flat, the conformally related Ricci tensor vanishes $\bar{R}_{ij} = 0$ and the physical Ricci tensor is given by the derivatives of ψ in (3.3) alone. The Ricci scalar, finally, reduces to

$$R = -8\psi^{-5} \bar{D}^2 \psi, \quad (3.5)$$

a remarkably simple expression.

It is also convenient to split the extrinsic curvature K_{ij} into its trace K and a traceless part A_{ij}

$$K_{ij} = A_{ij} + \frac{1}{3} \gamma_{ij} K. \quad (3.6)$$

Solving the initial value problem usually proceeds by further decomposing the traceless part A_{ij} , which is done slightly differently in different approaches.

In the following we will briefly discuss the transverse-traceless and the thin-sandwich decomposition.

3.2 The Conformal Transverse-Traceless Decomposition

In the conformal transverse-traceless decomposition, we first introduce the conformal traceless extrinsic curvature by defining

$$A^{ij} = \psi^{-10} \bar{A}^{ij} \quad (3.7)$$

and accordingly $A_{ij} = \psi^{-2} \bar{A}_{ij}$ (see, e.g., York (1979)). Other choices for the exponent of the conformal factor are possible as well – and in fact we will use a different scaling in Section 4.3 – but for our purposes here the exponent -10 is particularly convenient since any symmetric traceless tensor S^{ij} satisfies $D_j S^{ij} = \psi^{-10} \bar{D}_j (\psi^{10} S^{ij})$.

Any symmetric, traceless tensor can be split into a transverse-traceless tensor, which is divergenceless, and a longitudinal part, which can be written as a symmetric, traceless gradient of a vector (York, 1973). We can therefore further decompose \bar{A}^{ij} as

$$\bar{A}^{ij} = \bar{A}_{TT}^{ij} + \bar{A}_L^{ij}, \quad (3.8)$$

where the transverse part is divergenceless

$$\bar{D}_j \bar{A}_{TT}^{ij} = 0 \quad (3.9)$$

and where the longitudinal part satisfies

$$\bar{A}_L^{ij} = \bar{D}^i W^j + \bar{D}^j W^i - \frac{2}{3} \bar{\gamma}^{ij} \bar{D}_k W^k \equiv (\bar{L}W)^{ij}. \quad (3.10)$$

Here W^i is a vector potential, and it is easy to see that the *longitudinal operator* or *vector gradient* \bar{L} produces a symmetric, traceless tensor. The divergence of \bar{A}^{ij} can be written as

$$\begin{aligned} \bar{D}_j \bar{A}^{ij} &= \bar{D}_j \bar{A}_L^{ij} = \bar{D}_j (\bar{L}W)^{ij} = \bar{D}^2 W^i + \frac{1}{3} \bar{D}^i (\bar{D}_j W^j) + \bar{R}^i_j W^j \\ &\equiv (\bar{\Delta}_L W)^i, \end{aligned} \quad (3.11)$$

where $\bar{\Delta}_L$ is the vector Laplacian.

Inserting the conformally related quantities into (2.44) now yields the Hamiltonian constraint

$$8\bar{D}^2\psi - \psi\bar{R} - \frac{2}{3}\psi^5K^2 + \psi^{-7}\bar{A}_{ij}\bar{A}^{ij} = -16\pi\psi^5\rho, \quad (3.12)$$

while the momentum constraint (2.45) becomes

$$(\bar{\Delta}_L W)^i - \frac{2}{3}\psi^6\bar{\gamma}^{ij}\bar{D}_jK = 8\pi\psi^{10}j^i. \quad (3.13)$$

Example 3.2 *As a consequence of the Bianchi identities, not all of Einstein's equations are independent. This redundancy can be exploited in numerical evolution calculations, where some quantities can be solved for using either constraint or evolution equations. The conformal factor ψ , for example, satisfies an evolution equation (which in spherical symmetry can be found by solving equation (2.63) for $\dot{\psi}$) and the Hamiltonian constraint (3.12). In fact, the evolution equations can be completely eliminated in spherical symmetry, which reflects the fact that in spherical symmetry the gravitational fields do not carry any dynamical degrees of freedom. In constrained evolution codes some of the evolution equations are replaced by constraint equations, while in unconstrained evolution codes the gravitational fields are computed from the evolution equations alone, while the constraint equations are typically used to monitor the quality of the numerical solution. Constrained evolution has been very popular in spherical and axial symmetry. In full 3D, however, solving the elliptic constraint equation is very expensive computationally, so that most current codes in 3 + 1 use unconstrained evolution.*

Given a solution to the constraint equations, one can find the mass, linear and angular momenta from the asymptotic behavior of the solution. For asymptotically flat solutions, the total (ADM) energy is

$$M = -\frac{1}{2\pi} \oint_{\infty} \bar{D}^i\psi d^2S_i, \quad (3.14)$$

the linear momentum is

$$P^i = \frac{1}{8\pi} \oint_{\infty} \bar{K}^{ij} d^2S_j, \quad (3.15)$$

and, in Cartesian coordinates, the angular momentum is

$$J_i = \frac{\epsilon_{ijk}}{8\pi} \oint_{\infty} x^j K^{kl} d^2S_l \quad (3.16)$$

(see, e.g., Ó Murchadha and York (1974); Bowen and York (1980); York (1980)).

At this point it is instructive to count degrees of freedom. We started out with six independent variables in both the spatial metric γ_{ij} and the extrinsic curvature K_{ij} . Splitting off the conformal factor ψ left five degrees of freedom in the conformally related metric $\bar{\gamma}_{ij}$ (specifying $\bar{\gamma}$). Of the six independent variables in K^{ij} we moved one into its trace K , two into A_{TT}^{ij} (which is symmetric, traceless, and divergenceless), and three into A_L^{ij} (which is reflected in its representation by a vector). Of the twelve original degrees of freedom, the constraint equations determine only four, namely the conformal factor ψ (Hamiltonian constraint) and the longitudinal part of the traceless extrinsic curvature (momentum constraint). Four of the remaining degrees of freedom are associated with the coordinate freedom – three spatial coordinates hidden in the spatial metric and one that determines the evolution in time that is often identified with K . This leaves four physical degrees of freedom undetermined – two in the conformally related metric $\bar{\gamma}_{ij}$, and two in the transverse part of traceless extrinsic curvature A_{TT}^{ij} . These two freely specifiable degrees of freedom carry the dynamical degrees of freedom of the gravitational fields. All others are either fixed by the constraint equations or represent coordinate freedom.

It is obvious that the background data $\bar{\gamma}_{ij}$, \bar{A}_{TT}^{ij} and K have to be chosen before the constraints can be solved for ψ and \bar{A}_L^{ij} . The choice of background data has to be made in accordance with the physical or astrophysical situation that one wants to represent. Physically, the choice reflects the amount of gravitational wave content in the background. In many situations, as for example for close compact binaries, it is not a priori clear what choices correspond to the desired astrophysical scenario and reflect the past inspiral history. Arguments have then be made that the background data can be approximated reasonably well by conformal flatness $\bar{\gamma}_{ij} = \eta_{ij}$, maximal slicing $K = 0$ (see Section 5.2) and $\bar{A}_{TT}^{ij} = 0$. While this choice is somewhat controversial (see the discussion in Appendix C), it has the great benefit of dramatically simplifying the constraint equations (3.12) and (3.13).

It is quite remarkable that the momentum constraint (3.13) is a linear equation for the vector potential W^i . For maximal slicing $K = 0$ and in vacuum $j = 0$ it also decouples from the Hamiltonian constraint, and can be solved independently of a solution for ψ . For conformal flatness, the operator $\bar{\Delta}_L$ simplifies significantly (see also Appendix B), and in fact we will discuss analytic solutions in Section 7.1.

Assuming conformal flatness, the Hamiltonian constraint (3.12) also simplifies significantly, since \bar{D}^2 reduces to the flat Laplace operator and $\bar{R} = 0$. Maximal slicing further simplifies the equation.

Example 3.3 *As we have seen in Example 3.1, the metric (2.60) is conformally flat. If we are further interested in time-symmetric vacuum solutions (whereby $K_{ij} = -K_{ij} = 0$ and $\rho = 0$), the Hamiltonian constraint (3.12) reduces to the simple Laplace equation*

$$\Delta^{\text{flat}}\psi = 0 \tag{3.17}$$

in spherical symmetry (where Δ^{flat} is the flat Laplace operator). Assuming asymptotic flatness, so that $\psi \rightarrow 1$ as $r \rightarrow \infty$, we can write the solution as

$$\psi = 1 + \frac{m}{2r} \tag{3.18}$$

where m is a constant. Evaluating the ADM mass (3.14) of this solution shows that $M = m$. We have therefore rediscovered the spatial part of the Schwarzschild solution in isotropic coordinates. We will see in Example 6.1 that the surface $r = m/2$ is the event (and apparent) horizon of a black hole.

It can be shown that the coordinate transformation $x^i \rightarrow (m/2)^2 x^i / r^2$ maps every point inside $r = m/2$ into a point outside $r = m/2$. Moreover, the transformation maps the metric into itself, making it an isometry. Applying the coordinate transformation twice yields the identity transformation, and points on the horizon $r = m/2$ are mapped into themselves. We can therefore think of the transformation as a reflection across $r = m/2$. The geometry close to the origin is therefore identical to the geometry near infinity, which suggests that we can think of the geometry as two asymptotically flat sheets, or else as two separate but identical universes, which are connected by a throat or Einstein-Rosen bridge (Einstein and Rosen, 1935). See Figure 31.5 in Misner, Thorne and Wheeler (1973) for an embedding diagram.

It is remarkable that equation (3.17) is linear. As an immediate consequence, time-symmetric initial data containing multiple black holes can be constructed by simply adding several terms of the form (3.18). We will return to the construction of binary black hole initial data in Section 7.

3.3 The Thin-Sandwich Decomposition

Solving the conformal transverse-traceless decomposition yields data γ_{ij} and K_{ij} intrinsic to one spatial slice Σ , but this solution does not tell us anything about how it will evolve in time away from Σ , nor does the formalism allow us to determine any such time-evolution. In some circumstances, for example when we are interested in constructing equilibrium or quasi-equilibrium solutions, we would like to construct data such that they do have a certain

time-evolution. The *thin-sandwich* approach offers an alternative that does allow us to determine the evolution of the spatial metric. Instead of providing data for γ_{ij} and K_{ij} on one timeslice, it provides data for γ_{ij} on two timeslices, or, in the limit of infinitesimal separation of the two slices, data for γ_{ij} and its time derivative. The original thin-sandwich conjecture goes back to Baierlein, Sharp and Wheeler (1962) (see also the discussion in Misner, Thorne and Wheeler (1973)), but here we will focus on a more recent, conformal formulation (York, 1999; Cook, 2000). A similar formulation has been developed independently (and earlier) by Wilson and Mathews (1989, 1995) (see Section 10.2).

Following Cook (2000), to whom the reader is referred for a more detailed treatment, we start by defining u_{ij} as the traceless part of the time derivative of the spatial metric,

$$u_{ij} \equiv \gamma^{1/3} \partial_t (\gamma^{-1/3} \gamma_{ij}), \quad (3.19)$$

in terms of which the evolution equation (2.46) becomes

$$u^{ij} = -2\alpha A^{ij} + (L\beta)^{ij}. \quad (3.20)$$

Here L is the vector gradient defined in (3.10), except in terms of the physical metric γ_{ij} . Using⁴

$$u_{ij} = \psi^4 \bar{u}_{ij} \quad (3.21)$$

together with the conformal scaling (3.7) and the identity $(L\beta)^{ij} = \psi^{-4}(\bar{L}\beta)^{ij}$, we can rewrite equation (3.20) as

$$\bar{A}^{ij} = \frac{\psi^6}{2\alpha} \left((\bar{L}\beta)^{ij} - \bar{u}^{ij} \right). \quad (3.22)$$

This equation relates \bar{A}^{ij} to the shift vector β^i . Inserting this equation into the momentum constraint (2.45), we can therefore derive an equation for the shift

$$\begin{aligned} (\bar{\Delta}_L \beta)^i - (\bar{L}\beta)^{ij} \bar{D}_j \ln(\alpha \psi^{-6}) = \\ \alpha \psi^{-6} \bar{D}_j (\alpha^{-1} \psi^6 \bar{u}^{ij}) + \frac{4}{3} \alpha \bar{D}^i K + 16\pi \alpha \psi^4 j^i. \end{aligned} \quad (3.23)$$

A solution of the thin-sandwich formulation can now be constructed as follows. We choose the background metric $\bar{\gamma}_{ij}$ as well as its time derivative \bar{u}_{ij} . Given

⁴ This follows from the identifications $\bar{u}_{ij} = \partial_t \bar{\gamma}_{ij}$ and $\bar{\gamma}^{ij} \bar{u}_{ij} = 0$.

choices for the lapse α and the trace of the extrinsic curvature K , we can then solve the Hamiltonian constraint (3.12) and the momentum constraint (3.23) for the conformal factor ψ and the shift β^i ⁵. With these solutions, we can then construct \bar{A}^{ij} from (3.22) and finally the physical quantities γ_{ij} and K_{ij} .

It is again instructive to count the degrees of freedom, and to compare with the transverse-traceless decomposition of Section 3.2. There, we found that of the twelve independent variables in γ_{ij} and K_{ij} , four were determined by the constraint equations, four were related to the coordinate freedom, and four represented the dynamical degrees of freedom of general relativity. The latter eight can be chosen freely. In the thin-sandwich formalism, we count a total of sixteen independent variables, of which we can freely choose twelve: five each in $\bar{\gamma}_{ij}$ and \bar{u}_{ij} , and one each for α and K . The four remaining variables, ψ and β^i , are then determined by the constraint equations. The four new independent variables are accounted for by the lapse α and the shift β^i , which are absent from the transverse-traceless decomposition. That approach only deals with quantities intrinsic to one spatial slice Σ , and hence only requires coordinates on Σ . The thin-sandwich approach, on the other hand, also takes into account the evolution of the metric away from that slice, and therefore requires coordinates in a neighborhood of Σ . As a consequence, the lapse α and the shift β^i , which describe the evolution of the coordinates away from Σ , appear in the thin-sandwich approach, but not in the transverse-traceless decomposition. The four new free degrees of freedom hence reflect the time derivatives of the coordinates.

The thin-sandwich approach is particularly useful for the construction of equilibrium or quasi-equilibrium data, for which it is natural to choose

$$\bar{u}_{ij} = 0. \quad (3.24)$$

For equilibrium data it is also natural to choose $K = 0$ and $\partial_t K = 0$, which from equation (2.49) yields the maximal slicing condition

$$D^2\alpha = \alpha \left(A_{ij}A^{ij} + 4\pi(\rho + S) \right). \quad (3.25)$$

We will discuss maximal slicing in more detail in Section 5.2. Expressing D^2 in terms of \bar{D}^2 and using the conformal transformations of Section 3.1, we find that this equation can be combined with the Hamiltonian constraint to yield

$$\bar{D}^2(\alpha\psi) = \alpha\psi \left(\frac{7}{8}\psi^{-8}\bar{A}_{ij}\bar{A}^{ij} + \frac{1}{8}\bar{R} + 2\pi\psi^4(\rho + 2S) \right). \quad (3.26)$$

⁵ Strictly speaking, the “densitized” lapse $\hat{\alpha} = \gamma^{-1/2}\alpha$ (see also equation (4.16) below) should be fixed instead of the lapse α (York, 1999). This distinction is unnecessary if the lapse is determined through maximal slicing.

Equations (3.12), (3.23) and (3.26) now determine the solutions for ψ , β^i and α . The equations further simplify if we assume conformal flatness, in which case they reduce to

$$\Delta^{\text{flat}}\psi = -\frac{1}{8}\psi^{-7}\bar{A}_{ij}\bar{A}^{ij} - 2\pi\psi^5\rho \quad (3.27)$$

$$(\Delta_L^{\text{flat}}\beta)^i = 2\bar{A}^{ij}\bar{D}_j(\alpha\psi^{-6}) + 16\pi\alpha\psi^4j^i \quad (3.28)$$

$$\Delta^{\text{flat}}(\alpha\psi) = \alpha\psi\left(\frac{7}{8}\psi^{-8}\bar{A}_{ij}\bar{A}^{ij} + 2\pi\psi^4(\rho + 2S)\right). \quad (3.29)$$

Here Δ^{flat} and Δ_L^{flat} are the flat Laplacian and vector Laplacian. Strategies for solving the flat vector Laplacian will be discussed in Appendix B. Interestingly, we will re-discover the shift condition (3.28) in Section 5.4 and will find that it is identical to minimal distortion. The thin-sandwich formalism therefore reduces to the Hamiltonian constraint for the conformal factor, the minimal distortion condition for the shift, and the maximal slicing condition for the lapse.

If initial data for a time evolution calculation are constructed from the transverse-traceless decomposition, then the lapse and shift have to be chosen independently of the construction of initial data. The thin-sandwich formalism, on the other hand, provides a lapse and a shift together with the initial data γ_{ij} and K_{ij} . Obviously, once the initial data are determined, the lapse and shift can always be chosen freely in performing subsequent evolution calculations. However, the original relation between the time derivative of γ_{ij} and \bar{u}_{ij} only applies when the lapse and shift of the thin-sandwich solution are employed.

4 Rewriting the ADM evolution equations

The ADM equations as presented in Section 2.2 form the basis for most 3+1 decompositions of the Einstein equations and their numerical implementations. As it turns out, the evolution equations are not yet in their most desirable form, and straight-forward implementations in three spatial dimensions typically develop instabilities very quickly.

In this Section we will discuss the draw-backs of the ADM equations and will present possible alternatives. We will first illustrate some of the relevant issues with an electrodynamics analogy, and will then present two different re-formulations of the ADM equations.

4.1 Rewriting Maxwell's equations

In Section 2.3 we showed that Maxwell's equations, when written as the two evolution equations (2.55) and (2.56)

$$\partial_t A_i = -E_i - D_i \Phi \quad (4.1)$$

$$\partial_t E_i = -D^j D_j A_i + D_i D^j A_j - 4\pi J_i \quad (4.2)$$

and the constraint equation (2.50)

$$D^i E_i = 4\pi \rho_e, \quad (4.3)$$

share some of the structure of the ADM equations. In fact they also share some of their draw-backs. To illustrate these, take a time derivative of (4.1) and insert (4.2) to form a single equation for the vector potential A_i

$$-\partial_t^2 A_i + D^j D_j A_i - D_i D^j A_j = D_i \partial_t \Phi - 4\pi J_i. \quad (4.4)$$

It is obvious that this equation would be a simple wave equation for the components A_i if it weren't for the mixed derivative term $D_i D^j A_j$. In general relativity the situation is very similar, since the Ricci tensor R_{ij} (2.43) on the right hand side of equation (2.47) also contains mixed derivative terms in addition to a Laplace operator acting on γ_{ij} . Without these mixed derivatives, the ADM equations could be written as wave equations for the components of the spatial metric and would be manifestly hyperbolic (see, e.g., Friedrich (1996) for a discussion). This is unfortunate, since it would be desirable in many ways to deal with a hyperbolic system of equations. Mathematical theorems would guarantee the existence and uniqueness of solutions, and for numerical purposes one could bring the equations into a form that allows for the application of flux-conservative schemes that have been developed and tested in other fields of computational physics, and quite in general one might feel more comfortable that numerical implementations will produce stable evolutions.

These considerations suggest that it might be desirable to eliminate the mixed derivative terms. In electrodynamics, three different approaches can be taken to eliminate the $D_i D^j A_j$ term: one can make a special *gauge choice*, one can bring Maxwell's equations into an *explicitly hyperbolic* form, or one can introduce an *auxiliary variable*. For the remainder of this section, we will briefly discuss each one of these three strategies.

The most straightforward approach is to choose a *gauge* such that the term $D_i D^j A_j$ disappears. This can be achieved, for example, in the Lorentz gauge

$$\partial_t \Phi = -D^i A_i \quad (4.5)$$

for which these two terms cancel in equation (4.4), reducing it to a wave equation for the vector potential A_i (see Jackson (1975)). Another possibility is the Coulomb gauge $D^i A_i = 0$, which results in an elliptic equation for Φ .

In general relativity, an analogous approach can be taken by choosing harmonic coordinates (see Section 5.3), which bring the equations into a manifestly hyperbolic form. This was first realized by De Donder (1921) and Lanczos (1922), and many recent hyperbolic formulations of Einstein's equations are based on this gauge choice (e.g. Choquet-Bruhat (1952, 1962); Fischer and Marsden (1972)). For the purpose of numerical simulations this strategy does not seem very promising, since harmonic coordinates may not be the optimal coordinate choice for the astrophysical situation at hand (but see Landry and Teukolsky (1999), where the traditional ADM approach together with harmonic coordinates and finely tuned finite differencing has been used to simulate the merger of binary neutron stars; see also Garfinkle (2002)). Moreover, harmonic coordinates may develop pathologies which could prematurely end a numerical simulation (Alcubierre, 1997; Alcubierre and Massó, 1998). It is therefore more desirable to preserve the coordinate freedom, and to adopt a different approach to re-writing the equations.

An alternative, gauge-covariant approach to bringing Maxwell's equations into an *explicitly hyperbolic* form is to take a time derivative of (4.2) instead of (4.1), which yields (Abrahams and York, 1997)

$$\partial_t^2 E_i = D_i D^j (-E_j - D_j \Phi) - D_j D^j (-E_i - D_i \Phi) - \partial_t J_i. \quad (4.6)$$

Using the constraint (4.3) we can eliminate the first term and find a wave equation for E_i

$$-\partial_t^2 E_i + D_j D^j E_i = \partial_t J_i + 4\pi D_i \rho_e. \quad (4.7)$$

Interestingly, the gauge dependent quantities A_i and Φ have disappeared from this equation, and, quoting Abrahams and York (1997), “the dynamics of electromagnetism have been cleanly separated from the gauge-dependent evolution of the vector and scalar potentials.” We will discuss similar approaches in general relativity in Section 4.2.

While equation (4.7) is aesthetically very appealing, it also reveals some potential disadvantages for simulations that involve matter. In evolution calcu-

lations of neutron stars, for example, the non-smoothness of the matter and fields on the stellar surface or across shocks always pose numerical difficulties. It is to be expected that these would only get worse if further derivatives of the matter variables have to be taken, as in equation (4.7).

This suggests a third approach to re-writing Maxwell's equations, namely by introducing an *auxiliary variable*

$$\Gamma = D^i A_i. \quad (4.8)$$

Inserting this into (4.2) yields

$$\partial_t E_i = -D_j D^j A_i + D_i \Gamma - 4\pi J_i. \quad (4.9)$$

We now elevate Γ 's status to that of a new independent variable, and derive its evolution equation from (4.1)

$$\begin{aligned} \partial_t \Gamma &= \partial_t D^i A_i = D^i \partial_t A_i = -D^i E_i - D_i D^i \Phi \\ &= -D_i D^i \Phi - 4\pi \rho_e. \end{aligned} \quad (4.10)$$

Note that we have used the constraint equation (4.3) in the last equality, similar to how we used the same constraint to arrive at the wave equation (4.7). We will see in equation (4.31) below that this step is crucial for stabilizing the system.

Equations (4.1), (4.9) and (4.10) are now the evolution equations in this new formulation, and equations (4.3) and (4.8) are the constraint equations. In this formulation the mixed derivative term $D_i D^j A_j$ has been eliminated without using up the gauge freedom, and without introducing derivatives of the matter terms. In Section 4.3 we will introduce an analogous re-formulation of the ADM equations.

4.2 Hyperbolic formulations

In light of the disadvantages of the ADM system, a large number of $3+1$ hyperbolic formulations of general relativity have been developed recently (see the recent review article by Reula (1998) for an extensive survey and a more complete list of references). The first formulations that departed from the assumption of harmonic coordinates (Choquet-Bruhat, 1952, 1962; Fischer and Marsden, 1972) were based on a spin-frame formalism (Friedrich, 1981a,b, 1985, 1986a,b). Other formulations introduced partial derivatives of the metric and other quantities as new independent variables (e.g. Bona and Massó

(1992); Frittelli and Reula (1994, 1996); Bona, Massó, Seidel and Stela (1995, 1997)). In analogy to the electromagnetic example in Section 4.1, Choquet-Bruhat and Ruggeri (1983) and Abrahams *et.al.* (1995) took a time derivative of equation (2.47) to derive a hyperbolic system that is sometimes referred to as the “Einstein-Ricci” system (see also Abrahams and York (1997)). Alternatively, Friedrich (1996) and Anderson, Choquet-Bruhat and York (1997) used the Bianchi identities to derive another hyperbolic system for general relativity, sometimes called the “Einstein-Bianchi” system. Anderson and York (1999) developed the “Einstein-Christoffel” system by introducing additional “connection” variables. Other recent hyperbolic formulations are based on frame or tetrad formalisms (van Putten and Eardley, 1996; Estabrook, Robinson and Wahlquist, 1997), the Ashtekar formulation (Yoneda and Shinkai, 1999, 2000, 2001a; Shinkai and Yoneda, 2000), a conformal decomposition (Alcubierre *et.al.*, 1999), and a so-called λ -system that embeds Einstein’s equations in a larger symmetric hyperbolic system with the constraint surface of Einstein’s equations as an attractor of the evolution (Brodbeck *et.al.*, 1999).

It is clearly beyond the scope of this article to review all of these formulations. Some of these systems have features that are not very desirable numerically, in that they restrict the gauge freedom, introduce extra derivatives of the matter variables, or introduce a large number of auxiliary variables. Only few of these formulations have been implemented numerically, and most of these implementations assumed certain simplifying symmetry conditions (e.g. spherical symmetry). Some of these implementations showed advantages over the ADM formalism (e.g. Bona and Massó (1992)), but others also revealed additional problems. Scheel *et.al.* (1997, 1998), for example, found that a particular equation in the “Einstein-Ricci” system produced an instability, which could be removed in spherical symmetry, but not in more general 3D simulations. Very few hyperbolic systems have been implemented in 3D, including that of Bona and Massó (Bona and Massó, 1992; Bona, Massó, Seidel and Stela, 1995, 1997), and generalized versions of the “Einstein-Christoffel” system (Anderson and York, 1999). The latter have been implemented numerically by Kidder, Scheel and Teukolsky (2001, see also Kidder *et.al.* (2000)) using spectral methods. Since this formulation is particularly elegant and currently seems like the most promising hyperbolic formulation, we provide a brief summary. Some properties of this formulation have been analyzed by Calabrese, Lehner and Tiglio (2002); Calabrese *et.al.* (2002) and Lindblom and Scheel (2002).

Starting with the ADM formalism as presented in Section 2, and adopting the notation of Kidder *et.al.* (2000), we define the new variables

$$f_{kij} = \Gamma_{(ij)k} + \gamma_{ki}\gamma^{lm}\Gamma_{[lj]m} + \gamma_{kj}\gamma^{lm}\Gamma_{[li]m}. \quad (4.11)$$

These functions are now promoted to independent functions. It can then be

shown that the evolution equations (2.46) and (2.47) can be rewritten as

$$\begin{aligned}
d_t \gamma_{ij} &= -2\alpha K_{ij} \\
d_t K_{ij} + \alpha \gamma^{kl} \partial_l f_{kij} &= \alpha M_{ij} \\
d_t f_{kij} + \alpha \partial_k K_{ij} &= \alpha N_{kij}.
\end{aligned} \tag{4.12}$$

Here we have used the abbreviation

$$d_t \equiv \partial_t - \mathcal{L}_\beta \tag{4.13}$$

and the source terms M_{ij} and N_{ijk} are given by

$$\begin{aligned}
M_{ij} = & \gamma^{kl} (K_{kl} K_{ij} - 2K_{ki} K_{lj}) + \gamma^{kl} \gamma^{mn} (4f_{kmi} f_{[ln]j} \\
& + 4f_{km[n} f_{l]ij} - f_{ikm} f_{jln} + 8f_{(ij)k} f_{[ln]m} + 4f_{km(i} f_{j)ln} \\
& - 8f_{kli} f_{mnj} + 20f_{kl(i} f_{j)mn} - 13f_{ikl} f_{jmn}) \\
& - \partial_i \partial_j \ln \hat{\alpha} - (\partial_i \ln \hat{\alpha})(\partial_j \ln \hat{\alpha}) + 2\gamma_{ij} \gamma^{kl} \gamma^{mn} (f_{kmn} \partial_l \ln \hat{\alpha} \\
& - f_{kml} \partial_n \ln \hat{\alpha}) + \gamma^{kl} \left((2f_{(ij)k} - f_{kij}) \partial_l \ln \hat{\alpha} \right. \\
& + 4f_{kl(i} \partial_{j)} \ln \hat{\alpha} - 3(f_{ikl} \partial_j \ln \hat{\alpha} + f_{jkl} \partial_i \ln \hat{\alpha}) \Big) \\
& \left. - 8\pi S_{ij} + 4\pi \gamma_{ij} T \right)
\end{aligned} \tag{4.14}$$

and

$$\begin{aligned}
N_{kij} = & \gamma^{mn} \left(4K_{k(i} f_{j)mn} - 4f_{mn(i} K_{j)k} + K_{ij} (2f_{mnk} - 3f_{kmn}) \right) \\
& + 2\gamma^{mn} \gamma^{pq} \left(K_{mp} (\gamma_{k(i} f_{j)qn} - 2f_{qn(i} \gamma_{j)k}) \right. \\
& + \gamma_{k(i} K_{j)m} (8f_{npq} - 6f_{pqn}) + K_{mn} (4f_{pq(i} \gamma_{j)k} - 5\gamma_{k(i} f_{j)pq}) \Big) \\
& - K_{ij} \partial_k \ln \hat{\alpha} + 2\gamma^{mn} (K_{m(i} \gamma_{j)k} \partial_n \ln \hat{\alpha} - K_{mn} \gamma_{k(i} \partial_{j)} \ln \hat{\alpha}) \\
& \left. + 16\pi \gamma_{k(i} j_{j)}. \right)
\end{aligned} \tag{4.15}$$

We have also used the “densitized” lapse function

$$\hat{\alpha} = \gamma^{-1/2} \alpha \tag{4.16}$$

and, in addition to the matter terms defined in Section 2, the four-dimensional trace of the stress energy tensor

$$T = g^{ab} T_{ab}. \tag{4.17}$$

The above equations form the “Einstein-Christoffel” system of Anderson and York (1999). Evolutions of a single black hole using a spectral implementation of this system are still unstable (compare Section 8.1), but Kidder, Scheel and Teukolsky (2001) were able to show that the lifetime of these simulation can be extended to late times by a certain generalization of the equations. This generalization involves the redefinition of variables and an addition of constraints, and embeds the above equations into a 12-parameter family of hyperbolic formulations. The stability properties of the system depend strongly on the choice of the free parameters, which can be understood analytically in terms of energy norm arguments (Lindblom and Scheel, 2002).

The first order symmetric hyperbolic system (4.12) is equivalent to the original set of evolution equations (2.46) and (2.47). Since the f_{kij} are evolved as independent functions, their original definition (4.11) can be considered as a new constraint equation in addition to (2.44) and (2.45). This system is particularly elegant because the source terms M_{ij} and N_{ijk} on the right hand sides do not contain any derivatives of the fundamental variables (other than the arbitrary lapse function α). Equations (4.12) can be combined to yield a wave equation for the components of the spatial metric γ_{ij} in which the right hand sides appear as sources.

Hyperbolic systems have the great advantage that their characteristic structure can be analyzed. In the system (4.12), all characteristic fields propagate either along the light cone or normal to the spatial foliation. This knowledge can be used for the construction of boundary conditions, both at the outer boundaries and on inner boundaries if the interior of black holes is excised (see, e.g., Kidder *et.al.* (2000) and Section 8.1).

4.3 The BSSN formulation

Following the electrodynamic example of Section 4.1 we can also eliminate the mixed second derivatives in the Ricci tensor with the help of auxiliary variables (Nakamura, Oohara and Kojima, 1987). In addition, the conformal factor and the trace of the extrinsic curvature are evolved separately, which follows the philosophy of separating transverse from longitudinal, or radiative from non-radiative degrees of freedom (see Section 3).

We follow here the formulation of Baumgarte and Shapiro (1999), which is based on that of Shibata and Nakamura (1995). We start by writing the conformal factor as $\psi = e^\phi$ so that

$$\bar{\gamma}_{ij} = e^{-4\phi} \gamma_{ij}, \tag{4.18}$$

and by choosing it such that the determinant of the conformally related metric $\bar{\gamma}_{ij}$ is unity, $\phi = (\ln \gamma)/12$. As in equation (3.6) we split the trace from the extrinsic curvature and conformally rescale the traceless part A_{ij} . Following Shibata and Nakamura (1995) and Baumgarte and Shapiro (1999) again, we choose a conformal rescaling that is different from (3.7) and instead rescale A_{ij} like the metric itself

$$\tilde{A}_{ij} = e^{-4\phi} A_{ij}. \quad (4.19)$$

We will use tildes as opposed to the bars used in Section 3 as a reminder of this different rescaling. Indices of \tilde{A}_{ij} will be raised and lowered with the conformal metric $\bar{\gamma}_{ij}$, so that $\tilde{A}^{ij} = e^{4\phi} A^{ij}$

Evolution equations for ϕ and K can now be found from equation (2.48), yielding

$$\partial_t \phi = -\frac{1}{6} \alpha K + \beta^i \partial_i \phi + \frac{1}{6} \partial_i \beta^i \quad (4.20)$$

and (2.49)

$$\partial_t K = -\gamma^{ij} D_j D_i \alpha + \alpha (\tilde{A}_{ij} \tilde{A}^{ij} + \frac{1}{3} K^2) + 4\pi \alpha (\rho + S) + \beta^i \partial_i K. \quad (4.21)$$

Subtracting these from the evolution equations (2.46) and (2.47) yields the traceless evolution equations for $\bar{\gamma}_{ij}$

$$\partial_t \bar{\gamma}_{ij} = -2\alpha \tilde{A}_{ij} + \beta^k \partial_k \bar{\gamma}_{ij} + \bar{\gamma}_{ik} \partial_j \beta^k + \bar{\gamma}_{kj} \partial_i \beta^k - \frac{2}{3} \bar{\gamma}_{ij} \partial_k \beta^k. \quad (4.22)$$

and \tilde{A}_{ij}

$$\begin{aligned} \partial_t \tilde{A}_{ij} = & e^{-4\phi} \left(-(D_i D_j \alpha)^{TF} + \alpha (R_{ij}^{TF} - 8\pi S_{ij}^{TF}) \right) \\ & + \alpha (K \tilde{A}_{ij} - 2 \tilde{A}_{il} \tilde{A}^l_j) \\ & + \beta^k \partial_k \tilde{A}_{ij} + \tilde{A}_{ik} \partial_j \beta^k + \tilde{A}_{kj} \partial_i \beta^k - \frac{2}{3} \tilde{A}_{ij} \partial_k \beta^k. \end{aligned} \quad (4.23)$$

In the last equation, the superscript TF denotes the trace-free part of a tensor, e.g. $R_{ij}^{TF} = R_{ij} - \gamma_{ij} R/3$. Note also that in equations (4.20) through (4.23) the shift terms arise from Lie derivatives of the respective variable. The divergence of the shift, $\partial_i \beta^i$, appears in the Lie derivative because the choice $\bar{\gamma} = 1$ makes ϕ a tensor density of weight $1/6$, and $\bar{\gamma}_{ij}$ and \tilde{A}_{ij} tensor densities of weight $-2/3$.

According to (3.3) we can split the Ricci tensor into two terms

$$R_{ij} = \bar{R}_{ij} + R_{ij}^\phi, \quad (4.24)$$

where R_{ij}^ϕ can be found by inserting $\phi = \ln \psi$ into (3.3). The conformally related Ricci tensor \bar{R}_{ij} could be computed by inserting $\bar{\gamma}_{ij}$ into (2.43), which would introduce the mixed second derivatives similar to those in the electrodynamics illustration of Section 4.1. In analogy to the new variable Γ that we used to eliminate those mixed derivatives there, we can now define the “conformal connection functions”

$$\bar{\Gamma}^i \equiv \bar{\gamma}^{jk} \bar{\Gamma}_{jk}^i = -\bar{\gamma}^{ij}{}_{,j}, \quad (4.25)$$

where the $\bar{\Gamma}_{jk}^i$ are the connection coefficients associated with $\bar{\gamma}_{ij}$, and where the last equality holds because $\bar{\gamma} = 1$ (see Problem 7.7f in Lightman *et.al.* (1975)). In terms of these, the Ricci tensor can be written

$$\begin{aligned} \bar{R}_{ij} = & -\frac{1}{2} \bar{\gamma}^{lm} \bar{\gamma}_{ij,lm} + \bar{\gamma}_{k(i} \partial_{j)} \bar{\Gamma}^k + \bar{\Gamma}^k \bar{\Gamma}_{(ij)k} + \\ & \bar{\gamma}^{lm} \left(2 \bar{\Gamma}_{l(i}^k \bar{\Gamma}_{j)km} + \bar{\Gamma}_{im}^k \bar{\Gamma}_{klj} \right). \end{aligned} \quad (4.26)$$

The only second derivatives of $\bar{\gamma}_{ij}$ left over in this operator is the Laplace operator $\bar{\gamma}^{lm} \bar{\gamma}_{ij,lm}$ – all others have been absorbed in first derivatives of $\bar{\Gamma}^i$. This property of the contraction of the Christoffel symbols has been known for a long time (De Donder, 1921; Lanczos, 1922), and has been used widely to write Einstein’s equations in a hyperbolic form (e.g. Choquet-Bruhat (1952); Fischer and Marsden (1972)).

We now promote the $\bar{\Gamma}^i$ to independent functions, and hence need to derive their evolution equation. This can be done in complete analogy to (4.10) by permuting a time and space derivative in the definition (4.25)

$$\partial_t \bar{\Gamma}^i = -\partial_j \left(2\alpha \tilde{A}^{ij} - 2\bar{\gamma}^{m(j} \beta^{i)}{}_{,m} + \frac{2}{3} \bar{\gamma}^{ij} \beta^l{}_{,l} + \beta^l \bar{\gamma}^{ij}{}_{,l} \right). \quad (4.27)$$

The divergence of the extrinsic curvature can now be eliminated with the help of the momentum constraint (2.45), which yields the evolution equation⁶

$$\begin{aligned} \partial_t \bar{\Gamma}^i = & -2\tilde{A}^{ij} \partial_j \alpha + 2\alpha \left(\bar{\Gamma}_{jk}^i \tilde{A}^{kj} - \frac{2}{3} \bar{\gamma}^{ij} \partial_j K - 8\pi \bar{\gamma}^{ij} S_j + 6\tilde{A}^{ij} \partial_j \phi \right) \\ & + \beta^j \partial_j \bar{\Gamma}^i - \bar{\Gamma}^j \partial_j \beta^i + \frac{2}{3} \bar{\Gamma}^i \partial_j \beta^j + \frac{1}{3} \bar{\gamma}^{li} \beta^j{}_{,jl} + \bar{\gamma}^{lj} \beta^i{}_{,lj}. \end{aligned} \quad (4.28)$$

⁶ Note that the shift terms enter with the wrong sign in equation (24) of Baumgarte and Shapiro (1999).

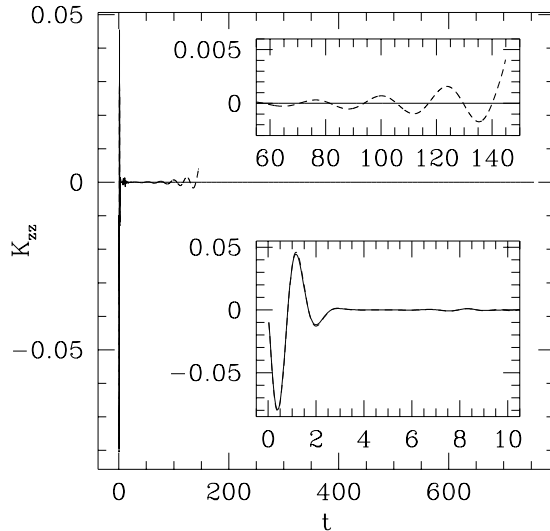


Fig. 4.1. Comparison of the evolution of a small amplitude gravitational wave using the ADM equations (dashed line) and the BSSN equations (solid line). The bottom panel shows the evolution of the K_{zz} component as a function of time for early times, for which both systems agree very well, while the top panel shows the evolution at a later time, just before the ADM system crashes. See text for more details. (Figure from Baumgarte and Shapiro (1999).)

Equations (4.20) through (4.23) together with (4.28) form a new system of evolution equations that is equivalent to (2.46) and (2.47). Since the $\bar{\Gamma}^i$ are evolved as independent functions, their original definition (4.25) serves as a new constraint equation, in addition to (2.44) and (2.45).

While the different formulations are equivalent analytically, the difference in performance of numerical implementations is striking. In Figure 4.1 we show a particular example from Baumgarte and Shapiro (1999). In this example, a small amplitude wave (Teukolsky, 1982) is evolved with harmonic slicing (see Section 5.3), zero shift, and a very simple outgoing wave boundary condition (see also Shibata and Nakamura (1995)). Both systems give very similar results early on, but the ADM system crashes very soon, while the BSSN system remains stable. Similar improvements have been found for many other applications, including strong field gravitational waves as well as black hole and neutron star spacetimes (Baumgarte, Hughes and Shapiro, 1999; Alcubierre *et.al.*, 2000b,d; Lehner, Huq and Garrison, 2000; Alcubierre and Brügmann, 2001). It is generally found that the ADM system is more accurate initially (which is to be expected given that it uses fewer equations), but that the BSSN system is much more stable in long term evolution calculations. Given this success, the BSSN system, either in the form of Shibata and Nakamura (1995) or Baumgarte and Shapiro (1999), is currently used very commonly in numerical relativity and has been adopted for many recent applications (an incomplete list includes Shibata (1999a,b); Shibata and Uryū (2000a); Shibata,

Baumgarte and Shapiro (2000a,b); Alcubierre *et.al.* (2000a, 2001a,b); Duez, Baumgarte and Shapiro (2001); Font *et.al.* (2001)).

Significant effort has also gone into understanding why implementations of the BSSN system are more stable than those of the ADM system (Frittelli and Reula, 1999; Alcubierre *et.al.*, 2000b; Miller, 2000; Yoneda and Shinkai, 2002; Sarbach *et.al.*, 2002, see also Frittelli and Gomez (2000)). While we are still lacking a complete understanding, several arguments point to the propagation of the constraints (compare Frittelli (1997)). Alcubierre *et.al.* (2000b) linearized the ADM and BSSN equations on a flat Minkowski background and showed that modes that violate the momentum constraint propagate with speed zero in the ADM equations. They also demonstrate in a model problem that such zero speed modes lead to instabilities when nonlinear source terms are included. Furthermore, they show that by adding the momentum constraint in the derivation of the $\bar{\Gamma}^i$ evolution equation (4.28) of the BSSN system, the momentum constraint violating modes now propagate with non-zero speed. Instead of building up locally, as in the ADM system, constraint violations can now propagate off the numerical grid⁷, presumably stabilizing the simulation⁸.

This effect can be illustrated very easily with the electrodynamic example of Section 4.1 (see Knapp, Walker and Baumgarte (2002)). In the Maxwell system, the time derivative of a constraint violation

$$\mathcal{C} \equiv D^i E_i - 4\pi\rho_e \quad (4.29)$$

vanishes identically

$$\begin{aligned} \partial_t \mathcal{C} &= \partial_t (D^i E_i - 4\pi\rho_e) = D^i \partial_t E_i - 4\pi \partial_t \rho_e \\ &= -D^i D^j D_j A_i + D^i D_i D^j A_j - 4\pi (D^i J_i + \partial_t \rho_e) = 0, \end{aligned} \quad (4.30)$$

where we have used the continuity equation $D_i J^i + \partial_t \rho_e = 0$. Using the modified system (4.1), (4.9) and (4.10), on the other hand, it can be shown that \mathcal{C} now satisfies a wave equation

$$\begin{aligned} \partial_t^2 \mathcal{C} &= \partial_t D^i \partial_t E_i - 4\pi \partial_t^2 \rho_e = \partial_t D^i (-D_j D^j A_i + D_i \Gamma - 4\pi J_i) - 4\pi \partial_t^2 \rho_e \\ &= -D^i (D_j D^j \partial_t A_i - D_i \partial_t \Gamma) - 4\pi \partial_t (D^i J_i + \partial_t \rho_e) \\ &= D^i (D_j D^j (E_i + D_i \Phi) - D_i (D^j D_j \Phi + 4\pi \rho_e)) \end{aligned}$$

⁷ Assuming that appropriate boundary conditions are imposed.

⁸ For simulations of black holes it may be constraint violating modes that propagate along the outward characteristic as opposed to along the normal that cause instabilities; see Lindblom and Scheel (2002).

$$= D_j D^j (D^i E_i - 4\pi\rho_e) = D_j D^j \mathcal{C}. \quad (4.31)$$

The crucial step in achieving this property has been the use of the constraint (4.3) to replace $D^i E_i$ with $4\pi\rho_e$ in (4.10). Had we not done that, then the $D^i E_i$ would cancel in (4.31), leading again to a zero propagation speed. Instead, the two terms now combine to form \mathcal{C} , yielding a wave equation with the speed of light as the characteristic speed.

If $\mathcal{C} = \partial_t \mathcal{C} = 0$ initially, then the two systems are equivalent analytically, since both will guarantee that $\mathcal{C} = 0$ in the domain of dependence of the initial surface. Numerically, the two systems behave very differently, since finite difference error will lead to a constraint violation $|\mathcal{C}| > 0$. Solving Maxwell's equations in primitive form, such a constraint violation will not propagate and will remain constant. As the model problem of Alcubierre *et.al.* (2000b) suggests, this behavior will lead to instabilities when nonlinear sources are included. Using the modified evolution equations (4.1), (4.9) and (4.10), the constraint violation \mathcal{C} propagates with the speed of light, will leave the numerical grid very quickly, and will ultimately leave behind $\mathcal{C} = 0$. This behavior has been verified in numerical implementations of the two systems (Knapp, Walker and Baumgarte, 2002).

The addition of the constraints to the evolution equations is by no means unique to the BSSN system. Detweiler (1987) pointed out that constraint violations can be controlled by adding the constraints to the ADM evolution equations. Frittelli (1997) demonstrated the importance of the propagation of constraints in unconstrained evolution calculations, and showed how this is linked to adding the Hamiltonian constraint to the evolution equations. Other groups have experimented with adding the momentum constraints to the ADM equations and have found stabilizing effects (Detweiler, 1987; Yoneda and Shinkai, 2001b; Shinkai and Yoneda, 2002; Kelly *et.al.*, 2001). Similarly, the derivation of many of the hyperbolic systems in Section 4.2 involve an addition of the constraints to the original equations.

5 Choosing Coordinates

Before the evolution equations as derived in Section 4 can be integrated for a set of initial data as constructed in Section 3, suitable coordinate conditions have to be chosen. In the framework of the ADM equations, the coordinate conditions are imposed with the help of the lapse α and the shift vector β^i , which determine how the coordinates evolve from one spatial slice to the next. Often, choices for the lapse are referred to as “slicing conditions”, while choices for the shift are called “spatial gauge conditions”. In the following we will discuss several different slicings and spatial gauges that have recently been

popular in $3 + 1$ numerical relativity. Parts of this Section are based on the lecture notes of Baumgarte, Shapiro and Abrahams (1998).

5.1 Geodesic Slicing

Since we are free to choose any lapse and shift, we might be tempted to make the particularly simple choice

$$\alpha = 1, \quad \beta^i = 0. \quad (5.1)$$

For constant lapse the acceleration of normal observers vanishes according to equation (2.22), and for zero shift normal observers and coordinate observers coincide. For this choice of the lapse and shift, coordinate observers are therefore freely falling and follow geodesics, which explains the name *geodesic slicing*⁹.

Example 5.1 *In geodesic slicing, the metric (2.60) of Example 2.1 reduces to*

$$ds^2 = -dt^2 + \psi^4(dr^2 + r^2(d\theta^2 + \sin^2\theta d\phi^2)), \quad (5.2)$$

which can be identified with the flat Robertson-Walker metric in spherical coordinates. If one further assumes that a homogeneous and isotropic perfect fluid is comoving with the coordinate observers, it is easy to show that the constraint and evolution equations (2.44) to (2.47) are equivalent to the well-known Friedmann equations.

Unfortunately, geodesic slicing is a particularly poor choice for most numerical simulations. In a Schwarzschild spacetime every coordinate observer, if starting from rest, will fall into the singularity in a finite time, leaving only very little time until the numerical simulation would break down (see, e.g., the discussion in Smarr and York (1978b)). To make matters worse, coordinate observers are not only attracted to physical singularities, but also tend to form coordinate singularities. This behavior is well known for the evolution of even small amplitude gravitational waves. To illustrate this property, imagine a small gravitational wave packet located originally at the origin of the coordinate system. After a short time the wave packet will have dispersed, leaving behind a flat spacetime. The coordinate observers will initially be attracted by the mass-energy of the gravitational wave packet, and will continue to coast toward the origin of the coordinate system even after the gravitational waves

⁹ Sometimes these coordinates are also called *Gaussian-normal* coordinates

have disappeared. They will intersect after a finite time and form a coordinate singularity.

This behavior can also be understood from equation (2.49), which reduces to

$$\partial_t K = K_{ij} K^{ij} = A_{ij} A^{ij} + \frac{1}{3} K^2 \quad (5.3)$$

for geodesic slicing in vacuum. The right hand side is non-negative, and once a positive value of K has been induced by any small perturbation it will continue to grow without bound. Assuming $K = K_0$ at $t = 0$ and $A_{ij} = 0$, one finds $K = 3K_0/(3 - K_0 t)$, indicating that a coordinate singularity forms at $t = 3/K_0$. Clearly, the usefulness of geodesic slicing is very limited (see also Shibata and Nakamura (1995); Anninos *et.al.* (1995c)).

5.2 Maximal Slicing

The above considerations suggest that the pathologies of geodesic slicing can be avoided by imposing a condition on the trace of the extrinsic curvature K . The most popular such choice is to set $K = 0$ at all times, which implies $\partial_t K = 0$. Equation (2.49) then yields an equation for the lapse α

$$D^2 \alpha = \alpha \left(K_{ij} K^{ij} + 4\pi(\rho + S) \right). \quad (5.4)$$

Example 5.2 *As we have seen in Section 3.3, the maximal slicing condition (5.4) can be combined with the Hamiltonian constraint (3.12) to yield equation (3.26) for the product $\alpha\psi$. Returning to Example 3.3, we find that all terms on the right hand side of (3.26) vanish: $\bar{A}_{ij} = 0$ because of time symmetry and equation (3.6), $\bar{R} = 0$ because the background metric is flat, and $\rho = S = 0$ because of vacuum. The resulting equation*

$$\bar{D}^2(\alpha\psi) = 0 \quad (5.5)$$

can therefore be solved very easily. Using (3.18) and choosing boundary conditions such that $\alpha = 1$ for $r \rightarrow \infty$ and $\alpha = 0$ on the black hole horizon $r = M/2$ we find

$$\alpha = \frac{1 - M/(2r)}{1 + M/(2r)}. \quad (5.6)$$

With $\beta^i = 0$, the conformal factor given by (3.18) and the lapse by (5.6), the

metric (2.60) now reduces to

$$ds^2 = -\frac{1 - M/(2r)}{1 + M/(2r)} dt^2 + \left(1 + \frac{M}{2r}\right)^4 (dr^2 + r^2 d\Omega^2), \quad (5.7)$$

which, as expected, is the well-known Schwarzschild metric in isotropic coordinates.

It can be shown that maximal slicing extremizes the volume of spatial slices spanned by a set of normal observers. A familiar example in Euclidian, three-dimensional space is a soap film suspended by a wire loop. Neglecting gravity, surface tension will minimize the area of the soap film, and as a consequence the trace of its extrinsic curvature vanishes (as Problem 9.31 in Lightman *et.al.* (1975) demonstrates).

From equation (2.13) we find that in maximal slicing the convergence of normal observers vanishes, $\nabla_a n^a = 0$, implying that the normal congruence is convergence free. This property prevents the focusing of normal observers that we found in geodesic slicing.

In strong field regions, this condition will tend to hold back the evolution of the slice, and will make proper time “advance more slowly”. This property is called *singularity avoidance*, and is very desirable for many numerical applications (see also Section 8.1 and Figure 8.1). Maximal slices starting at $v = 0$ in a Kruskal diagram, for example, never reach the singularity and asymptotically approach a limit surface at $R = 3M/2$ (in Schwarzschild coordinates, see Estabrook *et.al.* (1973); Smarr and York (1978b); Eardley and Smarr (1979)). Unlike in geodesic slicing, the entire exterior of the black hole can be covered.

The properties of maximal slicing have also been studied in a simple model problem (Smarr and York, 1978b; York, 1979). Among other things, this short calculation reveals that at late times of an approach to a singularity, maximal slicing makes the lapse fall off exponentially, which is commonly referred to as “the collapse of the lapse”. Numerically, this collapse of the lapse has been observed in many calculations, including Evans (1984); Shapiro and Teukolsky (1985b); Petrich, Shapiro and Teukolsky (1985).

While all these properties are very desirable, maximal slicing also has disadvantages. Equation (5.4) is an elliptic equation for the lapse function α , and in particular in three spatial dimensions solving elliptic equations is very expensive computationally. Since maximal slicing is only a coordinate condition, physical results of a simulation should not be affected if the maximal slicing condition is solved only approximately. This suggests that, instead of solving an elliptic equation, one could convert that equation into a parabolic equation, which is much faster to solve numerically (Balakrishna *et.al.*, 1996; Shibata,

1999a). As a first step, it may be advantageous to write the maximal slicing equation as

$$\partial_t K = -cK, \quad (5.8)$$

instead of $\partial_t K$, since this prescription will “drive” K back to zero in case numerical errors cause it to deviate from zero in the course of some evolution. Here c is a positive number of order unity. Inserting (2.49) then yields

$$D^2\alpha - \alpha \left(K_{ij}K^{ij} + 4\pi(\rho + S) \right) - \beta^i D_i K = cK. \quad (5.9)$$

This equation may now be solved by rewriting it as a parabolic equation by adding a “time” derivative of α

$$\partial_\lambda \alpha = D^2\alpha - \alpha \left(K_{ij}K^{ij} + 4\pi(\rho + S) \right) - \beta^i D_i K - cK, \quad (5.10)$$

where λ is an appropriately chosen “time” parameter. If this equation is evolved to “late” enough λ for every timestep so that convergence $\partial_\lambda \alpha = 0$ is achieved, then equation (5.8) is solved and K will be driven toward zero. This approximate implementation of maximal slicing is sometimes referred to as “K-driver” (Balakrishna *et.al.*, 1996) and sometimes as “approximate maximal slicing” or AMS (Shibata, 1999a; Shibata and Uryū, 2000a). While this approach seems very appealing, it also requires some fine-tuning of the parameters c and λ . Moreover, achieving convergence of the parabolic equation (5.10) may require a fair number of iteration steps. Most elliptic solvers that one would use to solve the elliptic equation (5.4) directly also involve iterative algorithms, and in order to save computer time one could limit those to just a few iteration steps also. One can therefore think of both approaches as taking a few iteration steps toward an approximate maximal slicing solution.

5.3 Harmonic Coordinates and Variations

Another particularly simple choice of coordinates is *harmonic coordinates*, for which the coordinates x^a are harmonic functions

$$\nabla^2 x^a = 0. \quad (5.11)$$

It can be shown that this condition is equivalent to

$${}^{(4)}\Gamma^a \equiv g^{bc} {}^{(4)}\Gamma_{bc}^a = 0, \quad (5.12)$$

where ${}^{(4)}\Gamma_{bc}^a$ is the connection associated with the spacetime metric g_{ab} . Inserting the metric (2.39) into (5.12) shows that in harmonic coordinates the lapse and shift satisfy the coupled set of hyperbolic equations

$$(\partial_t - \beta^j \partial_j) \alpha = -\alpha^2 K \quad (5.13)$$

$$(\partial_t - \beta^j \partial_j) \beta^i = -\alpha^2 \left(\gamma^{ij} \partial_j \ln \alpha + \gamma^{jk} \Gamma_{jk}^i \right) \quad (5.14)$$

(see York (1979)).

Harmonic coordinates have played an important role in the mathematical development of general relativity, since they bring the four-dimensional Ricci tensor ${}^{(4)}R_{ab}$ into a particularly simple form. In the three-dimensional case, we found in Section 4.3 that R_{ij} can be written in the form (4.26) in terms of the three-dimensional connection functions $\Gamma^i = \gamma^{jk} \Gamma_{jk}^i$. In complete analogy, ${}^{(4)}R_{ab}$ can be expressed as

$$\begin{aligned} {}^{(4)}R_{ab} = & -\frac{1}{2} g^{cd} g_{ab,cd} + g_{c(a} \partial_{b)} {}^{(4)}\Gamma^c + {}^{(4)}\Gamma^c {}^{(4)}\Gamma_{(ab)c} \\ & + 2g^{ed} {}^{(4)}\Gamma_{e(a}^c {}^{(4)}\Gamma_{b)cd} + g^{cd} {}^{(4)}\Gamma_{ad}^e {}^{(4)}\Gamma_{ecb} \end{aligned} \quad (5.15)$$

Evidently, in harmonic coordinates where ${}^{(4)}\Gamma^a = 0$ Einstein's equations reduce to a set of nonlinear wave equations (De Donder, 1921; Lanczos, 1922), which is why all of the early hyperbolic formulations are based on these coordinates (Choquet-Bruhat, 1952; Fischer and Marsden, 1972).

Completely harmonic coordinates have been adopted in only few three-dimensional simulations (Landry and Teukolsky, 1999; Garfinkle, 2002). More popular is so-called *harmonic slicing*, in which only the time-component ${}^{(4)}\Gamma^0$ is set to zero. Combining harmonic slicing with zero shift yields a particularly simple equation for the lapse,

$$\partial_t \alpha = -\alpha^2 K, \quad (5.16)$$

which, after inserting (2.48) for αK , can be integrated to

$$\alpha = C(x^i) \gamma^{1/2}. \quad (5.17)$$

Here $C(x^i)$ is a constant of integration that may depend on the spatial coordinates x^i , but not on time. This condition is identical to keeping the densitized lapse $\hat{\alpha} = \gamma^{-1/2} \alpha$ (see equation (4.16)) constant.

Example 5.3 *For the Schwarzschild metric (5.7) of Example 5.2, K , β^i and $\partial_t \alpha$ are all zero. It is therefore obvious that the maximally sliced Schwarzschild*

spacetime in isotropic coordinates is simultaneously harmonically sliced. For numerical purposes, it may be undesirable that the lapse (5.6) vanishes on the event horizon at $r = M/2$. Well-behaved harmonic slices, for which the lapse does not vanish on the horizon, have been constructed by Bona and Massó (1988) and Cook and Scheel (1997).

The harmonic slicing condition (5.17) is just about as simple as the geodesic slicing condition (5.1), but it provides for a much more stable numerical evolution (see, e.g., Shibata and Nakamura (1995); Baumgarte and Shapiro (1999)). It does not focus coordinate observers and, as Example 5.3 suggests, metric components of static solutions are independent of time in harmonic slicing, hence allowing for long time evolutions (e.g. Cook and Scheel (1997); Baumgarte, Hughes and Shapiro (1999)). However, there is no guarantee that harmonic slicing will lead to well-behaved coordinates in more general situations (see, e.g. Alcubierre (1997); Alcubierre and Massó (1998); Khokhlov and Novikov (2002)) and it has been pointed out that the singularity avoidance properties of harmonic slicing are weaker than those of, for example, maximal slicing (e.g. Shibata and Nakamura (1995); cf. Garfinkle (2002)).

Equation (5.17) is an example of an algebraic coordinate condition, in which the lapse can be found algebraically, without having to solve complicated and computer intensive differential equations as for maximal slicing. A generalization of that condition has been suggested by Bona, Massó, Seidel and Stela (1995)

$$\partial_t \alpha = -\alpha^2 f(\alpha) K, \quad (5.18)$$

where $f(\alpha)$ is a positive but otherwise arbitrary function of α . For $f = 1$ this condition obviously reduces to harmonic slicing. For $f = 0$ (and $\alpha = 1$ initially), it reduces to geodesic slicing (Section 5.1). Formally, maximal slicing (Section 5.2) corresponds to $f \rightarrow \infty$. For $f = 2/\alpha$ the condition (5.18) can be integrated to yield

$$\alpha = 1 + \ln \gamma, \quad (5.19)$$

where we have used (2.48) and chosen a constant of integration to be unity. This quite popular slicing condition is often called “1 + log” slicing (Bernstein, 1993; Bona, Massó, Seidel and Stela, 1995), and has been used in various applications (including Anninos *et.al.* (1995c); Bona, Massó, Seidel and Walker (1998); Alcubierre *et.al.* (2001a); Font *et.al.* (2001)). As an algebraic slicing condition it has the virtue of being extremely simple to implement and fast to solve. It has also been found to have stronger singularity avoidance properties than harmonic slicing, which can be motivated by the fact that f becomes large when α becomes small, so that it probably behaves more like maximal

slicing than harmonic slicing. A similar slicing condition has been suggested by Shibata and Nakamura (1995) and Oohara, Nakamura and Shibata (1997) with the goal of enhancing the singularity avoidance properties of harmonic slicing.

5.4 Minimal Distortion and Variations

In Section 3 we found that the conformally related metric $\bar{\gamma}_{ij}$ has five independent functions, two of which correspond to true gravitational degrees of freedom and three to coordinate freedom. For a stable and accurate numerical evolution it is desirable to eliminate purely coordinate-related fluctuations in $\bar{\gamma}_{ij}$, which suggests that one may want to construct a gauge condition that minimizes the time change of the conformally related metric. This gauge condition is called *minimal distortion* (see Smarr and York (1978a,b), whose derivation we will follow closely).

In Section 3.3 we introduced the time derivative u_{ij} of the conformally related metric,

$$u_{ij} \equiv \gamma^{1/3} \partial_t (\gamma^{-1/3} \gamma_{ij}), \quad (5.20)$$

(equation (3.19)). Since u_{ij} is traceless, we can decompose it into a transverse-traceless and a longitudinal part

$$u_{ij} = u_{ij}^{TT} + u_{ij}^L, \quad (5.21)$$

similar to the decomposition of the traceless part of the extrinsic curvature in Section 3.2. The divergence of the transverse part vanishes

$$D^j u_{ij}^{TT} = 0, \quad (5.22)$$

and the longitudinal part can be written as

$$u_{ij}^L = D_i X_j + D_j X_i - \frac{2}{3} \gamma_{ij} D^k X_k = (LX)^{ij} \quad (5.23)$$

Since $\bar{\gamma}_{ij} = \gamma^{-1/3} \gamma_{ij}$ is a vector density of weight $-2/3$, the right hand side of (5.23) can be identified with the Lie derivative of $\bar{\gamma}_{ij}$ along the vector X^i ,

$$u_{ij}^L = \gamma^{1/3} \mathcal{L}_{\mathbf{X}} \bar{\gamma}_{ij}. \quad (5.24)$$

Evidently, the longitudinal part can be interpreted as arising from a change of coordinates, generated by X^i . It represents the coordinate effects in the time development, which can therefore be eliminated by choosing u_{ij}^L to vanish. This leaves only the transverse part u_{ij}^{TT} , which implies that the divergence of u_{ij} itself must vanish

$$D^j u_{ij} = 0. \quad (5.25)$$

Combining this with equation (3.20) yields

$$D^j (L\beta)_{ij} = 2D^j (\alpha A_{ij}) \quad (5.26)$$

or

$$(\Delta_L \beta)^i = 2A^{ij} D_j \alpha + \frac{4}{3} \alpha \gamma^{ij} D_j K + 16\pi \alpha j^i, \quad (5.27)$$

where we have replaced the divergence of A^{ij} with the momentum constraint. This is the minimal distortion condition for the shift vector β^i . This condition can also be derived by minimizing the action

$$\mathcal{A} \equiv \int u_{ij} u_{kl} \gamma^{ik} \gamma^{jl} \gamma^{1/2} d^3x \quad (5.28)$$

with respect to β^i .

It is also useful to express (5.27) in terms of conformally related quantities. Using $(L\beta)^{ij} = \psi^{-4} (\bar{L}\beta)^{ij}$ and $D_j S^{ij} = \psi^{-10} \bar{D}_j (\psi^{10} S^{ij})$ for any symmetric, traceless tensor, we find

$$(\Delta_L \beta)^i = \psi^{-4} \left((\bar{\Delta}_L \beta)^i + (\bar{L}\beta)^{ij} \bar{D}_j \ln \psi^6 \right) \quad (5.29)$$

and hence

$$(\bar{\Delta}_L \beta)^i + (\bar{L}\beta)^{ij} \bar{D}_j \ln \psi^6 = 2\tilde{A}^{ij} \bar{D}_j \alpha + \frac{4}{3} \alpha \bar{\gamma}^{ij} \bar{D}_j K + 16\pi \psi^4 \alpha j^i. \quad (5.30)$$

Here we have used the rescaling (4.19) of Section 4.3 for \tilde{A}^{ij} .

Evidently, the minimal distortion condition (5.30) is fairly involved and quite difficult to solve numerically. Shibata (1999c) therefore suggested simplifying the condition. Just as was the case maximal slicing, simplifying is justified

because the condition is only a coordinate condition. We may hope that minimal distortion has properties that are advantageous for numerical implementations, but small modifications of the conditions may still lead to similarly desirable properties.

Shibata (1999c) suggested modifying (5.30) in two steps. In the first step, we can express \tilde{A}^{ij} in terms of $(\bar{L}\beta)^{ij}$ as

$$\tilde{A}^{ij} = \frac{1}{2\alpha} \left((\bar{L}\beta)^{ij} - \psi^{-4} u^{ij} \right). \quad (5.31)$$

(compare equation (3.22)). Assuming $u_{ij} = 0$ in this expression, and inserting into (5.30) we find

$$(\bar{\Delta}_L\beta)^i = 2\alpha\tilde{A}^{ij}\bar{D}_j \ln(\alpha\psi^{-6}) + \frac{4}{3}\alpha\bar{\gamma}^{ij}D_j K + 16\pi\psi^4\alpha j^i. \quad (5.32)$$

Alternatively, this expression can be derived by modifying the original condition (5.25), $D^i u_{ij} = 0$, which is equivalent to $\bar{D}^i(\psi^2 u_{ij}) = 0$, to

$$\bar{D}^i(\psi^{-4} u_{ij}) = 0 \quad (5.33)$$

(Shibata, 1999c). Note that the condition (5.32) is identical to the shift condition (3.28) that we found in the thin sandwich approach with $u_{ij} = 0$, $K = 0$ and conformal flatness (Section 3.3). The assumptions of the thin sandwich approach hence leads to the minimal distortion condition for the shift.

In the second step Shibata (1999c) simplifies the operator $(\bar{\Delta}_L\beta)^i$ in (5.32) by replacing it with the flat vector Laplacian $(\Delta_L^{\text{flat}}\beta)^i$, so that in Cartesian coordinates the covariant derivatives can be replaced with partial derivatives. This condition is called the “approximate minimal distortion” (AMD) condition, and has been used successfully in various applications (Shibata, 1999a,c; Shibata and Uryū, 2000a; Shibata, Baumgarte and Shapiro, 2000a,b). Strategies for solving the flat vector Laplacian are discussed in Appendix B.

In collapse situations, however, Shibata (1999c) showed that minimal distortion leads to shift vectors that point outwards, leading to coordinate points being shifted outward, and hence to a coarser resolution at the center of the collapse. This is clearly not desirable, because one would probably want an increasingly fine resolution at the center of the collapse. Shibata (1999c) experimented with various ways of adding an artificial radial component to the shift, which compensates this effect and improves the numerical performance.

A gauge condition that is closely related to minimal distortion is based on the conformal connection function $\bar{\Gamma}^i$ of the BSSN formulation (Section 4.3).

These functions could be set to zero, which would result in “conformal three-harmonic” coordinates (compare Section 5.3). Instead, Alcubierre and Brügmann (2001) suggested setting their time-derivative to zero,

$$\partial_t \bar{\Gamma}^i = 0. \quad (5.34)$$

Inserting this into (4.28) leads to the “Gamma freezing” condition

$$\begin{aligned} & \bar{\gamma}^{lj} \beta_{,lj}^i + \frac{1}{3} \bar{\gamma}^{li} \beta_{,jl}^j + \beta^j \partial_j \bar{\Gamma}^i - \bar{\Gamma}^j \partial_j \beta^i + \frac{2}{3} \bar{\Gamma}^i \partial_j \beta^j \\ & = 2 \tilde{A}^{ij} \partial_j \alpha - 2\alpha \left(\bar{\Gamma}_{jk}^i \tilde{A}^{kj} - \frac{2}{3} \bar{\gamma}^{ij} \partial_j K - \bar{\gamma}^{ij} S_j + 6 \tilde{A}^{ij} \partial_j \phi \right). \end{aligned} \quad (5.35)$$

The relation to minimal distortion can be seen by inserting (4.25) into the condition (5.34), which yields

$$\partial_j \partial_t \bar{\gamma}^{ij} = \partial_j (\psi^4 u^{ij}) = 0 \quad (5.36)$$

(compare with the divergence conditions (5.25) and (5.33)). To simplify the numerical implementation of condition (5.35), Alcubierre and Brügmann (2001) converted the elliptic equation into a parabolic one,

$$\partial_t \beta^i = k \partial_t \bar{\Gamma}^i, \quad (5.37)$$

where k is positive and where (4.28) should be inserted for $\partial_t \bar{\Gamma}^i$. In analogy to the “K-driver” of Balakrishna *et.al.* (1996) (see Section 5.2), this condition has been called the “Gamma driver” condition. Alcubierre *et.al.* (2001b) also experimented with a hyperbolic version

$$\partial_t^2 \beta^i = \psi^{-4} k \partial_t \bar{\Gamma}^i - \eta \partial_t \beta^i, \quad (5.38)$$

where both k and η are positive constants.

Another gauge condition that is closely related to minimal distortion is the *minimal shear* or *minimal strain* condition, in which the time change of the physical metric γ_{ij} (as opposed to the conformal metric) is minimized in the action (5.28). Brady, Creighton and Thorne (1998) suggested to combine this condition with a similar condition for the lapse to construct “comoving” coordinates that are particularly well suited for simulations of the slow inspiral outside of the ISCO (see also Garfinkle and Gundlach (1999) and Garfinkle *et.al.* (2000)).

6 Locating Black Hole Horizons

A black hole is defined as a region of spacetime out of which no null geodesics can escape to infinity. The *event horizon*, or surface of the black hole, is the boundary between those events which can emit light rays to infinity and those which cannot. More formally, it is defined as the boundary of the causal past of future infinity (see, e.g., Hawking and Ellis (1973); Wald (1984)). It is formed by those outward-going, future-directed null geodesics which neither escape to infinity nor fall toward the center of the black hole. The event horizon is obviously a gauge-invariant entity, and contains important geometric information about the spacetime. Unfortunately, its global properties make it very difficult to locate, since, in principle, knowledge of the entire future spacetime is required to decide whether or not any particular null geodesic will ultimately escape to infinity or not. An event horizon can therefore at best be found “after the fact”, meaning after an evolution calculation has evolved to some stationary state.

Locating event horizons after the completion of a calculation may be sufficient for diagnostic purposes, for analyzing the geometrical and astrophysical results of a black hole simulation, but locating black holes in numerical simulations is also important for a more technical reason. The spacetime singularities at the center of black holes have to be excluded from the numerical grid, since they would otherwise spoil the numerical calculation (see also Section 8.1). As we have seen in Section 4, spacetime slicings can be chosen so that they avoid singularities (for example maximal slicing, Section 4.2). Typically, however, these slices quickly develop grid pathologies which also cause numerical codes to crash. Realizing that the interior of a black hole can never influence the exterior suggests an alternative solution, namely “excising” a spacetime region just inside the event horizon from the numerical domain (Unruh, 1984). This approach requires at least approximate knowledge of the location of the horizon at all times during the evolution, and the construction of the event horizon after the fact is therefore not sufficient.

In practice one therefore locates *apparent horizons* during the evolution. The apparent horizon is defined as the outermost smooth 2-surface, embedded in the spatial slices Σ , whose outgoing null geodesics have zero expansion. As we will see, the apparent horizon can be located on each slice Σ , and is therefore a local-in-time concept. The singularity theorems of general relativity (see, e.g., Hawking and Ellis (1973); Wald (1984)) tell us that if an apparent horizon exists on a given time slice, it must be inside a black hole event horizon. This makes it safe to excise the interior of an apparent horizon from a numerical domain¹⁰. Note, however, that the absence of an apparent horizon

¹⁰ This is not necessarily true in other theories of gravity. In Brans-Dicke theory,

does not necessarily imply that no black hole is present. It is possible, for example, to construct slicings of the Schwarzschild geometry in which no apparent horizon exists (Wald and Iyer, 1991). The latter clearly demonstrates the gauge-dependent nature of the apparent horizon. In numerical simulations, one simply hopes that the chosen slices are sufficiently non-pathological, and that the apparent horizon is reasonably close to the event horizon. This is the case, for example, for stationary situations, for which the apparent horizon and the event horizon coincide.

Recently, the concept of *isolated horizons* has also been introduced (see, e.g., Ashtekar, Beetle and Fairhurst (1999); Ashtekar *et.al.* (2000)), and the first implementations in numerical relativity have been reported in Dreyer *et.al.* (2002).

6.1 Locating Apparent Horizons

Example 6.1 *In spherical symmetry, the concept of an apparent horizon is quite transparent, and can be illustrated very easily. The apparent horizon is defined as the boundary of the region of trapped surfaces, wherein the cross-sectional area spanned by a beam of outgoing light rays immediately evolves to a smaller area.*

For the metric (2.60), an outgoing light ray satisfies

$$\frac{dr}{dt} = \frac{\alpha}{\psi^2} - \beta, \quad (6.1)$$

and the areal radius is given by $\psi^2 r$. The apparent horizon condition can therefore be found from the condition that the total time derivative of $\psi^2 r$ along the right ray vanish

$$\begin{aligned} \frac{d}{dt}(\psi^2 r) &= \frac{\partial}{\partial t}(\psi^2 r) + \frac{dr}{dt} \frac{\partial}{\partial r}(\psi^2 r) \\ &= 2r\dot{\psi}^2 \left(\frac{\dot{\psi}}{\psi} - \beta \frac{\psi'}{\psi} - \frac{\beta}{2r} \right) + 2r\alpha \frac{\psi'}{\psi} + \alpha = 0. \end{aligned} \quad (6.2)$$

The expression in brackets can be rewritten in terms of the extrinsic curvature

for example, apparent horizons may exist outside of event horizons, so that only a part of the region inside the apparent horizon can be excised (see Scheel, Shapiro and Teukolsky (1995b) for a numerical example).

(2.62), which yields

$$-\psi^2 r K^\theta_\theta + 2 \frac{\psi'}{\psi} r + 1 = 0. \quad (6.3)$$

This condition can be evaluated very easily. For the Schwarzschild solution (3.18), for example, one readily verifies that the apparent horizon coincides with the event horizon at $r = m/2$.

Consider a closed smooth hypersurface of Σ , and call it S . By construction, S is spatial and two-dimensional. Let s^a be its unit outward pointing normal in Σ . Obviously s^a then satisfies $s_a s^a = 1$ and $s^a n_a = 0$. Similarly to how the spacetime metric g_{ab} induces the spatial metric γ_{ab} on Σ (see Section 2.1), the latter now induces a two-dimensional metric

$$m_{ab} = \gamma_{ab} - s_a s_b = g_{ab} + n_a n_b - s_a s_b \quad (6.4)$$

on S . We now consider the outgoing future-pointing null geodesics whose projection on Σ is orthogonal to S . Up to an overall factor, the tangents k^a to these geodesics can be constructed, on S , from

$$k^a = s^a + n^a, \quad (6.5)$$

which automatically satisfies $k_a k^a = 0$ and $m_{ab} k^a = 0$. We parallel propagate k^a away from S with the geodesic equation $k^a \nabla_a k^b = 0$. A *marginally trapped surface* (or sometimes called marginally outer-trapped surface) is now defined as a surface on which the expansion Θ of the outgoing null geodesics orthogonal to S vanishes everywhere¹¹

$$\Theta = \nabla_a k^a = 0. \quad (6.6)$$

The outermost such surface is called the *apparent horizon*.

For the purposes of numerical relativity, it is useful to rewrite this equation in terms of three-dimensional objects. To do so, we insert (6.5) into (6.6), which yields

$$\Theta = \nabla_a (n^a + s^a) = -K + \nabla_a s^a \quad (6.7)$$

where we have used equation (2.13). The divergence of s^a can now be rewritten

¹¹ Note that this condition is equivalent to $m^{ab} \nabla_a k_b = 0$.

$$\begin{aligned}\nabla_a s^b &= g^a_b \nabla_a s^b = (\gamma^a_b - n^a n_b) \nabla_a s^b = D_i s^i - n^a n_b \nabla_a s^b \\ &= D_i s^i + n^a s^b \nabla_a n_b = D_i s^i + s^i s^j K_{ij} + k^a s^b \nabla_a n_b.\end{aligned}\tag{6.8}$$

The last term vanishes identically, as can be seen by inserting (6.5) again,

$$k^a s^b \nabla_a n_b = s^b k^a \nabla_a k_b - k^a s^b \nabla_a s_b = 0.\tag{6.9}$$

We can now combine results to find the apparent horizon equation

$$\Theta = D_i s^i - K + s^i s^j K_{ij} = 0,\tag{6.10}$$

which can also be written as

$$\Theta = m^{ij}(D_i s_j - K_{ij}) = 0.\tag{6.11}$$

(cf. York (1989) and Gundlach (1998)). This condition only depends on spatial quantities defined within each slice Σ , which makes it obvious that it can be constructed “locally in time” on each slice.

Example 6.2 *We can now verify that condition (6.11) leads to (6.3) in spherical symmetry. In this case, s^a only has a radial component, $s^r = \psi^{-2}$, and the only non-vanishing components of m^{ij} are $m^{\theta\theta} = \gamma^{\theta\theta}$ and $m^{\phi\phi} = \gamma^{\phi\phi}$. The term $m^{ij}K_{ij}$ is therefore*

$$m^{ij}K_{ij} = K^\theta_\theta + K^\phi_\phi = 2K^\theta_\theta,\tag{6.12}$$

and $m^{ij}D_i s_j$ reduces to

$$m^{ij}D_i s_j = m^{ij}(s_{j,i} - \Gamma^k_{ij}s_k) = \frac{2}{\psi^2 r} \left(2 \frac{\psi'}{\psi} r + 1 \right),\tag{6.13}$$

where we have used the connection coefficients (2.61). Inserting the last two equations into the condition (6.11) immediately yields (6.3), as expected.

Various different methods have been employed to locate apparent horizons. Most of these methods have in common that they characterize the horizon as a level surface of a scalar function, e.g.

$$\tau(x^i) = 0.\tag{6.14}$$

The unit normal s^a can then be expressed as

$$s^i = \lambda \gamma^{ij} D_j \tau\tag{6.15}$$

where λ is the normalization factor

$$\lambda \equiv (\gamma^{ij} D_i \tau D_j \tau)^{-1/2}. \quad (6.16)$$

Inserting these into equation (6.11) yields

$$\Theta = m^{ij} (\lambda D_i D_j \tau - K_{ij}). \quad (6.17)$$

The expansion Θ is therefore a second order differential operator on τ . The principal part of this operator is the Laplace operator with respect to the two-dimensional metric m_{ij} on S (see also the discussion in Gundlach (1998)).

Most authors have chosen τ to be of the form¹²

$$\tau(x^i) = r_C(x^i) - h(\theta, \phi), \quad (6.18)$$

where r_C is the coordinate separation between the point x^i and some location C^i inside the $\tau = 0$ surface, and where θ and ϕ are polar coordinates centered on C^i . In fact, most authors assume that C^i is the origin of the coordinate system, $C^i = 0$. The function h measures the coordinate distance from C^i to the $\tau = 0$ surface in the direction (θ, ϕ) .

Inserting (6.18) into (6.17) yields a second order differential operator on $h(\theta, \phi)$ (which, when considered as a differential operator in two dimensions, is elliptic). In spherical symmetry, where h is a constant, the problem reduces to solving an algebraic equation, as we have seen in Examples 6.1 and 6.2. In axisymmetry h only depends on θ , and equation (6.17) becomes an ordinary differential equation which has to be solved with periodic boundary conditions. Solutions have been constructed with shooting methods (for example Čadež (1974); Bishop (1984); Shapiro and Teukolsky (1992)), spectral methods (Eppley, 1977) and finite difference methods (Cook and York, 1990). Both spectral and finite difference methods have also been employed in three-dimensional problems, without any simplifying symmetry assumptions.

Nakamura, Kojima and Oohara (1984) (also Nakamura, Kojima and Oohara (1985)) adopt a spectral method. They expand h in spherical harmonics

$$h(\theta, \phi) = \sum_{l=0}^{l_{\max}} \sum_{m=-l}^l a_{lm} Y_{lm}(\theta, \phi) \quad (6.19)$$

and construct an iterative algorithm to determine the expansion coefficients

¹² This choice restricts the topology of S to S^2 , and S must furthermore be star-shaped around C^i (compare the discussion in Gundlach (1998)).

a_{lm} , which is most easily explained in the notation of Gundlach (1998). Recall that the principal part of the nonlinear operator Θ acting on h is a two-dimensional Laplacian with respect to m_{ij} . The key idea is introduce a linear elliptic operator, which is easier to invert, and to subtract it from the nonlinear one. Nakamura, Kojima and Oohara (1984) use the flat Laplacian on a 2-sphere,

$$L^2 h \equiv h_{,\theta\theta} + \cot \theta h_{,\theta} + \sin^{-2} \theta h_{,\phi\phi} \quad (6.20)$$

and rewrite the equation $\Theta = 0$ as

$$L^2 h = \rho \Theta + L^2 h. \quad (6.21)$$

Here the scalar function ρ is chosen so that the partial derivative $h_{,\theta\theta}$ cancels on the right hand side (see Gundlach (1998) for a generalization). Since $L^2 Y_{lm} = -l(l+1)Y_{lm}$, we can now multiply both sides with Y_{lm}^* and integrate over S to find

$$-l(l+1) a_{lm} = \int_S Y_{lm}^* (\rho \Theta + L^2 h) d\Omega, \quad (6.22)$$

where $d\Omega = \sin \theta d\theta d\phi$, and where we have used the orthogonality of the spherical harmonics. A priori, this equation is not very helpful, since the right hand side has to be evaluated at S , which depends on the very a_{lm} that we would like to determine. However, equation (6.22) can now be used to define an iteration procedure, in which the integral on the right hand side is evaluated using a previous set of guesses a_{lm}^n to determine a new set a_{lm}^{n+1} . Obviously, this algorithm works only for $l \geq 1$, and a_{00} has to be determined independently from the integral on the right hand side alone. A similar scheme has been implemented by Kembell and Bishop (1991).

A variant of the spectral method, in which the problem of finding a root of Θ is reduced to a multi-dimensional minimization problem, was proposed by Libson *et.al.* (1996a) and implemented independently by Baumgarte *et.al.* (1996) and Anninos *et.al.* (1998). In this approach, Θ^2 is integrated over S

$$\mathcal{S} = \int_S \Theta^2 d\sigma, \quad (6.23)$$

where $d\sigma$ is the proper area element on S . The function h is again expanded as in (6.19)¹³, so that \mathcal{S} becomes a function of the expansion coefficients a_{lm} . A standard minimization method is then used to vary the a_{lm} until a minimum

¹³ Except that these authors expand h in terms of symmetric traceless tensors in-

of \mathcal{S} has been found. An apparent horizon has been located if \mathcal{S} , according to some appropriate criterion, is sufficiently close to zero.

Shibata (1997) (also Shibata and Uryū (2000b)) uses the same ansatz (6.21) as Nakamura, Kojima and Oohara (1984), but employs a finite difference method instead of a spectral method to solve it. In particular, S is covered with a finite difference grid (θ_i, ϕ_j) , on which $h(\theta, \phi)$ is represented as $h_{i,j}$. The operator (6.20) is then finite differenced in a straight-forward, second-order fashion

$$(L^2 h)_{i,j} = \frac{h_{i+1,j} - 2h_{i,j} + h_{i-1,j}}{(\Delta\theta)^2} + \cot\theta_i \frac{h_{i+1,j} - h_{i-1,j}}{2\Delta\theta} + \sin^{-2}\theta_i \frac{h_{i,j+1} - 2h_{i,j} + h_{i,j-1}}{(\Delta\phi)^2}. \quad (6.24)$$

Equation (6.21) can again be solved using an iterative algorithm. On the right hand side, the operator (6.24) can be evaluated for a previous set of values $h_{i,j}^n$. On the left hand side, the same operator acts on the new values $h_{i,j}^{n+1}$. Evaluating (6.21) at all gridpoints (θ_i, ϕ_j) then yields a coupled set of linear equations for the $h_{i,j}^{n+1}$, which can be solved with standard techniques of matrix inversion (e.g. Press *et.al.* (1992)).

Thorneburg (1996) and Huq, Choptuik and Matzner (2000) have also implemented finite difference methods to locate apparent horizons. They, however, do not use the ansatz (6.21), and instead finite difference the nonlinear equation $\Theta = 0$ directly. The resulting nonlinear system of equations is then solved with Newton's method. A similar method has been used by Schnetter (2002), except that here the tensor fields on the horizon are represented in Cartesian coordinate components.

Yet another method, a curvature flow method, was proposed by Tod (1991). This method is related to solving an elliptic equation by converting it into a parabolic equation. During the evolution in an unphysical “time” parameter, the solution of the parabolic problem settles down into an equilibrium solution, which is the solution to the original elliptic problem. Similarly, Tod (1991) proposes to deform a trial surface S according to

$$\frac{\partial x^i}{\partial \lambda} = -s^a \Theta, \quad (6.25)$$

where λ is the unphysical time parameter. For time-symmetric data with $K_{ij} = 0$, Θ reduces to the trace of the extrinsic curvature of S in Σ , $D_i s^i$. The apparent horizon then satisfies $D_i s^i = 0$ and is therefore a minimal surface

stead of spherical harmonics, which is completely equivalent, but more convenient in Cartesian coordinates.

(compare Problem 9.31 in Lightman *et.al.* (1975)), for which Tod's method is known to converge. For general data, the flow (6.25) is no longer guaranteed to converge, but numerical experience shows that in general it still does. Implementations of Tod's method have been described in a number of unpublished reports (see, e.g. Gundlach (1998) and Shoemaker, Huq and Matzner (2000) for references).

Gundlach (1998) generalizes the flow prescription (6.25) and describes a new family of spectral algorithms which include the methods of Tod (1991) and Nakamura, Kojima and Oohara (1984) as special cases for particular values of certain parameters. It is suggested that other algorithms in this family may combine the robustness of the former with the speed of the latter.

Alcubierre *et.al.* (2000c) have compared the algorithm of Gundlach (1998) with the minimization method of Anninos *et.al.* (1998) for a number of different test problems, without finding clear advantages of one algorithm over the other. The spectral method of Gundlach (1998) is reported to be generally much faster than the minimization routine, but the efficiency of the latter could probably be improved dramatically. Both Anninos *et.al.* (1998) and Baumgarte *et.al.* (1996) employ Powell's method for the multi-dimensional minimization, since it does not use derivatives of the function and is hence easy to implement. Pfeiffer, Teukolsky and Cook (2000) report on replacing Powell's method in the code of Baumgarte *et.al.* (1996) with a Davidson-Fletcher-Powell algorithm (see Press *et.al.* (1992)) and find a significant speed-up.

Shoemaker, Huq and Matzner (2000) implement a finite difference version of a flow description with is also a slightly generalized version of (6.25). They also introduce a so-called level flow, in which the flow proceeds to a surface of constant, but not necessarily zero expansion Θ . The apparent horizon is then located by constructing a sequence of such surfaces, including the case $\Theta = 0$. This approach may have certain advantages for handling situations in which multiple apparent horizons are present.

6.2 Locating Event Horizons

Event horizons, formally defined as the boundary of the causal past of future infinity, are traced out by outgoing light rays that never reach future null infinity and never hit the singularity. In principle, therefore, knowledge of the entire future evolution of a spacetime is necessary to locate event horizons. In practice, however, event horizons can be located fairly accurately after a finite evolution time, once a spacetime has settled down to an approximately stationary state.

Hughes *et.al.* (1994) constructed an event horizon finder by evolving null geodesics

$$\frac{d^2 x^a}{d\lambda^2} + {}^{(4)}\Gamma_{bc}^a \frac{dx^b}{d\lambda} \frac{dx^c}{d\lambda} = 0, \quad (6.26)$$

where λ is an affine parameter. In $3 + 1$ form, this equation can be rewritten as

$$\frac{dp_i}{d\lambda} = -\alpha\alpha_{,i}(p^0)^2 + \beta^k{}_{,i}p_k p^0 - \frac{1}{2}\gamma^{lm}{}_{,i}p_l p_m \quad (6.27)$$

$$\frac{dx^i}{d\lambda} = \gamma^{ij}p_j - \beta^i p^0, \quad (6.28)$$

where we have used $p^i = dx^i/d\lambda$ and $p^0 = (\gamma^{ij}p_i p_j)^{1/2}/\alpha$ (which enforces $g^{ab}p_a p_b = 0$).

From each point in a numerically generated spacetime, for which the lapse α , the shift β^i and the spatial metric γ_{ij} are known on a numerical grid, light rays can then be sent out in many different directions p^i . To determine whether or not this point is inside an event horizon, Hughes *et.al.* (1994) use the additional knowledge of apparent horizons. Conceptually, if all light rays sent out from a point end up inside an apparent horizon (which is always located inside an event horizon) the point is inside the event horizon as well. If, on the other hand, at least one light ray sent out from the point escapes to large separations, the point is not inside an event horizon. In this way, the ejection and propagation of light rays from various points in spacetime can determine the location of the event horizon.

An alternative and quite attractive approach was suggested by Anninos *et.al.* (1995a) and Libson *et.al.* (1996). Realizing that the future directed light rays diverge away from the event horizon, either toward the interior of the black hole or toward future null infinity, they suggest integrating null geodesics *backwards* in time, which converge to the event horizon. In practice, Hughes *et.al.* (1994) also employ backwards integration of light rays for the same reason. This method is particularly efficient if one can identify a “horizon-containing” region in which the event horizon is expected to reside. It is then sufficient to integrate light rays from this limited region, and they will quickly be attracted by the event horizon.

Anninos *et.al.* (1995a) and Libson *et.al.* (1996) also pointed out that instead of integrating individual null geodesics, one may integrate entire null surfaces backward in time. Defining such a null surface as a level surface $f(t, x^i) = 0$, one can rewrite the null condition

$$g^{ab}\partial_a\partial_b f = 0 \quad (6.29)$$

to find an evolution equation for f

$$\partial_t f = \frac{-g^{ti}\partial_i f + \sqrt{(g^{ti}\partial_i f)^2 - g^{tt}g^{ij}\partial_i f\partial_j f}}{g^{tt}}. \quad (6.30)$$

An event horizon can then be located by evolving two such surfaces defining the inner and outer boundary of the horizon-containing region backward in time. The two surfaces will converge very quickly and will bracket the event horizon.

Examples of event horizons in numerically generated spacetimes, for example for the head-on collision of two black holes, can be found in Hughes *et.al.* (1994); Anninos *et.al.* (1995a); Matzner *et.al.* (1995) and Libson *et.al.* (1996).

7 Binary Black Hole Initial Data

In this Section we will discuss various approaches to solving the initial value equations of Section 3 for spacetimes that describe binary black holes in approximately circular orbit. Such initial data may be used as initial data for dynamical simulations of the plunge and merger, as “snapshots” of the evolutionary sequence up to the ISCO, to locate the ISCO, and finally as background models in quasi-adiabatic evolutionary calculations to simulate the late inspiral phase. For a more complete review of initial data for numerical relativity see Cook (2000).

Under sufficiently restrictive assumptions, constructing initial data containing multiple black hole is almost trivial. Recall from Example 3.3 that for conformally flat ($\bar{\gamma}_{ij} = \eta_{ij}$), time-symmetric ($K_{ij} = 0$) vacuum spacetimes ($\rho = j^i = 0$), the momentum constraint (3.13) is solved trivially and the Hamiltonian constraint (3.12) reduces to the simple Laplace equation (3.17), which, with suitable boundary conditions, has solutions of the form (3.18). Given that the Laplace equation (3.17) is linear, we can obviously add several solutions (3.18) and find

$$\psi = 1 + \sum_{\alpha} \frac{m_{\alpha}}{2r_{\mathbf{C}_{\alpha}}} \quad (7.1)$$

for an arbitrary number of black holes. Here $r_{\mathbf{C}_{\alpha}} = \|x^i - C_{\alpha}^i\|$, and C_{α}^i is the coordinate location of the α -th black hole.

However, even for two black holes this construction is not unique. We could define a coordinate mapping equivalent to that of Example 3.3 for each one of

the black holes, but would find that for each one the presence of the companion would destroy the isometry that we found for a single black hole (Linquist, 1963). In other words, we can think of the two throats as connecting one sheet or universe with two black holes with two separate asymptotically flat sheets, each one only containing one black hole. This topology is called a “three-sheeted” topology. The isometry can be restored by adding additional throats inside each one of the already existing throats, which correspond to mirror images of the companion black hole (Misner, 1963; Kulkarni, Shepley and York, 1983). This “conformal-imaging” approach leads to a two-sheeted topology, in which the two throats connect to identical, asymptotically flat sheets. It is also possible to consider a one-sheeted, but multiply connected topology, in which the two ends of a “wormhole” represent the two black holes (Misner, 1960).

The non-uniqueness of these solutions stems from the fact that Einstein’s equations determine the local geometry of a spacetime, but do not fix its topology. In more physical terms, solutions with different topologies differ by their initial gravitational wave content, which is also not determined by Einstein’s equations.

From an astrophysical point of view, the above solutions are not very interesting because they assume time-symmetry with $K_{ij} = 0$. For the construction of binary black holes in binary orbit, we will be interested in black holes with finite momenta, and hence non-vanishing extrinsic curvature. That means that the momentum constraint is no longer solved as an identity, and that the extrinsic curvature introduces a non-linear term into the Hamiltonian constraint. In the following we will discuss several different approaches to constructing such binary black hole solutions. As we have explained in Section 1, we will be particularly interested in binary black holes in *quasi-circular* orbit.

7.1 The Bowen-York Approach

In the Bowen-York approach (Bowen and York, 1980; Bowen, 1982; York, 1989), initial data are constructed using the conformal transverse-traceless decomposition of Section 3.2. Assuming maximal slicing ($K = 0$) and conformal flatness ($\bar{\gamma}_{ij} = \eta_{ij}$), the momentum constraint (3.13) reduces to

$$(\Delta_L^{\text{flat}} W)^i = 0 \tag{7.2}$$

(compare Appendix B). This equation is solved analytically by

$$W_{\mathbf{CP}}^i = -\frac{1}{4r_{\mathbf{C}}} (7P^i + n_{\mathbf{C}}^i n_{\mathbf{C}}^j P_j) \tag{7.3}$$

where $n_{\mathbf{C}}^i = (x^i - C^i)/r$ is the normal vector pointing away from the center of the black hole at C^i , and where P^i is an arbitrary vector. Constructing the extrinsic curvature from this solution then yields

$$\bar{A}_{\mathbf{C}\mathbf{P}}^{ij} = \frac{3}{2r_{\mathbf{C}}^2} \left(P^i n_{\mathbf{C}}^j + P^j n_{\mathbf{C}}^i + (\eta^{ij} + n_{\mathbf{C}}^i n_{\mathbf{C}}^j) P_k n_{\mathbf{C}}^k \right). \quad (7.4)$$

Inserting this into (3.15) shows that P^i is the linear momentum of the black hole.

Since the momentum constraint (7.2) is linear, a binary black hole solution can now be constructed by superposition of single solutions

$$\bar{A}^{ij} = \bar{A}_{\mathbf{C}_1\mathbf{P}_1}^{ij} + \bar{A}_{\mathbf{C}_2\mathbf{P}_2}^{ij} \quad (7.5)$$

The total linear momentum of this solution is $P^i = P_1^i + P_2^i$, and from (3.16) we find that the total angular momentum is given by

$$J_i = \epsilon_{ijk} C_1^j P_1^k + \epsilon_{ijk} C_2^j P_2^k. \quad (7.6)$$

The extrinsic curvature can then be inserted into the Hamiltonian constraint, which for conformal flatness and maximal slicing reduces to

$$\Delta^{\text{flat}} \psi = -\frac{1}{8} \psi^{-7} \bar{A}_{ij} \bar{A}^{ij}. \quad (7.7)$$

Here Δ^{flat} is the flat Laplace operator.

7.1.1 The Conformal-Imaging Approach

At this point, the topology of the solution to be constructed has to be decided on. In the conformal-imaging approach a two-sheeted topology is assumed, so that an isometry holds across the throats. For this isometry to hold, additional image terms have to be added to the extrinsic curvature (7.5) before it is inserted into the Hamiltonian constraint (7.7) (Kulkarni, Shepley and York, 1983).

Cook (1991) and Cook *et.al.* (1993) constructed solutions to the Hamiltonian constraint for two black holes with arbitrary momenta using the conformal-imaging approach. In these simulations, the isometry conditions on the throats were used as boundary conditions, so that the singularities inside the throats could be eliminated from the numerical grid. The computational disadvantage of this method is that boundary conditions have to be imposed on fairly

complicated surfaces. In finite difference algorithms, this can be accomplished either with bispherical or Čadež coordinates (Čadež, 1971, see also Appendix C of Cook (1991)), designed such that a constant coordinate surface coincides with the throat, or else with fairly complicated algorithms in Cartesian coordinates. Both approaches, together with a spectral method, have been compared in Cook *et.al.* (1993).

To construct equal-mass binary black holes in quasi-circular orbit, one may assume that $P^i \equiv P_1^i = -P_2^i$, and that $P_i C^i = 0$, where C^i is the separation vector $C^i \equiv C_1^i - C_2^i$. For a given mass of the binary, the only remaining free parameters are the separation $C \equiv \|C^i\|$, and the momentum $P \equiv \|P^i\|$. It is intuitively clear, however, that for each separation C there is only one momentum P that corresponds to a circular orbit – namely the one that satisfies the equivalent of Kepler’s third law.

General relativity does not admit strictly circular orbits, since the emission of gravitational radiation will lead to loss of energy and angular momentum, and hence to a shrinking of the orbit. During most of the inspiral phase (see Section 1), however, the separation decreases very slowly, on a timescale much larger than the orbital period. It is therefore very reasonable to approximate the orbit as *quasi-circular*.

To determine this quasi-circular orbit, Cook (1994) suggested locating turning points of the binding energy E_b along a sequence of constant black hole mass M_{BH} and constant angular momentum $J = CP$. Restricting ourselves to non-spinning black holes, the mass of each individual black hole might be identified with the irreducible mass¹⁴

$$M_{\text{BH}} = M_{\text{irr}} \approx \left(\frac{A}{16\pi} \right)^{1/2}, \quad (7.8)$$

where A is the proper area of the black hole’s event horizon (Christodoulou, 1970). In numerical simulations, A is approximated as the area of the apparent horizon (see Section 6.1). The binding energy can then be defined as

$$E_b = M - 2M_{\text{BH}}, \quad (7.9)$$

where M is the total ADM mass of the system, given by (3.14). Lastly, we can define l as the proper separation between the two horizons, measuring the shortest path from one surface to the other.

¹⁴The mass of a single black hole in the presence of neighboring black holes is not unambiguously defined in general relativity, in contrast to the total mass as measured at infinity.

Following Cook (1994), quasi-circular orbits correspond to turning points

$$\left. \frac{\partial E_b}{\partial l} \right|_{M_{\text{BH}}, J} = 0. \quad (7.10)$$

A minimum corresponds to a stable quasi-circular orbit, while a maximum corresponds to an unstable orbit. The transition from stable to unstable orbits defines the innermost stable circular orbit (ISCO), which occurs at the saddle point

$$\left. \frac{\partial^2 E_b}{\partial l^2} \right|_{M_{\text{BH}}, J} = 0. \quad (7.11)$$

For a quasi-circular orbit, the binary's orbital angular velocity Ω as measured at infinity can then be determined from¹⁵

$$\Omega = \left. \frac{\partial E_b}{\partial J} \right|_{M_{\text{BH}}, l} \quad (7.12)$$

(compare Friedman, Uryū and Shibata (2002); Baker (2002)). A motivation and illustration of this approach can be found in Baumgarte (2001).

At this point, a word of warning is in order. As we have discussed above, relativistic binaries emit gravitational radiation, causing them to slowly spiral toward each other, and they hence do not follow strictly circular orbits. The very concept of an innermost stable *circular* orbit is therefore somewhat ill defined. Also, the minimum in the equilibrium energy identifies the onset of a *secular* instability, while the onset of *dynamical* instability may be more relevant for the binary inspiral (see, e.g., the discussion in Lai, Rasio and Shapiro (1993) and Lombardi, Rasio and Shapiro (1997), where it is shown that the two instabilities coincide in irrotational binaries). Moreover, it has been suggested that the passage through the ISCO may proceed quite gradually (Ori and Thorne, 2000; Buananno and Damour, 2000), so that a precise definition of the ISCO may be less meaningful than the above turning method suggests (see also Duez *et.al.* (2002)). Ultimately, dynamical evolution calculations will have to simulate the approach to the ISCO and to investigate these issues. For the sake of dealing with a well-defined problem, we will here identify the ISCO with the saddlepoint of the equilibrium energy (7.11).

¹⁵ Keeping l fixed in this derivative is equivalent to taking the derivative along an evolutionary sequence (Cook, 1994; Pfeiffer, Teukolsky and Cook, 2000), since the difference only appears at second order. I am grateful to H. Pfeiffer for pointing this out.

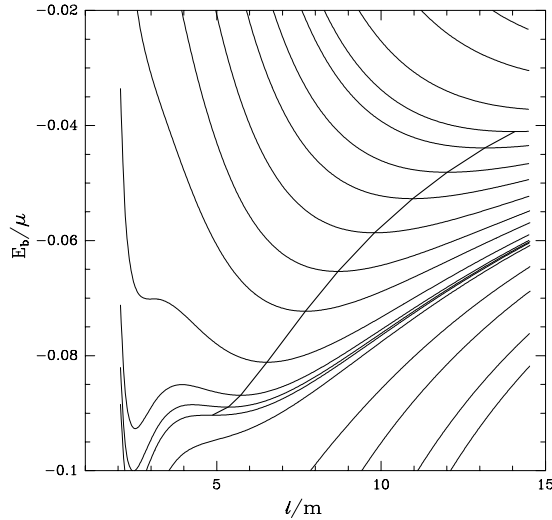


Fig. 7.1. The effective potential E_b/μ as a function of separation l for various values of the angular momentum $J/\mu m$ (thin lines) as obtained in the Bowen-York conformal-imaging approach. Here μ is the reduced mass $M_{\text{BH}}/2$ and m is the sum of the black hole masses $2M_{\text{BH}}$. The thick line connects a sequence of stable quasi-circular orbits, which correspond to minima of the binding energy (7.10). This sequence ends at the ISCO, identified by the saddlepoint of the binding energy (7.11). (Figure from Cook (1994).)

Combining the conformal-imaging approach with the turning-point method Cook (1994) constructed the first models of binary black holes in quasi-circular orbit (see Figure 7.1, which also illustrates the construction of circular orbits and the ISCO with the turning point method). Numerical values for the non-dimensional binding energy $\bar{E}_b \equiv E_b/\mu$, the orbital angular velocity $\bar{\Omega} \equiv m\Omega$ and angular momentum momentum $\bar{J} \equiv J/(\mu m)$ at the ISCO as obtained by Cook (1994) and other authors are listed in Table 7.1. Here μ is the reduced mass $\mu = M_{\text{BH}}/2$ and m is the sum of the black hole masses $m = 2M_{\text{BH}}$. The results of Cook (1994) were generalized to spinning black holes by Pfeiffer, Teukolsky and Cook (2000).

7.1.2 The Puncture Approach

An alternative to the conformal imaging approach is the *puncture* approach suggested by Brandt and Brügmann (1997), in which the singularities in the Hamiltonian constraint (7.7) are absorbed in an analytic expression. To do this, we write the conformal factor ψ as a sum

$$\psi = u + \frac{1}{a} \quad (7.13)$$

Reference	\bar{E}_b	\bar{J}	$\bar{\Omega}$
Schwarzschild	-0.0572	3.464	0.068
Cook (1994)	-0.09030	2.976	0.172
Baumgarte (2000)	-0.092	2.95	0.18
Grandclément, Gourgoulhon and Bonazzola (2002)	-0.068	3.36	0.103
Damour, Jaranowski and Schäfer (2000)	-0.0668	3.27	0.0883

Table 7.1

Values for the binding energy \bar{E}_b , the angular velocity $\bar{\Omega}$ and the angular momentum \bar{J} at the ISCO as obtained in different approaches.

with

$$\frac{1}{a} = \frac{\mathcal{M}_1}{2r_{\mathbf{C}_1}} + \frac{\mathcal{M}_2}{2r_{\mathbf{C}_2}}. \quad (7.14)$$

In the limit of infinite separation, the parameters \mathcal{M}_1 and \mathcal{M}_2 approach the masses of the individual black holes, but in general they are simply constants. Since $1/a$ is a solution to the (homogeneous) Laplace equation, the Hamiltonian constraint (7.7) now reduces to

$$\Delta^{\text{flat}} u = -b(1 + au)^{-7}, \quad (7.15)$$

where we have abbreviated

$$b = \frac{1}{8} a^7 \bar{A}_{ij} \bar{A}^{ij}. \quad (7.16)$$

The beauty of this approach is that the poles at the center of the black holes have been absorbed into the analytical terms, and that the corrections u are regular everywhere (Brandt and Brügmann, 1997). Equation (7.15) can therefore be solved everywhere, and there is no longer any need to excise the interior of the black holes from the computational grid. This eliminates the need for complicated boundary conditions on the throats, and allows for straightforward solutions on very simple computational domains. Since one no longer needs the isometry conditions on the throat, one can construct black hole binaries in a three-sheeted topology, so that no additional mirror terms need to be added to the extrinsic curvature (7.5), and instead (7.5) can be inserted directly into (7.16). The only added complication of this approach is that the location of the throat and horizon is not known a priori, and has to be located after the fact. This can be done with the apparent horizon finders discussed in Section 6.1.

Once a solution u has been found, the ADM energy (3.14) can be determined from

$$\begin{aligned} M &= -\frac{1}{2\pi} \oint_{\infty} \bar{D}^i \psi d^2 S_i = -\frac{1}{2\pi} \oint_{\infty} \bar{D}^i \left(\frac{1}{\alpha} \right) d^2 S_i - \frac{1}{2\pi} \int \Delta^{\text{flat}} u d^3 x \\ &= \mathcal{M}_1 + \mathcal{M}_2 + \frac{1}{2\pi} \int b(1 + \alpha u)^{-7} d^3 x. \end{aligned} \quad (7.17)$$

Baumgarte (2000) combined the puncture method of Brandt and Brügmann (1997) with the turning-point method of Cook (1994) to construct binary black holes in quasi-circular orbit. Numerical values for the ISCO are included in Table 7.1. Baker (2002) recently found very similar results by keeping a “bare” mass fixed instead of the apparent horizon mass.

7.2 The Thin-Sandwich Approach

As we will see in Section 7.3, the numerical results of Cook (1994) and Baumgarte (2000) disagree with post-Newtonian values for the ISCO by disturbingly large factors, which suggests that it would be useful to explore alternatives to the Bowen-York approach.

This has been done recently by Gourgoulhon, Grandclément and Bonazzola (2002) and Grandclément, Gourgoulhon and Bonazzola (2002), who have constructed binary black holes in the thin-sandwich approach (Section 3.3). In the thin-sandwich formalism, equations (3.27) – (3.29) are solved for the conformal factor ψ , the lapse α and the shift β^i . Unlike in the Bowen-York approach, the extrinsic curvature is not constructed from the analytical solution (7.5), but is instead computed from ψ , α and β^i (equation (3.22)). It is important to note that Gourgoulhon, Grandclément and Bonazzola (2002), just like Cook (1994) and Baumgarte (2000), assume maximal slicing and conformal flatness.

Following Cook (1991), Gourgoulhon, Grandclément and Bonazzola (2002) and Grandclément, Gourgoulhon and Bonazzola (2002) adopt the conformal-imaging approach (Section 7.1.1), which means that suitable boundary conditions have to be imposed on ψ , α and β^i on the throat. This leads to a technical problem. The isometry condition requires that both $\alpha = 0$ and $\beta^r = 0$ on the throat. For $\alpha = 0$ (and ψ non-zero) in equation (3.22), the extrinsic curvature can only be regular if the derivative of β^r also vanishes. The shift therefore has to satisfy more conditions than can be imposed. Grandclément, Gourgoulhon and Bonazzola (2002) circumvent this problem by introducing a regularization for the shift which then slightly violates equation (3.28), and proceed by hoping that this violation is small (see also the discussion in Cook (2002), who

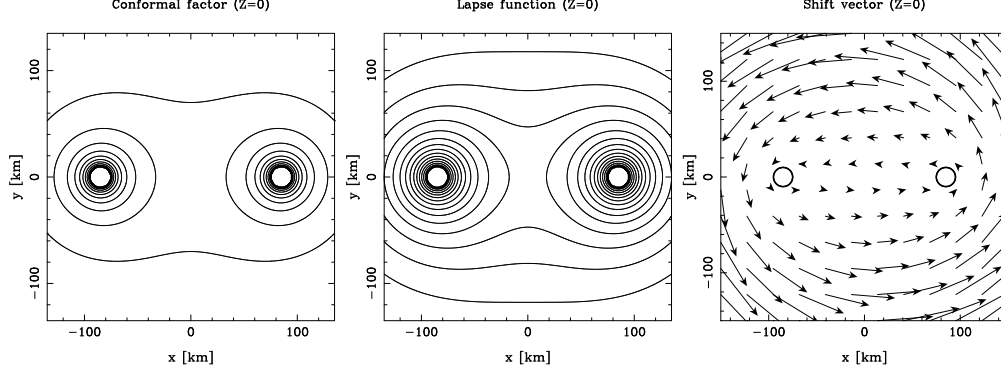


Fig. 7.2. Isocontours of the lapse function α , the conformal factor ψ and the shift vector β^i in the orbital plane $z = 0$ at the ISCO as obtained with the thin-sandwich approach. The thick solid lines denote the surfaces of the throats. The kilometer scale of the axis corresponds to an ADM mass of $31.8 M_\odot$. (Figure from Grandclément, Gourgoulhon and Bonazzola (2002).)

introduces an alternative set of boundary conditions).

The approach of Grandclément, Gourgoulhon and Bonazzola (2002) differs in another way from the calculations of Cook (1994) and Baumgarte (2000), namely in the determination of circular orbits. Instead of adopting the turning-point method, they compute the Komar mass (Komar, 1959)

$$M_K = \frac{1}{4\pi} \oint_{\infty} \gamma^{ij} (D_i \alpha - \beta^k K_{ik}) d^2 S_j \quad (7.18)$$

in addition to the ADM mass M (3.14). In general, the two mass definitions lead to different masses, but they agree in stationary spacetimes (Beig, 1978). Since quasi-equilibrium solutions approximate stationary spacetimes, Grandclément, Gourgoulhon and Bonazzola (2002) suggest that quasi-circular orbits can be identified by demanding

$$M = M_K. \quad (7.19)$$

The angular velocity Ω enters the equations (3.27) – (3.29) only through the outer boundary condition on the shift (Grandclément, Gourgoulhon and Bonazzola, 2002, equation (9)). This value can be varied until $M = M_K$ has been achieved. Note that this condition cannot be applied in the Bowen-York approach, since it does not provide the lapse and shift that is needed to evaluate the Komar mass (7.18).

Instead of using equation (7.12) to determine Ω , as in the turning-point method, it can now be used to construct an evolutionary sequence. The ISCO can be identified by locating a simultaneous minimum in the ADM mass M and the angular momentum J . Numerical values are included in Table 7.1.

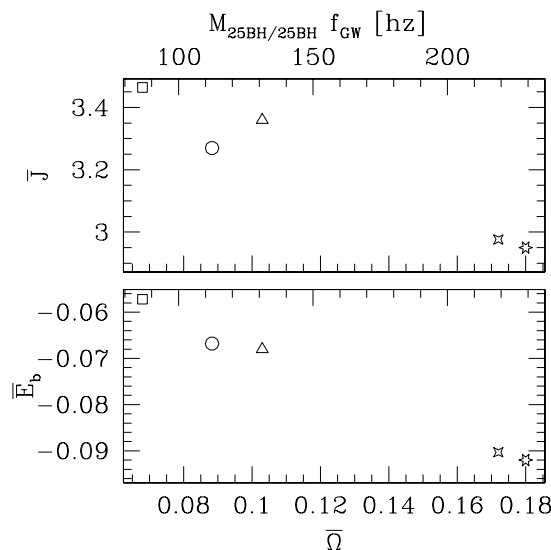


Fig. 7.3. Results for the angular momentum \bar{J} , the binding energy \bar{E}_b , and the orbital angular velocity $\bar{\Omega}$ at the ISCO for different approaches (see also Table 7.1). The square marks the Schwarzschild test-mass result, the circle the third order post-Newtonian results of Damour, Jaranowski and Schäfer (2000), the triangle the numerical results of Grandclément, Gourgoulhon and Bonazzola (2002), and the four and six-pointed stars the results of Cook (1994) and Baumgarte (2000). The top label gives the corresponding gravitational wave frequencies for a binary of two $25 M_\odot$ black holes. Compare Figures 2 in Baumgarte (2001) and 20 in Grandclément, Gourgoulhon and Bonazzola (2002).

7.3 Comparison and Discussion

In Table 7.1 we list numerical results from the numerical calculations of Cook (1994), Baumgarte (2000) and Grandclément, Gourgoulhon and Bonazzola (2002). We also include the third order post-Newtonian results of Damour, Jaranowski and Schäfer (2000, assuming $\omega_{\text{static}} = 0$), as well as the analytical values for a test particle orbiting a Schwarzschild black hole, $\bar{E}_b = \sqrt{8/9} - 1 \sim -0.0572$, $\bar{J} = 2\sqrt{3} \sim 3.464$, and $\bar{\Omega} = 1/6^{3/2} \sim 0.0680$. The same numbers are also plotted in Figure 7.3.

It is very noticable that the results of Grandclément, Gourgoulhon and Bonazzola (2002) agree quite well with Damour, Jaranowski and Schäfer (2000) (see also Blanchet (2002); Damour, Gourgoulhon and Grandclément (2002)), and that Cook (1994) agrees very well with Baumgarte (2000). There is a disturbingly large discrepancy between these two groups, however, of as much as a factor of two in the orbital frequency. It is most likely that these differences are caused by the different choices in the initial value decomposition. In fact, Pfeiffer, Cook and Teukolsky (2002) recently demonstrated that “different decompositions generate different physical initial-data sets for seemingly similar

choices for the freely specifiable pieces”, and that “the choice of the extrinsic curvature is critical”. The different decompositions seem to lead to different transverse-traceless components of the extrinsic curvature, so that the resulting data represent physically different slices (see also Damour, Gourgoulhon and Grandclément (2002)).

This conclusion leads to the question which initial value decomposition leads to more realistic initial data, describing binary black holes in quasi-circular orbit. As of now we do not have any reliable means of knowing. One way to compare the different initial data would be to evolve them dynamically and test which one is closer to being in equilibrium. While dynamical evolution codes that are reliable enough to make such comparisons are only now being developed (see Section 8), preliminary results suggest that evolutions of the initial data of Baumgarte (2000) do not lead to circular orbits (Alcubierre and Seidel, 2002). The fact that the two very different approaches of Grandclément, Gourgoulhon and Bonazzola (2002) and Damour, Jaranowski and Schäfer (2000) lead to quite similar results also points to these initial data being more realistic¹⁶. This is in accord with our arguments in Section 3.3 that the thin-sandwich decomposition provides a more natural means of constructing equilibrium initial data (see also Lousto and Price (1998)). Together, these findings suggest that the currently most promising approach to numerically constructing binary black holes in quasi-circular orbit is the thin-sandwich formulation.

The good agreement between Cook (1994) and Baumgarte (2000) may not be surprising, since the two approaches differ, other than in their numerical approach, mostly in the underlying manifold structure (the conformal-imaging approach of Cook (1994) adopts a two-sheeted topology, while the puncture method used by Baumgarte (2000) leads to a three-sheeted topology). The small difference in their results reflects the fact that the strength of the imaged mirror poles in the conformal-imaging approach is much smaller than the strength of the poles themselves (Misner, 1963).

Several future developments would be very desirable. As discussed above, the approach taken by Grandclément, Gourgoulhon and Bonazzola (2002) seems very promising. The inconsistency introduced by the regularization of the shift, which may spuriously affect their results, could be eliminated either by adopting the boundary conditions of Cook (2002), or by combining the thin-sandwich approach with the puncture method and hence completely eliminating the need for inner boundary conditions.

It would also be desirable to construct binary black holes using yet other

¹⁶ Even though both Grandclément, Gourgoulhon and Bonazzola (2002) and Damour, Jaranowski and Schäfer (2000) make some adhoc assumptions, so that their agreement could possibly be purely coincidental.

approaches. Marronetti and Matzner (2000, cf. Pfeiffer, Cook and Teukolsky (2002)) suggested a construction based on black holes in Kerr-Schild coordinates (see Section 8.1), which would avoid the assumption of conformal flatness. This approach has the additional benefit that the slices are regular across the horizon, which is very desirable for dynamical simulations. Results for quasi-circular orbits, however, are not yet available. Another possible approach that avoids the assumption of conformal flatness is to adopt a post-Newtonian solution as a background solution, and to solve the Hamiltonian and momentum constraints for corrections to the post-Newtonian metric (Tichy *et.al.*, 2002).

8 Dynamical Simulations of Binary Black Holes

The dawn of numerical relativity dates back to the calculation in axisymmetry of the head-on collision from rest at large separation of two identical black holes by Larry Smarr and his collaborators (see, e.g., Smarr (1979); Anninos *et.al.* (1993)). The result was that the emitted radiation is roughly 0.1 % Mc^2 , significantly less than the upper limit of 29 % allowed by Hawking's area theorem, but in accord with expectations from strong-field perturbation theory.

While significant progress has been made recently in the dynamical evolution of binary black hole scenarios in full 3D, even simulations of single black holes are still facing stability problems that are only poorly understood. A likely candidate for the origin of these problems is the handling of the black hole singularities, which we will discuss in Section 8.1. In spite of these difficulties, several groups have performed preliminary simulations of binary black hole mergers. We will review these efforts in Section 8.2.

8.1 Singularity Avoidance and Black Hole Excision

Simulations of black holes are greatly complicated by the presence of singularities. Encountering such a singularity during a computation would clearly have very unfortunate consequences for the numerical simulation. Two approaches have therefore been suggested to avoid these singularities: using *singularity avoiding* coordinates, and *excising* the black hole interior.

Traditionally, many black hole simulations, in particular in spherical and axial symmetry, have used *singularity avoiding* coordinates to model black hole spacetimes. This approach is illustrated in Figure 8.1, in which a family of singularity avoiding time slices wrap up around the newly formed singularity

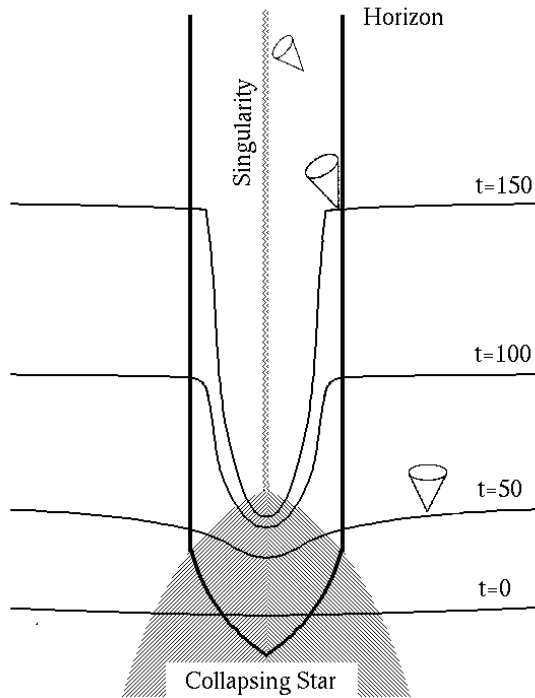


Fig. 8.1. A black hole spacetime diagram showing various singularity avoiding time slices that wrap up around the singularity inside the horizon. Such slicings allow short term success in the numerical evolution of black holes, while at the same time causing pathological behavior due to “grid stretching” that eventually dooms the calculation at late times. (Figure from Anninos *et.al.* (1995b).)

inside the horizon. Among the slicing conditions that avoid singularities is maximal slicing, which we discussed in Section 5.2. Another singularity avoiding slicing condition that proved quite useful in spherical and axisymmetric simulations is *polar slicing* (Eardley, 1982; Bardeen and Piran, 1983; Shapiro and Teukolsky, 1986; Schinder, Bludman and Piran, 1988). The properties of maximal and polar slicing have been analyzed for Oppenheimer-Snyder collapse in Petrich, Shapiro and Teukolsky (1985, 1986). In three-dimensional simulations, the “1+log” slicing (see Section 5.3) has been used fairly commonly. It has been shown to have singularity avoiding properties not unlike maximal slicing (Bona, Massó, Seidel and Stela, 1995; Anninos *et.al.*, 1995c), and as an algebraic condition it is much easier to implement.

The problem with singularity avoidance is that the time slices become increasingly pathological, as illustrated in Figure 8.1. For late times, they have to “stretch” all the way back to an early time in order to avoid the singularity. This “grid stretching” will lead to very steep gradients, which will lead to large numerical error, and which will ultimately cause the code to crash. One could try to resolve these steep gradients with an increasingly large number of gridpoints. This attempt leads to a “grid sucking” effect, and is similarly undesirable. Instead of solving the problem it only postpones the code crash

to a slightly later time, and moreover leads to large amounts of computational resources being spent on uninteresting regions of the spacetime.

If, unlike in Figure 8.1, the initial time slice already contains a singularity, it may be possible to absorb the singular part of the solution into an analytical expression, similar to the puncture method of Brandt and Brügmann (1997) (see Section 7.1.2). For a single black hole, for example, one can factor out the time-independent conformal factor (3.18), and evolve only the conformally related metric, which is regular everywhere. Functions and their derivatives can then be evaluated from the numerical functions together with the analytical factors, as long as the singularity of (3.18) does not happen to lie on a grid point.

In the first dynamical simulation of a black hole in three spatial dimensions, Anninos *et.al.* (1995c) adopted the traditional ADM formulation (Section 2) together with geodesic, “1+log” and maximal slicing (Sections 5.1, 5.2 and 5.3). The simulations in geodesic slicing encounter the central singularity very early on. In maximal and “1+log” slicing grid-stretching effects produce very large gradients very rapidly, as expected from simulations in spherical or axial symmetry, and the code crashes after a fairly short time (up to about $50M$ in some cases). Anninos *et.al.* (1995c) experimented with different ways of treating the singularities at the center of the black hole, including imposing isometry conditions (see Section 7.1.1) on the black hole throats and the analytical factoring described above (see also Brügmann (1996)).

Unruh (1984) pointed out that there is no need to include the interior of the black hole in the numerical simulation, because by the very definition of an event horizon (Section 6.2) the exterior is causally disconnected from the interior. If no information can propagate from the interior to the exterior, there is no need to numerically simulate the interior¹⁷. From Figure 8.1 it is evident that *black hole excision* may avoid both the singularity at the center of the black hole as well as the grid stretching effects associated with singularity avoiding timeslices.

Black hole excision is currently considered the most promising approach to dynamical black hole simulations. It has been successfully implemented in spherical symmetry (e.g. Seidel and Suen (1992); Scheel, Shapiro and Teukolsky (1995a,b) and Lehner *et.al.* (2000)), but most implementations in three spatial dimensions are still plagued by instabilities.

Various design choices have to be made in the implementation of black hole excision. As discussed in Section 6, the location of the event horizon is unknown during the dynamical simulation, so the excision is instead based on

¹⁷ Unless, of course, one is interested in the structure of the singularity; see, e.g., Berger and Moncrief (1993); Hübner (1996); Garfinkle (2002).

the location of the apparent horizon. Typically not all gridpoints inside the apparent horizon are excised, and instead a buffer zone of a few gridpoints is left inside the black hole. At each timestep, the grid points on the *inner boundary* have to be filled with numerical data. If a hyperbolic formulation of Einstein's equation is used with characteristics that lie either on or inside the light cone (e.g. the Einstein-Christoffel system discussed in Section 3.2), then all these characteristics must be outgoing on this inner boundary (i.e. toward the singularity), as is evident from the tilting of the light cones in Figure 8.1. In this case, the evolution equations can be used to fill the inner boundary points ("boundary without a boundary condition").

The tilting of the light cones points to another computational problem. While a normal observer n^a always lies inside the light cone, a coordinate observer t^a may lie outside the line cone, resulting in "super-luminal" grid velocities. This happens when the shift vector β^i becomes large (see equation 2.31). As a consequence, a gridpoint x_{ijk}^{n+1} on a timeslice t^{n+1} may be causally disconnected from the same gridpoint x_{ijk}^n on the previous timeslice t^n (see Figure 1 in Scheel *et.al.* (1997) for an illustration). Some numerical schemes become unconditionally unstable in such a situation, while others are stable only for very small time steps Δt . To avoid this problem, several groups have used *causal differencing* (Seidel and Suen, 1992; Alcubierre and Schutz, 1994; Scheel *et.al.*, 1997; Cook *et.al.*, 1998; Gundlach and Walker, 1999; Lehner, Huq and Garrison, 2000). Briefly summarized, the idea behind causal differencing is to evolve the gravitational fields along n^a instead of t^a , and then use an interpolation to shift the fields along the shift β^i .

If spatial derivatives have to be evaluated in the updating scheme, then derivatives in directions orthogonal to the surface of the excised region have to be computed using extrapolation or one-sided schemes on the inner boundary. In general, the coordinates will not be aligned with this surface, so that an appropriate algorithm has to be constructed.

If a black hole moves through the computational grid, then grid points re-emerge from the excised region on the trailing side of the black hole. These grid points have to be filled with data points, presumably by extrapolation.

Cook *et.al.* (1998) implemented black hole excision together with causal differencing for both static and boosted black holes, using the ADM formalism. As initial data, they adopted Schwarzschild black holes in *Kerr-Schild* form (compare Chandrasekhar (1992); Marsa and Choptuik (1996); Matzner, Huq and Shoemaker (1999); Marronetti and Matzner (2000); Yo, Baumgarte and Shapiro (2001b)).

In ingoing Kerr-Schild form, the Kerr metric is given by

$$ds^2 = g_{ab}dx^a dx^b = (\eta_{ab} + 2Hl_a l_b)dx^a dx^b, \quad (8.1)$$

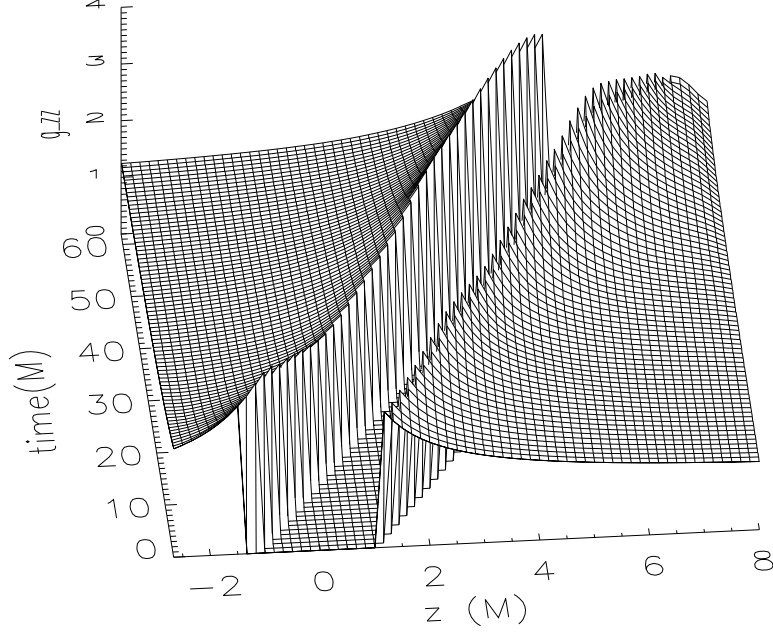


Fig. 8.2. Metric component g_{zz} along the z -axis as a function of time. The flat region that moves diagonally to the right represents the excised region (inside the black hole). Note that points at the trailing edge (left side) are smoothly updated as the hole moves toward positive z . Coordinate effects are seen to appear near the inner boundary. (Figure from Cook *et.al.* (1998).)

where $H = H(x^a)$ is a scalar function. The vector l_a is null both with respect to η_{ab} and g_{ab} ,

$$\eta^{ab}l_al_b = g^{ab}l_al_b = 0. \quad (8.2)$$

Comparing with the ADM metric (2.41), we can identify

$$\alpha = (1 + 2Hl_t^2)^{-1/2} \quad (8.3)$$

$$\beta_i = 2Hl_t l_i \quad (8.4)$$

$$\gamma_{ij} = \eta_{ij} + 2Hl_i l_j. \quad (8.5)$$

For the time-independent Schwarzschild spacetime we have

$$H = M/r \quad (8.6)$$

$$l_a = (1, x_i/r), \quad (8.7)$$

where M is the total mass-energy and $r^2 = x_1^2 + x_2^2 + x_3^2$. This form is equivalent to the ingoing Eddington-Finkelstein form (compare Misner, Thorne and Wheeler (1973)). The Kerr-Schild form (8.1) is invariant under boosts, and therefore can be used to represent either a static or boosted Schwarzschild (or Kerr) black hole. The other great advantage of Kerr-Schild coordinates

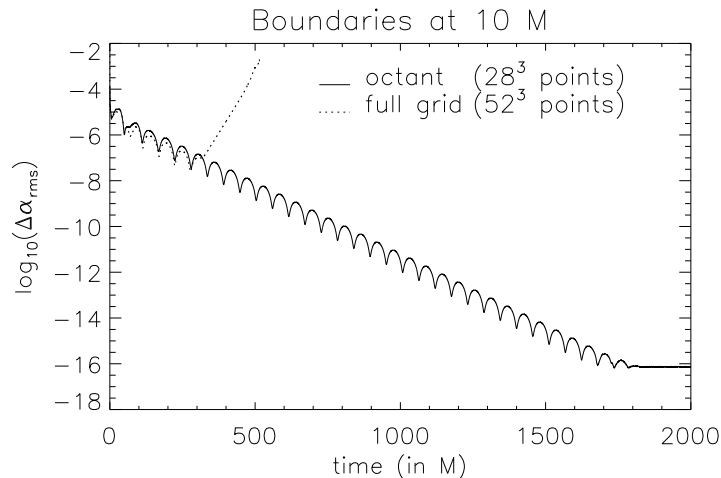


Fig. 8.3. The root means square of the change of the lapse function α from one time step to the next, in the simulations of Alcubierre and Brügmann (2001) for “1+log” slicing and static shift. Shown are the results for two runs, one performed in octant symmetry, and an identical run except that it does not assume any symmetry. The former evolves stably until very late times, while the latter develops an instability after a few 100M. (Figure from Alcubierre and Brügmann (2001).)

is that they are regular on the horizon and hence extend smoothly into the black hole. In Schwarzschild coordinates, for example, the lapse vanishes on the horizon. As a consequence, infalling radiation will never cross the horizon in Schwarzschild coordinates, and will instead “pile up” just outside the horizon. This has unfortunate consequences for numerical simulations, because this piling up will produce increasingly small length-scales which cannot be resolved with any given finite-difference resolution (see Rezzolla *et.al.* (1998) for an illustration in three spatial dimensions).

Cook *et.al.* (1998) use analytic Kerr-Schild data as initial data, and adopt the Kerr-Schild lapse and shift to fix the coordinates. For static black holes, evolutions of up to 95M are achieved, a slight improvement over the results of Anninos *et.al.* (1995c) (compare also with the run-time of 138M achieved by Daues (1996)¹⁸). More importantly, Cook *et.al.* (1998) demonstrate that black holes can be advected through a numerical grid. Figure 8.2 shows the excised region inside the black hole moving through the grid, and also demonstrates that points at the trailing edge, which re-emerge from the black hole, are updated smoothly.

¹⁸ Note also that *characteristic* evolutions of black holes in three spatial dimension had already achieved runtimes of about 1400M (Gomez *et.al.*, 1998). However, modeling binary black holes with characteristic methods requires multiple matching between characteristic and presumably Cauchy methods, which has not been established yet.

A new and quite successful approach was suggested by Alcubierre and Brügmann (2001, see also Alcubierre *et.al.* (2001b)). They use the BSSN formalism (Section 3.3) instead of the ADM formalism, and a particular simple black hole excision scheme. Instead of excising a (nearly) spherical region, they excise a cube, which is well adapted to the Cartesian coordinates. Instead of trying to construct boundary conditions from the evolution equations, they use a simple but stable boundary condition on the inner boundary. Finally, instead of using causal differencing, they use centered differences except for advection terms on the shift (i.e. terms involving $\beta^i \partial_i$), which are differenced with an upwind scheme along the shift direction. A modification of this scheme was suggested by Yo, Baumgarte and Shapiro (2001b).

Alcubierre and Brügmann (2001) use a static black hole in Kerr-Schild coordinates as initial data, and experiment with several slicing and gauge conditions, including using the analytical lapse and shift of the Kerr-Schild solution, maximal slicing, “1+log” slicing, and “Gamma-freezing” (see Section 5.4). An example of their results is shown in Figure 8.3, where the root mean square of the change of the lapse from one time step to the next is plotted as a function of time for “1+log” slicing and static (analytic) shift. Two findings are quite remarkable. When evolved in octant symmetry the evolution settles down exponentially until the changes in the lapse reach machine precision. No instability is encountered. However, when octant symmetry is relaxed, an otherwise identical evolution develops an instability after a few hundred M ¹⁹. Similar results were reported by Scheel (2000), who use a completely independent implementation (namely spectral methods) of a different formulation of Einstein’s equations (namely the Einstein-Christoffel system described in Section 3.2). Improvements over these results have been reported by Laguna and Shoemaker (2002); Lindblom and Scheel (2002); Yo, Baumgarte and Shapiro (2002); Alcubierre *et.al.* (2002). In the BSSN calculation of Yo, Baumgarte and Shapiro (2002), the octant symmetry has been removed and long-term stability has been achieved both for static and rotating black holes.

8.2 Evolution of Binary Black Holes

Disregarding the stability problems in simulations of single black holes, some groups (Brügmann, 1999; Brandt *et.al.*, 2000; Alcubierre *et.al.*, 2001a; Baker *et.al.*, 2001, 2002) have initiated preliminary simulations of binary black holes.

Brügmann (1999), Brandt *et.al.* (2000) and Alcubierre *et.al.* (2001a) simulated “grazing” collisions of black holes. In these simulations, two black holes, start-

¹⁹ It is also interesting that when evolved with the ADM formalism instead of the BSSN formalism, the simulation terminates after about 30 M , even in octant symmetry

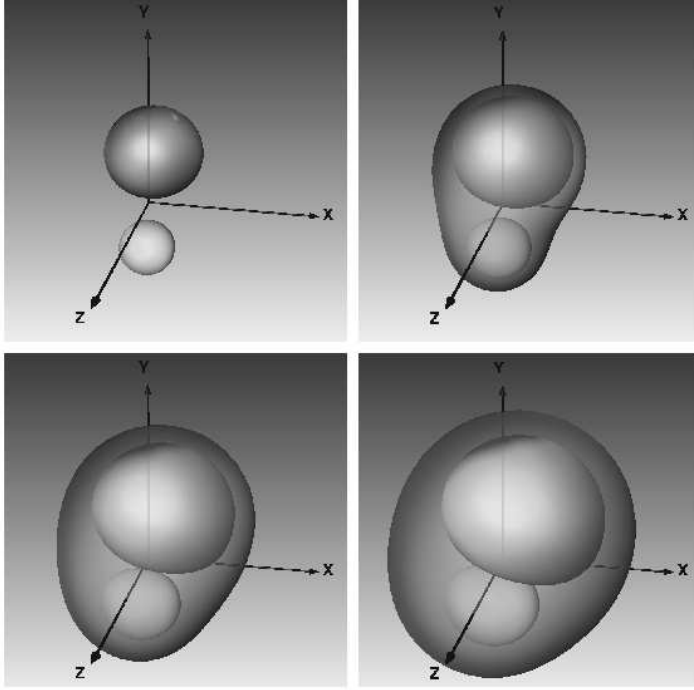


Fig. 8.4. The merger of apparent horizons in the simulations of Alcubierre *et.al.* (2001a). Shown are marginally trapped surfaces at times $2.5M$, $3.7M$, $5.0M$, and $6.2M$. The apparent horizon is the outermost of these surfaces. (Figure from Alcubierre *et.al.* (2001a).)

ing out well within the ISCO, are boosted toward each other with a certain impact parameter. These initial data do not correspond to the ISCO or any other astrophysically motivated configuration, and are instead chosen so that a common apparent horizon forms soon after the start of the evolution.

Brügmann (1999) uses the puncture method of Brandt and Brügmann (1997) both for the construction of initial data (as described in Section 7.1.2) and to remove the singularities during the evolution. In analogy to factoring out the time-independent term (3.18) for single black holes, Brügmann (1999) factors out a time-independent term similar to (7.13) for the binary. The remaining terms are regular, and can be integrated everywhere without black hole excision. In this approach the singularities or “punctures”, corresponding to the asymptotically flat region inside the black holes, remain at constant coordinate locations during the evolution. Brügmann (1999) evolves the remaining

regular terms using the ADM formalism with maximal slicing and zero shift. The simulation terminates very early (at about $t = 7M$), and the results are too crude to be of any astrophysical interest. They nevertheless show some interesting features, including the formation of a joint apparent horizon, and are also noteworthy as the first attempt to simulate binary black hole coalescence in three spatial dimensions.

Brandt *et.al.* (2000) adopt as initial data a superposition of Kerr-Schild solutions, which serves as an approximate solution to the constraint equations (Marronetti *et.al.*, 2000). This approximate solution also provides a lapse and shift which is used to fix the coordinates during the evolution. The gravitational fields are evolved with the ADM formalism, and the interior of the black holes is excised. The results seem to be strongly affected by the outer boundaries, which is implemented as a so-called “blending” to the semi-analytic solution. The code again crashes too early (after about $t = 15M$ on the “large” computational domain) to provide any interesting astrophysical results.

Alcubierre *et.al.* (2001a) return to the approach of Brügmann (1999), but use the BSSN formalism instead of the ADM formalism and the “1+log” slicing instead of maximal slicing during the evolution. The initial data and the “analytical” handling of the black hole singularities are very similar to Brügmann (1999). Alcubierre *et.al.* (2001a) take advantage of large computational resources at the National Center for Supercomputer Applications (NCSA), allowing them to simultaneously use fairly fine resolution and far outer boundaries on a uniform Cartesian grid. With this “combination of resolution, outer boundary location and treatment, coordinate choice, evolution system and puncture method for the black holes”, Alcubierre *et.al.* (2001a) were able to achieve evolutions well past $t = 30M$ (see Figure 8.4 for a visualization of the merger of apparent horizons). This is a significant improvement over previous results, since this number forms a rough minimum for a meaningful gravitational wave analysis. The lowest quasi-normal mode for a Schwarzschild black hole has a period of about $17M$, which sets the approximate scale for the expected gravitational wavelengths in the ringdown phase. A simulation past $t = 30M$ therefore allows one to capture about two periods of this ringdown phase, which Alcubierre *et.al.* (2001a) have been able to identify. At later times, however, grid-stretching effects as well as error originating from the outer boundaries start to degrade the numerical results. Alcubierre *et.al.* (2002) have recently reported finding singularity avoiding lapse and shift conditions which permit long-term stable integrations in octant symmetry.

Progress in the evolution of single and binary black holes has been very rapid in the past years (further improvements have already been reported by Alcubierre and Seidel (2002)), and it is quite likely that this field will continue to develop quite quickly in the near future.

As an alternative to a fully self-consistent numerical simulation of the entire plunge and merger of binary black holes, Baker *et.al.* (2001, 2002) recently demonstrated that it may be possible to match to a perturbative “close limit” treatment fairly early (the “Lazarus” project; see also Price and Pullin (1994)). Baker *et.al.* (2002) adopt puncture initial data describing binary black hole at the ISCO (see Baumgarte (2000) and Section 7.1.2), and evolve these with the ADM formalism, maximal slicing and zero shift (similar to Brügmann (1999)). The simulation terminates after about $t = 15 - 20M$. As an important self-consistency test, Baker *et.al.* (2002) show that the emitted gravitational wave signal and energy is independent, within a certain regime, of the time at which the matching is performed. It is likely that this or a similar approach will ultimately produce the desired late-time plunge and merger gravitational waveforms.

9 Binary Neutron Star Initial Data

In this Section we will discuss initial data describing binary neutron stars in quasi-equilibrium, quasi-circular orbit. Like the binary black hole solutions of Section 7 these models may serve as initial data in dynamical evolution equations (see Section 10), for the construction of evolutionary sequences up to the ISCO, and as background data for quasi-adiabatic approximations, as discussed in Section 10.4. We first discuss hydrostatic quasi-equilibrium in general (Section 9.1), and then specialize to corotational (Section 9.2) and irrotational binaries (Section 9.3).

9.1 Hydrostatic Quasi-Equilibrium

As we have discussed in Section 3.3, it is natural to adopt the thin-sandwich formalism for the construction of quasi-equilibrium initial data, since it allows us to set explicitly the time derivative of the conformally related metric to zero. With very few exceptions (Usui, Uryū and Eriguchi, 1999; Usui and Eriguchi, 2002), most binary neutron star initial data have also been constructed under the assumption of spatial conformal flatness. This has the great advantage of dramatically simplifying the equations, and has been justified naively by arguing that it approximately minimizes the gravitational wave content in the spatial slice (see also the discussion in Appendix C). Under these assumptions, the metric is written in the conformally flat form

$$ds^2 = -\alpha^2 dt^2 + \psi^4 \eta_{ij} (dx^i + \beta^i dt)(dx^j + \beta^j dt), \quad (9.1)$$

and Einstein's equations reduce to (3.27) through (3.29) for the lapse α , the conformal factor ψ and the shift β^i ²⁰.

To determine the matter sources in (3.27) to (3.29) we now have to specify the energy-momentum tensor T^{ab} , which, adopting a perfect fluid, can be written as

$$T^{ab} = (\rho_0 + \rho_i + P)u^a u^b + P g^{ab}. \quad (9.2)$$

Here u^a is the four-velocity of the fluid, and ρ_0 , ρ_i and P are the rest-mass density, internal energy density and pressure as observed by a comoving observer u^a . It is also useful to introduce the specific enthalpy

$$h = \exp \left(\int \frac{dP}{\rho_0 + \rho_i + P} \right). \quad (9.3)$$

For a polytropic equation of state

$$P = \kappa \rho_0^{1+1/n}, \quad (9.4)$$

where κ is the polytropic constant and n the polytropic index²¹, the enthalpy becomes

$$h = \frac{\rho_0 + \rho_i + P}{\rho_0}. \quad (9.5)$$

Note that equations (9.3) and (9.5) imply

$$dh = \rho_0^{-1} dP. \quad (9.6)$$

The equations of motion

$$\nabla_b T^{ab} = 0 \quad (9.7)$$

yield the Euler equation, which can be written as

$$u^b \nabla_b (h u_a) + \nabla_a h = 0. \quad (9.8)$$

²⁰ This formalism was developed independently by Wilson and Mathews (1989, 1995) as an approximate approach for dynamical simulations of binary neutron stars. We will discuss this approach in Section 10.2.

²¹ It is also common to use the polytropic exponent $\Gamma = 1 + 1/n$.

Rest-mass conservation yields the continuity equation,

$$\nabla_a(\rho_0 u^a) = 0. \quad (9.9)$$

Following Shibata (1998), we now write the fluid four-velocity u^a as

$$u^a = u^t(l^a + V^a), \quad (9.10)$$

where l^a is timelike and normalized so that $l^t = 1$, and V^a purely spatial, $n_a V^a = 0$. We will later assume that l^a is an approximate Killing vector. The spatial components of the velocity vector in a coordinate system comoving with l^a , which we will refer to as a corotating coordinate system, then reduce to $u^t V^i$.

The four-dimensional equations (9.8) and (9.9) can now be projected into the slice Σ . Expressing the covariant derivative $l^b \nabla_b u_a$ in terms of a Lie derivative along l^a and using equation (2.24) yields

$$\gamma_i^a \mathcal{L}_1(hu_a) + D_i \left(\frac{h}{u^t} + \hat{u}_j V^j \right) + V^j (D_j \hat{u}_i - D_i \hat{u}_j) = 0 \quad (9.11)$$

for the projection of (9.8) and

$$\alpha \left(\mathcal{L}_1(\rho_0 u^t) + \rho_0 u^t \nabla_a l^a \right) + D_i (\alpha \rho_0 u^t V^i) = 0 \quad (9.12)$$

for (9.9) (see Shibata (1998) and compare footnote 3 in Gourgoulhon (1998)). Here we have introduced \hat{u}_i as the spatial projection of hu_i ,

$$\hat{u}_i = \gamma_i^a hu_a. \quad (9.13)$$

So far we have not made any assumptions about the symmetry of the space-time. Now, however, we assume that l^a is a Killing vector, $\nabla_a l_b + \nabla_b l_a = 0$, in which case the quantities $\mathcal{L}_1(hu_a)$, $\mathcal{L}_1(\rho_0 u^t)$ and $\nabla_a l^a$ all vanish in the above equations. The Euler equation (9.11) then reduces to the Bernoulli equation

$$D_i \left(\frac{h}{u^t} + \hat{u}_j V^j \right) + V^j (D_j \hat{u}_i - D_i \hat{u}_j) = 0, \quad (9.14)$$

and the continuity equation (9.9) becomes

$$D_i (\alpha \rho_0 u^t V^i) = 0. \quad (9.15)$$

Example 9.1 We can now generalize the spherically symmetric, static solutions of Examples 3.3 and 5.2 to include matter. For a static star we have $u^a = n^a$ so that $u^t = \alpha^{-1}$. From equation (2.26) we find $\rho = \rho_0 + \rho_i$ and from (2.35) $S_{ij} = P\gamma_{ij}$ and hence $S = 3P$. The Hamiltonian constraint (3.12) becomes

$$\bar{D}^2\psi = -2\pi\psi^5\rho, \quad (9.16)$$

which, in spherical symmetry, can be integrated once to yield

$$\frac{\partial\psi}{\partial r} = -\frac{2\pi}{r^2} \int \psi^5 \rho r'^2 dr' = -\frac{m(r)}{2r^2} \quad (9.17)$$

where $m(r) \equiv 4\pi \int_0^r \psi^5 \rho r'^2 dr'$. In the exterior of the matter source, $m(r)$ is independent of r and (9.17) can be integrated once more to yield (3.18). The maximal slicing condition (3.26) can be similarly integrated to yield

$$\frac{\partial(\alpha\psi)}{\partial r} = \frac{2\pi}{r^2} \int \alpha\psi^5(\rho + 6P)r'^2 dr' = \frac{\alpha\tilde{m}(r)}{2r^2} \quad (9.18)$$

with $\tilde{m}(r) \equiv 4\pi\alpha^{-1} \int_0^r \alpha\psi^5(\rho + 6P)r'^2 dr'$. For static solutions we have $V^i = 0$, so that the continuity equation (9.15) is satisfied identically and the Bernoulli equation (9.14) reduces to

$$D_i(\alpha h) = 0. \quad (9.19)$$

This equation can now be rewritten as

$$\alpha D_i h = -h D_i \alpha = -h D_i \frac{\alpha\psi}{\psi} = -\frac{h}{\psi} (D_i(\alpha\psi) - \alpha D_i \psi) \quad (9.20)$$

or, with (9.6), (9.17) and (9.18),

$$\frac{\partial P}{\partial r} = -\frac{\rho_0 h}{\psi} \frac{m + \tilde{m}}{2r^2}. \quad (9.21)$$

This is the equivalent of the Oppenheimer-Volkoff equation (Oppenheimer and Volkoff, 1939) in isotropic coordinates. In the Newtonian limit this equation reduces to the Newtonian equation of hydrostatic equilibrium. We point out, however, that solving the equations of hydrostatic equilibrium for spherical stars is far more straight-forward in Schwarzschild areal coordinates than in isotropic coordinates presented here (e.g. Misner, Thorne and Wheeler (1973)).

For the construction of binaries in quasi-circular²² orbit we assume that the binary has a constant orbital velocity Ω . The time vector l^a in a frame corotating with the binary is therefore a Killing vector and can be constructed from the time vector in the binary's rest frame t^a as

$$l^a = t^a + \Omega \xi^a = \alpha n^a + \beta^a + \Omega \xi^a. \quad (9.22)$$

Here we have used (2.31) and have introduced ξ^a as the generator of rotations about the rotation axis. In Cartesian coordinates, $\xi^a = (0, -y, x, 0)$ represents a rotation around the z -axis. The Killing vector l^a is sometimes called the *helical* Killing vector (Bonazzola, Gourgoulhon and Marck, 1997).

The Bernoulli equation (9.14) and continuity equation (9.15) simplify for the two cases $V^a = 0$ and $D_j \hat{u}_i - D_i \hat{u}_j = 0$. The former corresponds to corotating binaries, and the latter to the more realistic case of irrotational binaries. We will discuss both cases separately in Sections 9.2 and 9.3.

9.2 Corotational Binaries

The easier case follows from the assumption that the fluid flow vanishes in the frame corotating with the binary

$$V^a = 0, \quad (9.23)$$

which leads to models of *corotating* binaries. With (9.23), the continuity equation (9.15) is solved identically, and the Bernoulli equation (9.14) reduces to

$$\frac{h}{u^t} = \text{const} \equiv C \quad (9.24)$$

(see, e.g., Problem 16.17 in Lightman *et.al.* (1975)).

Using the normalization $u_a u^a = -1$, the u^t component can be expressed in terms of the spatial components u_i as

$$\alpha u^t = \left(1 + \gamma^{ij} u_i u_j\right)^{1/2}. \quad (9.25)$$

²² Like binary black holes (Section 7.1), binary neutron stars in general relativity are not in strict equilibrium. Due to the emission of gravitational radiation, they lose energy and slowly spiral inward. For binaries sufficiently far from the ISCO, however, the inspiral timescale is much longer than the orbital timescale. This justifies the notion of binary neutron stars being in quasi-equilibrium, quasi-circular orbits, as we are assuming here.

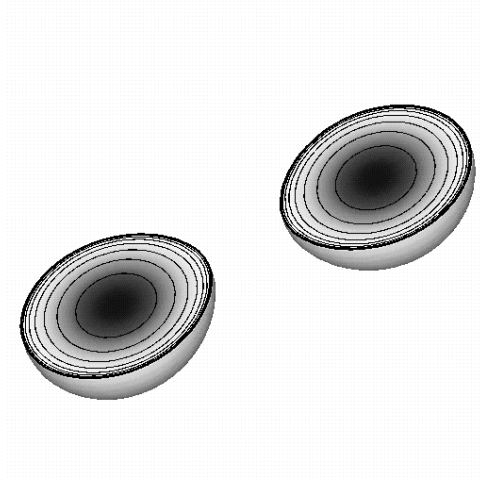


Fig. 9.1. Rest density contours in the equatorial plane for a $n = 1$ neutron star binary close to the ISCO. Each star has a rest mass of $\bar{M} = 0.169$, corresponding to a compaction in isolation of $(M/R)_\infty = 0.175$. The contours show isosurfaces of the rest-density in decreasing factors of 0.556. (Figure from Baumgarte *et.al.* (1998b).)

With $V^a = 0$, and assuming rotation about the z -axis, the four-velocity (9.10) reduces to

$$u^a = u^t(1, -\Omega y, \Omega x, 0). \quad (9.26)$$

Since we are also assuming spatial conformal flatness, (9.25) can then be rewritten as

$$\alpha u^t = \left(1 - \frac{\psi^4}{\alpha^2} \left((\Omega y - \beta^x)^2 + (\Omega x + \beta^y)^2 + (\beta^z)^2 \right) \right)^{-1/2}. \quad (9.27)$$

Inserting this into (9.24) shows that the enthalpy h is given as an algebraic function of α , ψ and β^i , which are determined by the thin-sandwich equations (3.27) to (3.29), and the constants Ω and C . From h the fluid variables ρ_0 , ρ_i and P can be computed. Finally, the matter-sources ρ , j^i and S in (3.27) to (3.29) can be computed in terms of the fluid variables and the velocity from their definitions (2.26), (2.29) and (2.35).

Self-consistent solutions to the Bernoulli equation (9.24) together with the field equations (3.27) to (3.29) can be constructed with iterative algorithms. The

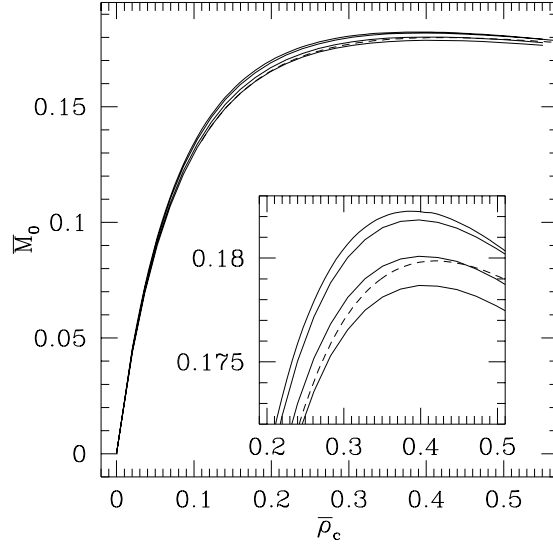


Fig. 9.2. Rest mass \bar{M}_0 versus central density $\bar{\rho}_c$ for separations $z_A = 0.3$ (bottom solid line), 0.2, 0.1 and 0.0 (top line) for corotational, $n = 1$, equal mass binary neutron stars. The dashed line is the Oppenheimer-Volkoff result. Due to finite difference error, the numerical values systematically underestimate the mass, which explains why some of these values are smaller than the corresponding Oppenheimer-Volkoff values. The insert is a blow-up of the region around the maximum masses. (Figure from Baumgarte *et.al.* (1997).)

method of Baumgarte *et.al.* (1997, 1998b) is based on a rescaling algorithm that had been used earlier for the construction of rotating stars (e.g. Hachisu (1986)). Defining the point on the stellar surface that is closest to the equal mass companion as r_A and the one that is furthest from the companion as r_B , Baumgarte *et.al.* (1997, 1998b) specify a particular binary model by the maximum density ρ_0^{\max} and the *relative* separation

$$z_A = r_A/r_B. \quad (9.28)$$

Starting the iteration with an initial guess for the density profile, namely that of a spherical star, the field equations (3.27) to (3.29) can be solved. With a new guess for α , ψ and β^i , the Bernoulli equation (9.24) can be evaluated at r_A , r_B and at the point of maximum density, r_C . At all three points the density is known; at r_A and r_B it vanishes, and at r_C it is pre-determined. These three relations can therefore be solved for constants Ω and C as well as the *absolute* separation r_B ²³. Given these values, the Bernoulli equation can be solved everywhere, yielding an updated guess for the fluid variables. The iteration is continued until a certain accuracy has been achieved. Baumgarte *et.al.* (1997, 1998b) implemented this algorithm in Cartesian coordinates with

²³ In the Bernoulli equation, the gravitational fields α and ψ are rescaled in terms of r_B , so that the latter enters the equation implicitly; see Baumgarte *et.al.* (1998b).

\bar{M}_0	\bar{M}_∞	$(M/R)_\infty$	$M_0\Omega_{\text{ISCO}}$	$(J_{\text{tot}}/M_{\text{tot}}^2)_{\text{ISCO}}$	\bar{M}_{ISCO}
0.0597	0.0582	0.05	0.003	1.69	0.0578
0.1122	0.1066	0.1	0.01	1.22	0.1055
0.1341	0.1259	0.125	0.015	1.12	0.1248
0.153	0.1423	0.15	0.02	1.05	0.1408
0.169	0.1547	0.175	0.025	1.00	0.1529
0.178	0.1625	0.2	0.03	0.97	0.1601

Table 9.1

Numerical results for the orbital angular velocity Ω , angular momentum J and the ADM mass \bar{M} at the ISCO, for corotating, equal mass binary neutron stars with polytropic index $n = 1$. We tabulate the individual rest mass \bar{M}_0 , the mass-energy \bar{M}_∞ and the compaction $(M/R)_\infty$ each star would have in isolation (where R is the Schwarzschild radius), as well as the angular velocity $M_0\Omega$, the angular momentum $J_{\text{tot}}/M_{\text{tot}}^2$ and the ADM mass \bar{M} at the ISCO. For $n = 1$, the maximum rest-mass in isolation is $\bar{M}_0^{\text{max}} = 0.180$. (Table adapted from Baumgarte *et.al.* (1998b).)

a full approximation storage multigrid solver. Other implementations have been used by Marronetti, Mathews and Wilson (1998); Uryū and Eriguchi (2000); Gourgoulhon *et.al.* (2001). A typical binary configuration close to the ISCO is shown in Figure 9.1.

Physical units enter the problem only through the polytropic constant κ in the polytropic equation of state (9.4). It is therefore convenient to nondimensionalize all equations, and present results in terms of dimensionless quantities. Since $\kappa^{n/2}$ has units of length, the non-dimensional mass \bar{M} , for example, is defined as

$$\bar{M} = \kappa^{-n/2} M, \quad (9.29)$$

and similar for other quantities.

One question of interest is how the maximum allowed rest mass changes with separation. In Figure 9.2, the rest mass \bar{M}_0 of $n = 1$ polytropes is plotted as a function of the central density $\bar{\rho}_c = \kappa^n \rho_c$ for different relative separations z_A . Clearly, the maximum allowed mass increases with decreasing separation, suggesting that neutron stars in corotating binaries are more stable than in isolation. Evolutionary sequences can be constructed by keeping the rest mass \bar{M}_0 constant. In Figure 9.2, horizontal lines therefore correspond to evolutionary sequences. Evolving from a large separation to a smaller separation, the central density decreases (see also Figure 9.4 below). Similar results hold for other polytropic indices (Baumgarte *et.al.*, 1998b).

The ISCO can be located by finding, for example, the minimum of the total energy \bar{M} along an evolutionary sequence $\bar{M}_0 = \text{const.}$ According to the relation

$$dM = \Omega dJ \quad (9.30)$$

(equation (33.61) in Misner, Thorne and Wheeler (1973), compare equation (7.12)), a minimum in the energy should coincide with a minimum in the angular momentum. Values of the orbital angular velocity $M_0\Omega$ and angular momentum J/M^2 at the ISCO for different values of the stellar mass \bar{M}_0 are tabulated in Table 9.1 for $n = 1$ polytropes. Baumgarte *et.al.* (1998b) found an ISCO only for sufficiently stiff equations of state, $n \lesssim 1$. This result is in qualitative agreement with various Newtonian results (see, e.g., the review by Rasio and Shapiro (1999)). Stars with softer equations of state are more centrally condensed and have more extended envelopes. Such stars come into contact and merge before encountering an ISCO.

The above arguments – the increase in the maximum allowed mass and the decrease in the central density – suggest that neutron stars in corotating binaries are more stable than in isolation. A rigorous stability analysis, based on turning point methods, comes to the same conclusion and shows that corotating binaries do not encounter any instabilities until they reach the ISCO (Baumgarte *et.al.*, 1998a). These results are in contrast to the claims of Wilson and Mathews (1995), who found in dynamical simulations that neutron stars collapsed to black holes individually before they reached the ISCO (“binary-induced collapse”; compare Section 10.2). It was later found that at least the size these results was erroneous and caused by a mistake in the derivation of the equations (Flanagan, 1999; Mathews and Wilson, 2000). Binary-induced collapse can occur for binaries made of collisionless matter (Shapiro, 1998; Duez *et.al.*, 1999)). As seen in an inertial frame, the neutron stars in corotating binaries are rapidly spinning, and in fact the mass increases found in corotating binaries are quite similar to those found in individual stars spinning with the same angular velocity (see footnote [19] in Baumgarte *et.al.* (1997)). This adds one more motivation to studying irrotational binaries, which are more realistic and where stabilizing effects of rotation are potentially much smaller.

9.3 Irrotational Binaries

The presence of viscosity is necessary to maintain binaries in corotation. Estimates of the viscosity in neutron stars (Kochanek, 1992; Bildsten and Cutler, 1992) show that the viscous timescale is much longer than the inspiral timescale, suggesting that the assumption of corotation is quite unrealistic.

Instead, it may be more reasonable to assume that the typical spin frequency of neutron stars is much less than the orbital frequency of close neutron star binaries. Since the emission of gravitational radiation, which drives the inspiral of compact binaries, conserves circulation, it is then more realistic to assume neutron stars to be *irrotational* (zero circulation), even in close binaries.

The first relativistic formulation for irrotational binaries in quasi-equilibrium was given by Bonazzola, Gourgoulhon and Marck (1997). Inspired by this approach, less complicated formalisms were developed independently by Asada (1998), Teukolsky (1998) and Shibata (1998). Gourgoulhon (1998) demonstrated that all of these formulations are equivalent. The derivation here follows most closely that of Shibata (1998).

In general relativity, the vorticity tensor ω_{ab} is defined as

$$\omega_{ab} = P_a^c P_b^d (\nabla_d(hu_c) - \nabla_c(hu_d)), \quad (9.31)$$

where $P_a^b = g_a^b + u_a u^b$ is the projection operator with respect to the fluid's four-velocity u^a . For irrotational binaries, the vorticity vanishes, and the quantity hu_a can be expressed as the gradient of a potential Φ

$$hu_a = \nabla_a \Phi. \quad (9.32)$$

It is easy to see that with this assumption the Euler equation (9.8) is satisfied identically, while the continuity equation becomes

$$\nabla^a ((n/h) \nabla_a \Phi) = 0 \quad (9.33)$$

(see, e.g., Teukolsky (1998)).

Projecting these relations into Σ shows that for irrotational stars, the three-dimensional vorticity vanishes

$$D_j \hat{u}_i - D_i \hat{u}_j = 0, \quad (9.34)$$

so that

$$\hat{u}_i = D_i \Phi. \quad (9.35)$$

The Bernoulli equation (9.14) then reduces to

$$\frac{h}{u^t} + \hat{u}_i V^i = C, \quad (9.36)$$

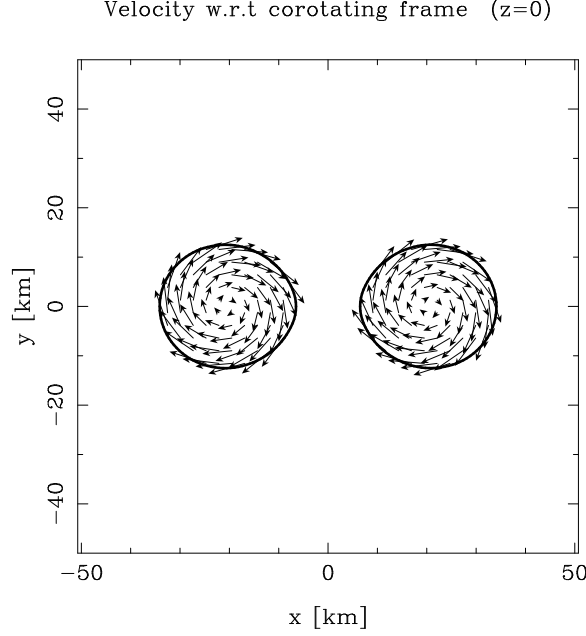


Fig. 9.3. The internal velocity field with respect to the co-orbiting frame in the orbital plane for stars of rest-mass $M_0 = 1.625M_\odot$ at a coordinate separation of 41 km, for an $n = 1$ polytrope with $\kappa = 1.8 \times 10^{-2} \text{Jm}^3\text{kg}^{-2}$. The thick lines denote the surfaces of the stars. (Figure from Gourgoulhon *et.al.* (2001).)

where C is a constant.

It is now convenient to introduce the rotational shift vector

$$B^i = \beta^i + \Omega \xi^i = l^a - \alpha n^a. \quad (9.37)$$

From (9.10), we can express V^a as

$$V^i = \frac{1}{u^t h} D^i \Phi - B^i, \quad (9.38)$$

and the normalization $u^a u_a = -1$ yields

$$\alpha u^t = \left(1 + h^{-2} D_i \Phi D^i \Phi\right)^{1/2} \quad (9.39)$$

(see (9.25)). Inserting (9.38) and (9.39) into the Bernoulli equation (9.36) also yields the following expression for αu^t ²⁴

$$\alpha u^t = \frac{1}{\alpha h} \left(C + B^i D_i \Phi\right). \quad (9.40)$$

²⁴ This relation can also be derived by observing that $\mathcal{L}_1(h\mathbf{u}) = \mathcal{L}_1(\mathbf{d}\Phi) = \mathbf{d}\mathcal{L}_1\Phi = 0$ implies that $l^a \nabla_a \Phi = C$, where C is a constant. Expressing n^a in $h\alpha u^t = h n^a u_a = n^a \nabla_a \Phi$ in terms of l^a and B^i then yields (9.40); see Teukolsky (1998).

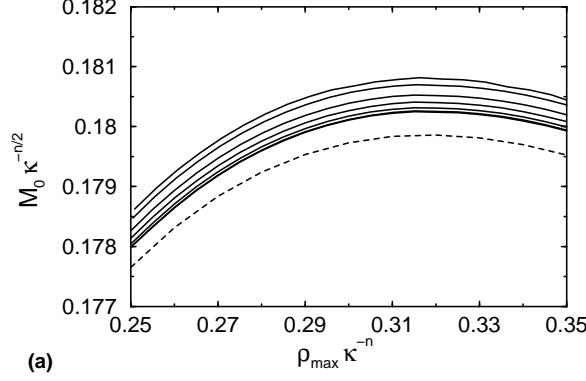


Fig. 9.4. The rest mass \bar{M}_0 as a function of central density $\bar{\rho}_0$ for separations $\bar{d} = 1.3125, 1.375, 1.5, 1.625, 1.75, 1.875$ and 2 (thick lines from top to bottom) for irrotational $n = 1$ binary neutron stars. The dashed line is the Oppenheimer-Volkoff result. (Figure from Uryū, Shibata and Eriguchi (2000).)

The last two equations can be solved for the enthalpy h

$$h^2 = \alpha^{-2}(C + B^i D_i \Phi) - D_i \Phi D^i \Phi. \quad (9.41)$$

An equation for the velocity potential Φ can be found by inserting (9.38) and (9.40) into the continuity equation (9.15)

$$\begin{aligned} D_i D^i \Phi - B^i D_i \left(\frac{C + B^j D_j \Phi}{\alpha^2} \right) - \frac{C + B^j D_j \Phi}{\alpha} K \\ = \left(\frac{C + B^j D_j \Phi}{\alpha^2} B^i - D^i \Phi \right) D_i \frac{\alpha \rho_0}{h}. \end{aligned} \quad (9.42)$$

At the surface of the stars the density vanishes $\rho_0 = 0$, so that regularity of the right hand side implies the boundary condition

$$\left(\frac{C + B^j D_j \Phi}{\alpha^2} B^i - D^i \Phi \right) D_i \rho_0 \Big|_{\text{surface}} = 0. \quad (9.43)$$

This boundary condition can also be derived by requiring that at the surface the fluid flow be tangent to the surface, $u^a \nabla_a \rho_0 = 0$.

Evidently, constructing irrotational binaries is much more involved than constructing corotational binaries. Unlike for corotational binaries, where only one algebraic equation (9.24) has to be solved for the enthalpy, one has to solve the elliptic equation (9.42) for the velocity potential Φ together with the enthalpy equation (9.41). The boundary condition (9.43) has to be imposed on the surface of the star, which adds another complication since the location of the surface is not known a priori.

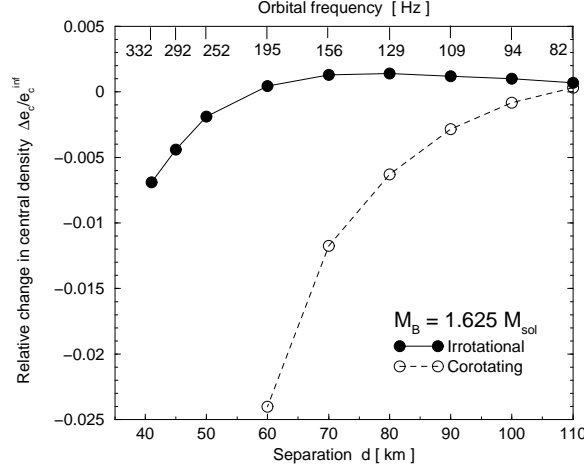


Fig. 9.5. Relative change of the central energy density $e = \rho_0 + \rho_i$ with respect to its value at infinite separation e_c^{inf} as a function of the coordinate separation d (or the orbital frequency $\Omega/(2\pi)$) for corotational and irrotational constant rest mass sequences with $M_0 = 1.625 M_\odot$. The sequences were computed for a $n = 1$ polytrope with $\kappa = 1.8 \times 10^{-2} \text{Jm}^3 \text{kg}^{-2}$. (Figure from Bonazzola, Gourgoulhon and Marck (1999a).)

Bonazzola, Gourgoulhon and Marck (1999a) and Gourgoulhon *et.al.* (2001) solved this problem with the help of a multi-domain, spectral method. In this method, space is covered with several patches of coordinate systems. In particular, the interiors of the stars are covered with spherical-type coordinate systems, which are constructed so that the surface of the star lies at a constant value of the radial coordinate. Such coordinate systems are called “surface-fitting” coordinates, and are very well suited for imposing the boundary condition (9.43). A similar algorithm, based on Newtonian simulations of irrotational neutron star binaries (Uryū and Eriguchi, 1998a,b), was used by Uryū and Eriguchi (2000) and Uryū, Shibata and Eriguchi (2000). Marronetti, Mathews and Wilson (1999) constructed irrotational models of neutron star binaries in Cartesian coordinates. They simplified the boundary condition (9.43) by assuming that the stars are spherical, so that the gradient of the density in (9.43) is aligned with a radial vector. While this may be adequate as long as the separation between the stars are large, this approximation seems problematic for small separation, and may explain why the results of Marronetti, Mathews and Wilson (1999) differ from those of Bonazzola, Gourgoulhon and Marck (1999a); Gourgoulhon *et.al.* (2001); Uryū and Eriguchi (2000) and Uryū, Shibata and Eriguchi (2000) for close binaries.

A typical binary configuration and its internal velocity field is shown in Figure 9.3. The maximum allowed mass of neutron stars in irrotational binaries can be found by finding the mass as a function of central density for fixed separation. Results of Uryū, Shibata and Eriguchi (2000) are shown in Figure 9.4. This demonstrates that, as in corotational binaries, the maximum

\bar{M}_0	\bar{M}_∞	$(M/R)_\infty$	$M_0\Omega_{\text{CUSP}}$	$(J_{\text{tot}}/M_{\text{tot}}^2)_{\text{CUSP}}$	\bar{M}_{CUSP}
0.112	0.107	0.1	0.0106	1.09	0.105
0.130	0.122	0.12	0.0144	1.02	0.121
0.146	0.136	0.14	0.0187	0.971	0.135
0.166	0.153	0.17	0.0263	0.919	0.150
0.175	0.160	0.19	0.0320	0.895	0.157

Table 9.2

Numerical results for the orbital angular velocity Ω , the angular momentum J and the ADM mass \bar{M} at cusp formation, for irrotational binary neutron stars with polytropic index $n = 1$. We tabulate the individual rest mass \bar{M}_0 , the mass-energy \bar{M}_∞ , the compaction $(M/R)_\infty$ each star would have in isolation, as well as the angular velocity $M_0\Omega$, the angular momentum $J_{\text{tot}}/M_{\text{tot}}^2$ and ADM mass \bar{M} at cusp formation. For $n = 1$, the maximum rest-mass in isolation is $\bar{M}_0^{\text{max}} = 0.180$. (Table adapted from Uryū, Shibata and Eriguchi (2000).)

mass increases with decreasing separation. However, comparing with Figure 9.2, we find that the increase in maximum mass is smaller for irrotational binaries than for corotational binaries (especially taking into account that the fairly coarse resolution results of Baumgarte *et.al.* (1998b) underestimate the masses in Figure 9.2). This result is not surprising, since neutron stars in corotational binaries are rotating with respect to the rest frame of the binary, which by itself increases their maximum mass (e.g. Cook, Shapiro and Teukolsky (1994)). It is also evident from Figures 9.4 and 9.2 that while the density along evolutionary sequences $\bar{M}_0 = \text{const}$ of irrotational binaries decreases with decreasing separation, the decrease is less than for corotational binaries. This can be seen more clearly in Figure 9.5, which demonstrates that while it is possible that the central density increases with decreasing separation by a very small amount for intermediate separations in irrotational binaries, it certainly decreases for small separations where tidal deformation dominates over any other effects. Similar results were found by Uryū and Eriguchi (2000) and Uryū, Shibata and Eriguchi (2000). While these findings have no immediate implications for the stability of neutron stars in irrotational binaries, they offer no evidence for an instability as initially reported by Wilson and Mathews (1995).

While evolutionary sequences of corotational binaries end either at the ISCO or at contact, irrotational sequences typically end with the formation of a cusp before they reach the ISCO (Bonazzola, Gourgoulhon and Marck, 1999a; Uryū and Eriguchi, 2000; Uryū, Shibata and Eriguchi, 2000). As analyzed by Uryū, Shibata and Eriguchi (2000), this cusp corresponds to an inner Lagrange point, across which neutron stars will transfer mass. Such configurations are likely to form dumbbell-like structures, with mass flowing between the two stars. Uryū, Shibata and Eriguchi (2000) find that only binaries with very stiff equations

of state ($n \lesssim 2/3$) reach an ISCO before they form a cusp, while binaries with softer equations of state form a cusp first. Numerical values for irrotational $n = 1$ binaries at cusp formation are listed in Table 9.2. Comparing with the ISCO values of corotational binaries in Table 9.1, one finds that the cusp and ISCO occur at very similar frequencies. The corotational binaries have more angular momentum, because the individual stars carry a spin angular momentum in addition to the orbital angular momentum of the binary. We also find that the binding energy $(\bar{M} - \bar{M}_\infty)/\bar{M}_0$ of corotational binaries is slightly larger than for irrotational binaries, because the ADM mass \bar{M} of the former include the additional spin kinetic energy of the individual stars (see also the discussions in Duez *et.al.* (2002) and Section 10.4). More numerical results and a detailed discussion of the ISCO and cusp formation in irrotational binaries can be found in Uryū, Shibata and Eriguchi (2000).

10 Dynamical Simulations of Binary Neutron Stars

In this Section we present approaches and results for dynamical simulations of binary neutron stars. We discuss formulations of relativistic hydrodynamics in Section 10.1, the conformal flatness approximation in Section 10.2, fully self-consistent simulations in Section 10.3, and a quasi-adiabatic approximation of the slow inspiral just outside of the ISCO in Section 10.4.

10.1 Relativistic Hydrodynamics

Since numerical hydrodynamics in general relativity has been the subject of a recent review (Font, 2000) we will provide only a very brief overview.

The equations of relativistic hydrodynamics can be derived from the local conservation laws of the stress-energy tensor T^{ab} (9.7)

$$\nabla_a T^{ab} = 0 \tag{10.1}$$

and the continuity equation (9.9)

$$\nabla_a (\rho_0 u^a) = 0, \tag{10.2}$$

where ρ_0 is the rest mass density and u^a the fluid four-velocity. For a perfect fluid, the stress-energy tensor is (9.2)

$$T^{ab} = (\rho_0 + \rho_i + P)u^a u^b + P g^{ab} \tag{10.3}$$

where ρ_i is the internal energy density and P the pressure.

The equations of motion can be derived from (10.1) and (10.2) in various different ways, depending on how the basic dynamical fluid variables are defined. One might be tempted to adopt a projection of T^{ab} with respect to the normal vector n^a , which yields the matter variables ρ (2.26) and j^i (2.29) as they appear in the ADM equations. It turns out, however, that projections with respect to the fluid four-velocity u^a yields equations that are simpler and closer to the Newtonian equations of hydrodynamics.

Wilson (1972, see also Hawley, Smarr and Wilson (1984a,b); Wilson and Mathews (1989); Wilson, Mathews and Marronetti (1996)), who pioneered the field of relativistic hydrodynamics in multi-dimensions, used the density definition $D = W\rho_0$, where W is the Lorentz factor between the fluid four-velocity u^a and normal observers n^a

$$W \equiv n_a u^a = \alpha u^t. \quad (10.4)$$

The equation of continuity (10.2) then becomes

$$\partial_t(\sqrt{\gamma}D) + \partial_j(\sqrt{\gamma}Dv^j) = 0. \quad (10.5)$$

Here $v^i = u^i/u^t$ is the transport velocity with respect to a coordinate observer, and γ is the determinant of the spatial metric γ_{ij} . Defining the momentum as $S_a = \rho_0 h W u_a$, the spatial components of (10.1) reduce to the Euler equation

$$\frac{1}{\sqrt{\gamma}}\partial_t(\sqrt{\gamma}S_i) + \frac{1}{\sqrt{\gamma}}\partial_j(\sqrt{\gamma}S_i v^j) = -\alpha\partial_i P - \frac{S_a S_b}{2S^0}\partial_i g^{ab}. \quad (10.6)$$

The time component S^0 is found from the spatial components through the normalization $u^a u_a = -1$. With the energy density $E = W\rho_i$, the timelike component of (10.1) yields the energy equation

$$\partial_t(\sqrt{\gamma}E) + \partial_j(\sqrt{\gamma}E v^j) = -P \left(\partial_t(\sqrt{\gamma}W) + \partial_i(\sqrt{\gamma}W v^i) \right). \quad (10.7)$$

Shibata (1999a, see also Shibata, Baumgarte and Shapiro (1998)) modified this scheme by absorbing the determinant into the definition of the density $\rho_* = \sqrt{\gamma}W\rho_0$, for which the equation of continuity becomes

$$\partial_t \rho_* + \partial_j(\rho_* v^j) = 0. \quad (10.8)$$

Also, for gamma-law equations of state

$$P = (\Gamma - 1)\rho_i \quad (10.9)$$

the source term on the right hand side of the energy equation (10.7) can be eliminated

$$\partial_t e_* + \partial_j (e_* v^j) = 0 \quad (10.10)$$

if the energy variable is defined as $e_* = \sqrt{\gamma} W \rho_i^{1/\Gamma}$. Defining $\tilde{u}_i = h u_i$, the Euler equation (10.6) becomes

$$\begin{aligned} \partial_t (\rho_* \tilde{u}_i) + \partial_j (\rho_* \tilde{u}_i v^j) = & -\alpha e^{6\phi} \partial_i P - \rho_* \left(W h \partial_i \alpha - \tilde{u}_j \partial_i \beta^j \right. \\ & \left. + \frac{\alpha e^{-4\phi} \tilde{u}_j \tilde{u}_k}{2 W h} \partial_i \bar{\gamma}^{jk} - \frac{2 \alpha h (W^2 - 1)}{W} \partial_i \phi \right) \end{aligned} \quad (10.11)$$

where we have expressed the right hand side of (10.6) in terms of the metric quantities introduced in the BSSN formalism (Section 4.3; in particular $\sqrt{\gamma} = e^{6\phi}$). The transport velocity v^i can be found from

$$v^i = -\beta^i + \frac{\alpha \bar{\gamma}^{ij} \tilde{u}_j}{W h e^{4\phi}}, \quad (10.12)$$

and W can be found from the normalization (9.25), which can be expressed as

$$W^2 = 1 + \frac{\bar{\gamma}^{ij} \tilde{u}_i \tilde{u}_j}{e^{4\phi}} \left(1 + \frac{\Gamma e_*^\Gamma}{\rho_* (W e^{6\phi})^{\Gamma-1}} \right)^{-2}. \quad (10.13)$$

Example 10.1 *For static configurations we have $\tilde{u}_i = 0$ and hence $W = 1$ and, in the BSSN formulation, $\rho_* = e^{6\phi} \rho_0$. The Euler equation (10.11) then reduces to*

$$\alpha \partial_i P + \rho_0 h \partial_i \alpha = 0, \quad (10.14)$$

which can be combined with (9.6) to yield equation (9.19) of Example 9.1 for hydrostatic equilibrium.

Other groups have cast the equations of relativistic hydrodynamics into the flux-conservative form

$$\partial_t \mathcal{U} + \partial_i \mathcal{F}^i = \mathcal{S} \quad (10.15)$$

where \mathcal{U} is the state vector containing the so-called primitive fluid variables, \mathcal{F} is the flux vector, and the source vector \mathcal{S} does not contain any derivatives of the fluid variables (see, e.g., Martí, Ibáñez and Miralles (1991), Font (2000)

and references therein). Font *et.al.* (2000, 2001) have implemented such a scheme with

$$\mathcal{U} = \begin{pmatrix} \tilde{D} \\ \tilde{S}_j \\ \tilde{\tau} \end{pmatrix} = \begin{pmatrix} \sqrt{\gamma} W \rho_0 \\ \sqrt{\gamma} \rho_0 h W^2 \tilde{v}_j \\ \sqrt{\gamma} (\rho_0 h W^2 - P - W \rho_0) \end{pmatrix}, \quad (10.16)$$

where $\tilde{v}^i = u^i/W + \beta^i/\alpha$ is the velocity of the fluid with respect to a normal observer, and where γ is the determinant of the spatial metric γ_{ij} . The flux vector \mathcal{F} is then given by

$$\mathcal{F}^i = \begin{pmatrix} (\alpha \tilde{v}^i - \beta^i) \tilde{D} \\ (\alpha \tilde{v}^i - \beta^i) \tilde{S}_j + \alpha \sqrt{\gamma} P \delta^i_j \\ (\alpha \tilde{v}^i - \beta^i) \tilde{\tau} + \alpha \sqrt{\gamma} \tilde{v}^i P \end{pmatrix}, \quad (10.17)$$

and the source vector \mathcal{S} by

$$\mathcal{S} = \begin{pmatrix} 0 \\ \alpha \sqrt{\gamma} T^{ab} g_{bc} {}^{(4)}\Gamma_{aj}^c \\ \alpha \sqrt{\gamma} (T^{a0} \partial_a \alpha - \alpha T^{ab} {}^{(4)}\Gamma_{ab}^0) \end{pmatrix}. \quad (10.18)$$

The virtue of these schemes is that the local characteristic structure can be determined, which is crucial for the implementation of high-resolution shock-capturing schemes (see below).

Once the equations have been brought into a particular form, a numerical strategy for their numerical implementation has to be chosen (see Font (2000)). This is true for all equations in this article, but hydrodynamics poses the additional challenge that shocks may appear. In a shock, hydrodynamic quantities develop discontinuities when perfect fluids are assumed, and macroscopic fluid flow is converted into internal energy. Neither one of these phenomena can be captured by traditional finite difference schemes, which therefore have to be modified.

Von Neumann and Richtmyer (1950) suggested an *artificial viscosity* scheme, in which an artificial term Q is added to the pressure P . They showed that the jump conditions across shocks are well satisfied for a Newtonian, one-

dimensional fluid flow if Q is defined as

$$Q = \begin{cases} -\rho(k\Delta x)^2(\partial_x v)^2 & \text{if } \partial_x v < 0 \\ 0 & \text{otherwise,} \end{cases} \quad (10.19)$$

where Δx is the grid resolution and k an adjustable constant of order unity. The effect of the artificial viscosity is to spread out the shock over approximately k gridzones. It appears in the source terms of the Euler equation (10.6) and the energy equation (10.7), and, as desired, converts the kinetic energy of bulk fluid flow into internal energy in accord with the Rankine-Hugoniot jump conditions.

Artificial viscosity schemes have been generalized for applications in general relativistic hydrodynamics by numerous authors (including May and White (1966); Wilson (1972); van Riper (1979); Shapiro and Teukolsky (1980); Baumgarte, Shapiro & Teukolsky (1995); Shibata (1999a)). These schemes have the virtue of being quite robust and very easy to implement. However, it has been shown that artificial viscosity schemes do not work well for ultra-relativistic fluid flow (Norman and Winkler, 1986).

Alternatively, *high-resolution shock-capturing* (HRSC) schemes can be employed. These schemes are based on the idea of treating all fluid variables as constant in each grid cell. The discontinuity at each grid interface can then be viewed as the initial data for a Riemann shock tube problem, which can be solved either exactly or approximately. These schemes rely on the local characteristic structure of the equations for the solution of the Riemann problem, and are therefore used with equations in flux-conservative form, (Font *et.al.*, 2000, 2001). By construction HRSC are capable of handling shocks and do not need additional artificial viscosity terms. In various applications, HRSC have been found to be more accurate than artificial viscosity schemes, in particular for highly relativistic flows. For more information on HRSC schemes in relativistic hydrodynamics see the review articles by Martí and Müller (1999) and Font (2000).

It is also possible to avoid finite difference methods altogether, and to solve the equations of relativistic hydrodynamics with either *smoothed particle hydrodynamics* (SPH) or *spectral* methods. SPH methods are quite common in Newtonian hydrodynamics, and have also been applied in relativistic hydrodynamics in stationary spacetimes (see Font (2000) for references). Quite recently, SPH methods have also been used for the modeling of binary neutron star coalescence in post-Newtonian theory (Faber and Rasio, 2002) as well as in full general relativity (Oechslin, Rosswog and Thielemann, 2002). Spectral methods (see Bonazzola, Gourgoulhon and Marck (1999b) for a review) have been used quite commonly for the solution of the elliptic equations in ini-

tial value problems (e.g. Bonazzola, Gourgoulhon and Marck (1999a); Grandclément, Gourgoulhon and Bonazzola (2002); Gourgoulhon *et.al.* (2001)) and recently also for the dynamical evolution of gravitational (vacuum) fields (Kidder, Scheel and Teukolsky, 2001). For hydrodynamic simulations, in particular in three dimensions, spectral methods are less common because of difficulties in treating the discontinuities in shocks, which lead to spurious oscillations (Gibbs phenomenon).

10.2 The Wilson-Mathews approximation

Wilson and Mathews (1989, 1995, also Wilson, Mathews and Marronetti (1996)) pioneered the conformal flatness approximation to the simulation of neutron star binaries. In this approach, one assumes that the dynamical degrees of freedom of the gravitational fields, i.e. the gravitational radiation, play a negligible role for the structure of binary neutron stars. To simplify the metric and the field equations, Wilson and Mathews (1989, 1995) therefore suggest assuming that the spatial metric is conformally flat, so that the spacetime metric takes the simplified form

$$ds^2 = -\alpha^2 dt^2 + \psi^4 \eta_{ij} (dx^i + \beta^i dt)(dx^j + \beta^j dt). \quad (10.20)$$

Wilson and Mathews (1989, 1995) further assume that the spatial metric remains conformally flat at all times. The traceless part of equation (2.46) then has to vanish, which yields

$$A^{ij} = \frac{1}{2\alpha} (L\beta)^{ij}. \quad (10.21)$$

Here A^{ij} is the traceless part of the extrinsic curvature, and the vector gradient L is defined in (3.10).

Equation (10.21) can be inserted into the momentum constraint (2.45), resulting in an equation for the shift β^i . The conformal factor ψ can be found from the Hamiltonian constraint (2.44), and to determine the lapse α Wilson and Mathews (1995) adopt maximal slicing (Section 5.2). If one also adopts the conformal rescaling (3.7), these equations reduce to the thin-sandwich equations (3.27) through (3.29), which now completely determine the metric (10.20).

All unknowns in the metric (10.20) are determined by elliptic equations, and in this sense dynamical degrees of freedom have been removed from the gravitational fields. In this approach, one solves an initial value problem at each instant of time, as opposed to dynamically evolving the gravitational fields.

While one may worry about the accuracy of this approximation (see also Appendix C), it greatly simplifies the field equations and allowed Wilson and Mathews (1995) to perform the first fairly detailed simulations of binary neutron stars. In this approach, the time step is limited by the matter sound speed and not the light speed, so it can be much larger than in fully self-consistent algorithms.

In these simulations, Wilson and Mathews (1995) combined equations (3.27) through (3.29) for the metric (10.20) with Wilson’s formulation of the relativistic equations of hydrodynamics (10.5) through (10.7). In each timestep, one first evolves the matter variables, and then solves the field equations for the metric (10.20) with the new density distribution as sources. If desired, the gravitational wave emission can be estimated with the quadrupole formula.

The initial results of Wilson and Mathews (1995) showed a so-called crushing effect, in which the neutron stars were compressed to very high densities even far outside of the ISCO, and ultimately collapsed to two individual black holes (“binary-induced collapse”). Since this effect contradicted expectations from Newtonian and post-Newtonian theory as well as relativistic quasi-equilibrium results (which predict that the density should be reduced by tidal deformations, see Sections 9.2 and 9.3), their findings spurned a fairly intense debate until it was discovered that at the very least the size of the effect was caused by an inconsistency in the derivation of the equations (Flanagan, 1999; Mathews and Wilson, 2000).

The unfortunate consequence of this debate is that the assumption of conformal flatness itself was often incorrectly blamed for the spurious results. While this approximation is obviously not suitable for every situation, it may be very good for the modeling of compact objects in some regimes, where its errors are probably much smaller than other sources of error (see also the discussion in Appendix C). It has recently been adopted by Oechslin, Rosswog and Thielemann (2002), who combined it with an SPH method to solve the equations of relativistic hydrodynamics.

10.3 Fully Self-consistent Simulations

Several groups have launched efforts to self-consistently solve the equations of relativistic hydrodynamics together with Einstein’s equations, and model the coalescence and merger of binary neutron stars (Oohara and Nakamura, 1997; Baumgarte *et.al.*, 1999; Font *et.al.*, 2000, 2001). The first successful simulations of binary neutron star mergers are those of Shibata and Uryū (2000a, see also Shibata (1999a); Shibata and Uryū (2002)), which we will focus on in this Section.

Model	$\bar{\rho}_{\max}$	\bar{M}_0	\bar{M}	J/M^2	remnant
I1	0.0726	0.261	0.242	0.98	neutron star
I2	0.120	0.294	0.270	0.93	black hole
I3	0.178	0.332	0.301	0.88	black hole

Table 10.1

Summary of the initial data for the coalescence simulations of $n = 1$ irrotational binary neutron stars by Shibata and Uryū (2000a). Here \bar{M}_0 , \bar{M} and J are the total rest mass, mass and angular momentum of the binary. In these dimensionless units, the maximum allowed rest mass of an isolated, non-rotating star is $\bar{M}_0^{\max} = 0.180$. (Table adapted from Shibata and Uryū (2000a).)

Shibata and Uryū (2000a) adopt a gamma-law equation of state (10.9) with index $\Gamma = 2$ ($n = 1$). They solve the equations of relativistic hydrodynamics in the form (10.8) to (10.11), and Einstein’s equations in the original form (Shibata and Nakamura, 1995) of what is now often referred to as the BSSN equations (Section 4.3). They use “approximate maximal slicing” (Section 5.2) to specify the lapse α and “approximate minimal distortion” (Section 5.4) to determine the shift β^i . They also add a radial component to the shift vector to avoid grid-stretching in collapse situations.

As initial data, Shibata and Uryū (2000a) prepare equal-mass polytropic ($n = 1$) models of binary neutron stars in quasi-equilibrium with both corotational (see Section 9.2) and irrotational (Section 9.3) velocity profiles. For both velocity profiles they prepare three different models with individual stellar masses ranging from about 75% to 100% of the maximum allowed mass of non-rotating stars in isolation. For corotating models, Shibata and Uryū (2000a) adopt the contact models ($z_A = 0$ in the parametrization (9.28)) as initial data, which are fairly close to the ISCO (see Section 9.2). Irrotational sequences terminate at cusp formation (see Section 9.3), which is still outside of the ISCO. Shibata and Uryū (2000a) therefore adopt the cusp model as initial data, and induce collapse by artificially reducing the angular momentum by about 2.5%. Since irrotational velocity profiles are probably more realistic, we will discuss their models (I1), (I2) and (I3) for irrotational binaries. The initial data for these three models are summarized in Table 10.1 (more information can be found in Table 1 of Shibata and Uryū (2000a)).

The first simulation, model (I1) in Shibata and Uryū (2000a), is for a binary of total rest mass $\bar{M}_0 = 0.261$ ²⁵. The angular momentum of the initial data is $J/M^2 = 0.98$, where M is the total gravitational mass, and is hence smaller than the Kerr limit $J/M^2 = 1$. We show snapshots of density contours in Figure 10.1.

²⁵ We have converted the units of Shibata and Uryū (2000a) into the same dimensionless units adopted in Section 9 for easier comparison.

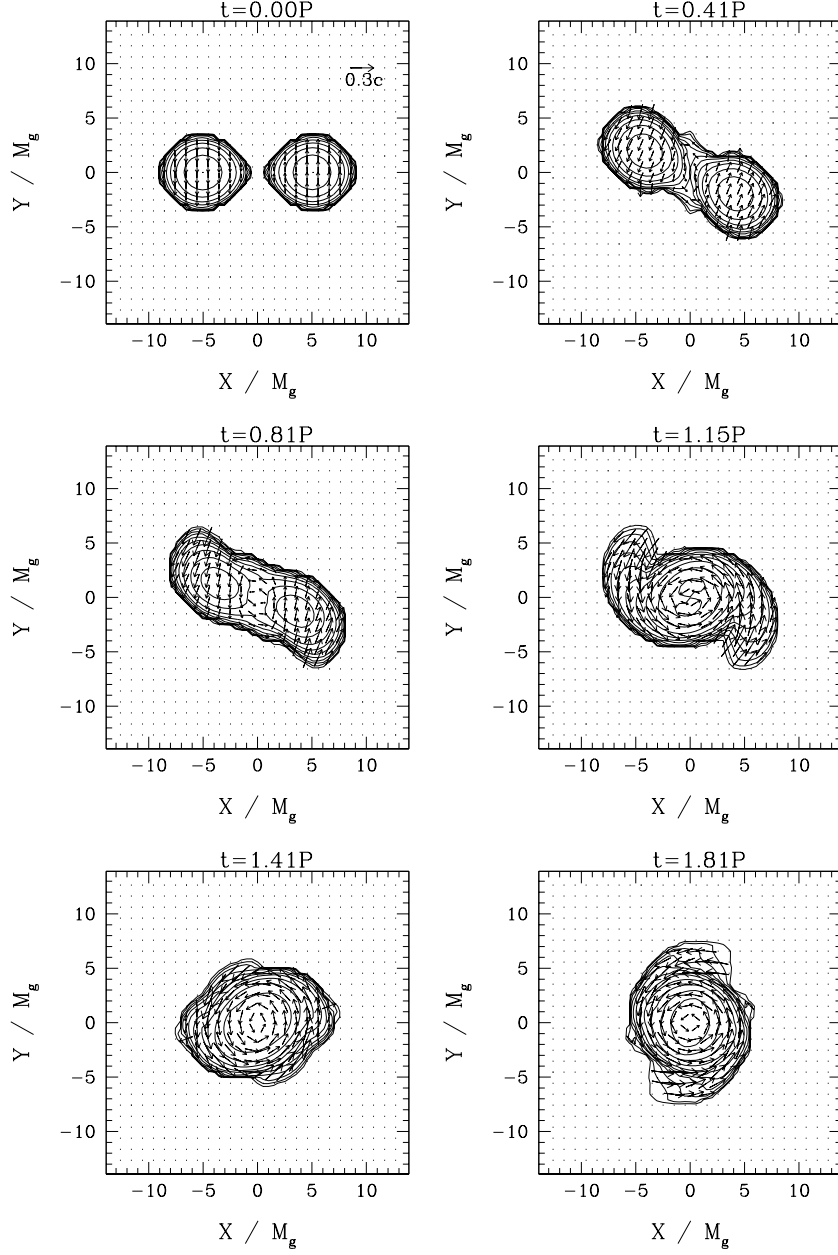


Fig. 10.1. Snapshots of density contours for ρ_* (see equation (10.8)) and the velocity field (v^x, v^y) in the equatorial plane for the coalescence of an irrotational binary of total rest mass $\bar{M}_0 = 0.261$ (Model (I1) in Shibata and Uryū (2000a)). Time is measured in terms of the orbital period P . The contour lines denote densities $\rho_*/\rho_{* \text{ max}} = 10^{-0.3j}$ with $\rho_{* \text{ max}} = 0.255$ and $j = 0, 1, 2, \dots, 10$. (Figure from Shibata and Uryū (2000a).)

In contrast to the coalescence of corotational binaries, no significant spiral arms form during merger, and hardly any matter is ejected. It is quite surprising then that the remnant settles down to a near-equilibrium neutron star

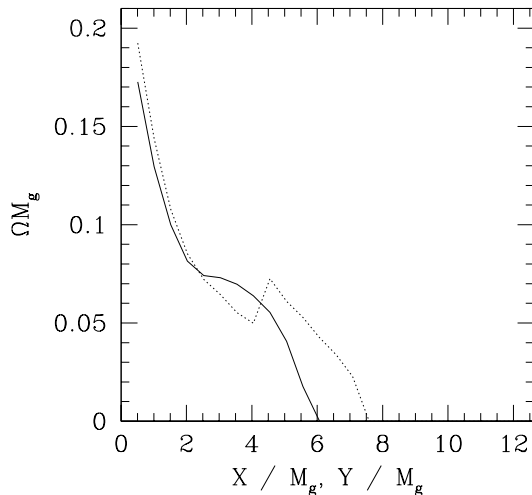


Fig. 10.2. The angular velocity Ω along the x -axis (solid line) and the y -axis (dotted line) at $t = 1.81P_{\text{orb}}$ for model (I1). Here M_g is the gravitational mass M . (Figure from Shibata and Uryū (2000a).)

and does not collapse to a black hole²⁶, even though its rest mass exceeds the maximum allowed rest mass of a spherical, non-rotating star by about 45%. Shibata and Uryū (2000a) find only small amounts of shock heating, which rules out thermal pressure as providing the extra support. As we have pointed out, the angular momentum J/M^2 is smaller than the Kerr limit and therefore cannot prevent black hole formation. Uniform rotation can increase the maximum allowed rest mass for $\Gamma = 2$ polytropes by only about 20% (Cook, Shapiro and Teukolsky, 1994). However, Shibata and Uryū (2000a) find that the core is differentially rotating as opposed to uniformly rotating, as shown in Figure 10.2.

It is quite intuitive that differential rotation may significantly increase the maximum mass (Baumgarte, Shapiro & Shibata, 2000). For uniform rotation, the angular velocity, and hence the centrifugal force which balances the gravitational force to increase the maximum mass, is limited by the Kepler limit at the equator, above which matter there would no longer be gravitationally bound (the “mass-shedding limit”). For differential rotation, the core may rotate faster than the equator, and may further increase the maximum mass without violating the Kepler limit at the equator. Baumgarte, Shapiro & Shibata (2000) have found that differential rotation is very effective in increasing the maximum mass, and have found mass increases of over 60% even for very modest degrees of differential rotation.

The remnant formed in this simulation is supported by differential rotation, as

²⁶ At least not on a dynamical timescale – see below.

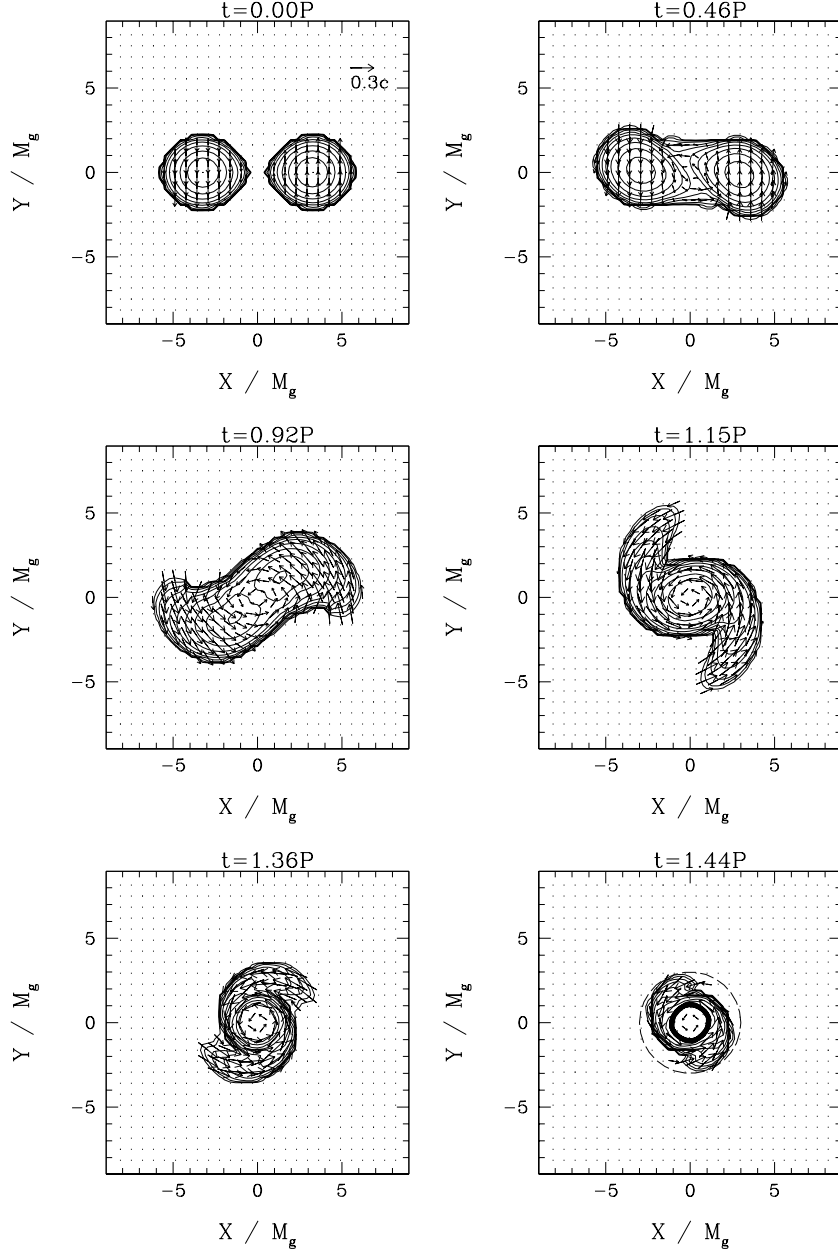


Fig. 10.3. Same as Figure 10.1, but for a binary of total rest mass $\bar{M}_0 = 0.332$ (Model (I3) in Shibata and Uryū (2000a)). Contour lines denote densities $\rho_*/\rho_{* \max} = 10^{-0.3j}$ with $\rho_{* \max} = 0.866$ and $j = 0, 1, 2, \dots, 10$. The dashed line in the last snapshot is the circle $r = 3M$ which encloses over 99% of the total rest mass. The thick solid line at $r \approx M$ denotes the location of the apparent horizon. (Figure from Shibata and Uryū (2000a).)

the thermal pressure support is minimal while its rest mass exceeds the maximum allowed rest mass by about 45%. Similar results were found more recently by Oechslin, Rosswog and Thielemann (2002), who used a completely independent numerical method (namely an SPH method to model the hydrodynamics and the Wilson-Mathews approximation to model the gravitational fields).

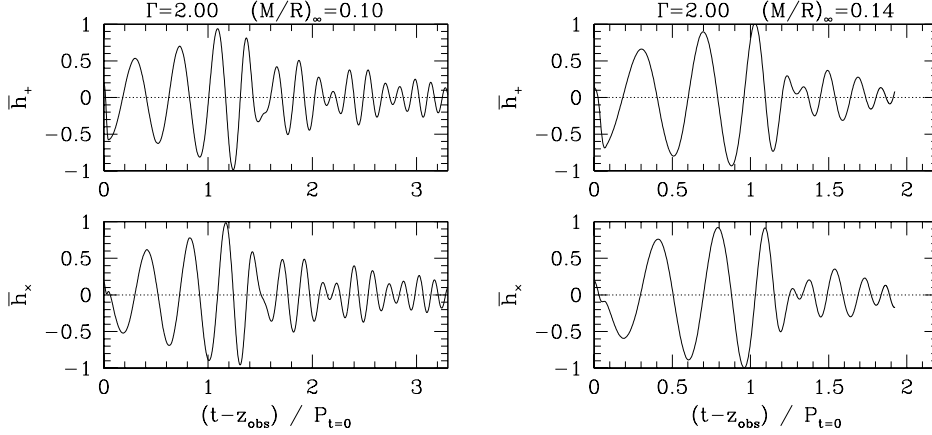


Fig. 10.4. Gravitational wave amplitudes h_+ and h_\times as a function of retarded time for the irrotational binary neutron star models (E) and (H) of Shibata and Uryū (2002). Model (E) corresponds to a slightly smaller mass than (I1) and results in a differentially rotating neutron star, while model (H) is similar to model (I2) and results in a black hole. (Figures from Shibata and Uryū (2002).)

This result is quite surprising, since up to then it was usually assumed that such massive neutron stars collapse to black holes on a dynamical timescale. (although earlier Newtonian merger calculations already foreshadowed this result; see Rasio and Shapiro (1999) and references therein). Instead, it is possible that such “hyper-massive” remnants are dynamically stable and collapse to black holes on a secular timescale, after some dissipative mechanism, for example viscosity or, more likely, magnetic fields, has brought the star into more uniform rotation (Baumgarte, Shapiro & Shibata, 2000; Shapiro, 2000).

Both models (I2) and (I3), for which the total rest mass exceeds the maximum allowed mass by 63% and 85% (see Table 10.1), form a black hole within a dynamical timescale upon merger. In Figure 10.3 we show snapshots of the density contours and velocity profiles for the more massive model (I3). In the last frame of Figure 10.3 the thick solid line denotes the location of an apparent horizon (see Section 6.1), indicating the formation of a black hole.

Shibata and Uryū (2000a) find fairly similar results for corotational binary models. Probably the most significant difference is that corotational binaries have more angular momentum in the outer parts of the binary, which leads to the formation of spiral arms during the coalescence. The spiral arms contain a few percent of the total mass, and may ultimately form a disk around the central object.

In the simulations of Shibata and Uryū (2000a) one of the largest limitations on the accuracy were the outer boundaries, which, because of limited computational resources, had to be imposed well within a wavelength of the gravitational radiation from the binary (at about $\lambda_{\text{gw}}/3$). This means that the

waves were extracted without being in the radiation zone, which necessarily introduces error. After having gained access to a more powerful supercomputer, Shibata and Uryū (2002) therefore repeated these calculations on computational grids that extend to about a gravitational wavelength. Qualitatively, these improved results are very similar to their earlier ones, although the onset of black hole formation shifts to slightly smaller masses. Most strongly affected by these improvements are the gravitational wave forms. In Fig 10.4, we therefore show examples from these improved simulations for models that are similar to model (I1), leading to a differentially rotating neutron star, and model (I2), leading to a black hole.

While the simulations of Shibata and Uryū (2000a, 2002) are pioneering, it would be desirable to confirm their findings with independent simulations with fully self-consistent codes. Many aspects of the simulations could also be improved in the future, including the setup of the initial data (eliminating the need for an artificial reduction of the angular momentum), the extraction of gravitational radiation, and the handling of the hydrodynamics. For example, coalescing irrotational neutron stars form a vortex sheet at the contact surface that is Kelvin-Helmholtz unstable on all wavelength (see, e.g., Rasio and Shapiro (1999) and references therein). Reliably simulating such sheets is quite challenging, and is likely to require more sophisticated algorithms than artificial viscosity schemes (compare Section 10.1, Font *et.al.* (2000, 2001)). Lastly it should be emphasized that these simulations assume polytropic stars governed by a gamma-law equation of state, which is an idealization. In reality, a number of factors, including effects of a realistic nuclear equation of state, magnetic fields and neutrino transport, may play an important role in the coalescence of binary neutron stars. It will probably be a while until all these can be incorporated in fully dynamical and self-consistent simulations.

10.4 *The Quasi-Adiabatic Inspiral of Binary Neutron Stars*

As we have discussed in Section 1, it is possible that other means of modeling binary neutron stars, in particular PN point-mass techniques, break down somewhat outside of the ISCO, when finite-size and relativistic effects become important. It is hard to imagine that fully hydrodynamical numerical calculations would be able to follow the inspiral reliably from such a point outside of the ISCO through many orbital periods to the onset of instability at the ISCO, followed by plunge and merger. Such calculations would accumulate significant amounts of numerical error and would be computational prohibitive. This leaves a gap between the regimes that PN and fully numerical calculations can model. Filling this gap for the late inspiral, immediately prior to plunge, therefore requires an alternative, approximate approach (in the case of binary black holes, this problem has been called the “intermediate binary

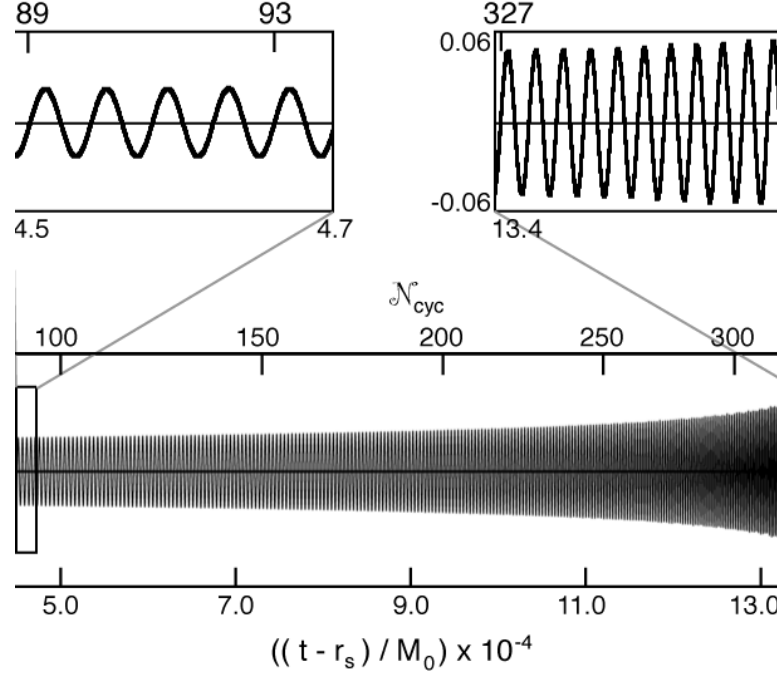


Fig. 10.5. The final hundreds of cycles of the inspiral waveform h_+ or h_\times on the axis of rotation as a function of retarded time and cycle number for an irrotational binary neutron star system. Also indicated is the gravitational strain h for a binary of total rest mass $M_0 = 2 \times 1.5M_\odot$ at a separation of 100 Mpc. (Figure from Duez *et.al.* (2002).)

black hole” problem (Brady, Creighton and Thorne, 1998)).

Several different such approaches have been suggested (Blackburn and Deweiler, 1992; Brady, Creighton and Thorne, 1998; Laguna, 1999; Whelan and Romano, 1999; Whelan, Krivan and Price, 2000; Duez, Baumgarte and Shapiro, 2001; Duez *et.al.*, 2002; Shibata and Uryū, 2001). Here we will focus on the “hydro-without-hydro” approach (see also Baumgarte, Hughes and Shapiro (1999)) adopted by Duez, Baumgarte and Shapiro (2001) and Duez *et.al.* (2002) (see also Yo, Baumgarte and Shapiro (2001a), who illustrated and calibrated this approach in a scalar gravitation model problem).

This approach approximates the binary orbit outside of the ISCO as circular, and treats the orbital decay as a small correction. For each binary separa-

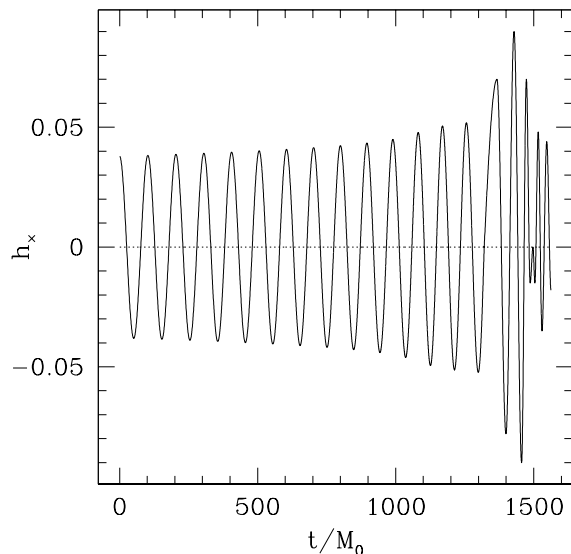


Fig. 10.6. A match of the late quasi-equilibrium inspiral wavetrain and the plunge and merger waveform for a binary of total rest mass $M_0 = 1.62M_0^{\text{max}}$. The merger of these binary results in immediate black hole formation (compare Section 10.3). Here $h_x = r_s/M_0\tilde{\gamma}_{xy}$, where r_s is the distance to the source. For $M_0 = 2 \times 1.5M_\odot$ and a distance to the source of 100 Mpc, the maximum amplitude of the metric perturbation is $\sim 5 \times 10^{-21}$. (Figure from Duez *et.al.* (2002).)

tion, the matter distribution can then be determined independently by the quasi-equilibrium methods of Section 9. These matter profiles, which satisfy the equations of quasi-stationary equilibrium, can then be inserted as matter sources into Einstein's equations. Evolving the gravitational fields yields the gravitational wave signal and luminosity, and hence the rate at which the system loses energy at each separation. Combining this luminosity dM/dt with the derivative of the binding energy M with respect to separation r yields the inspiral rate

$$\frac{dr}{dt} = \frac{dM/dt}{dM/dr}. \quad (10.22)$$

Integrating this equation yields the separation as a function of time, and accordingly the entire gravitational wave train.

Duez, Baumgarte and Shapiro (2001) implemented such a scheme for corotational binaries, based on the quasi-equilibrium models of Baumgarte *et.al.* (1998b) (see Section 9.2). In Duez *et.al.* (2002), these results were compared with those for an irrotational sequence, based on the models of Uryū, Shibata and Eriguchi (2000) (see Section 9.3). These simulations are illustrative only due to the small outer boundary radius which necessitated gravitational read-off inside the wave zone (compare Section 10.3). However, the method is quite promising. In Figure 10.5 we show such a gravitational wavetrain for an

irrotational binary.

For a given separation, the gravitational wave luminosity dM/dt is very similar for corotational and irrotational models²⁷, but since the binding energy of corotational models includes the spin kinetic energy of the individual stars, the absolute value of the corotational binding energy and hence $|dM/dr|$ is smaller than that of irrotational binaries. According to (10.22) this makes $|dr/dt|$ larger, meaning that the inspiral of corotational binaries proceeds faster than that of irrotational binaries.

Duez *et.al.* (2002) also point out that the entire gravitational wavetrain, from the slow inspiral to the ISCO and the subsequent plunge and merger, can be constructed by matching results from an quasi-adiabatic approximation of the inspiral and a dynamical simulation of the coalescence. An example, showing the last 13 orbits of the inspiral together with the plunge and merger leading to black hole formation (as obtained by Shibata and Uryū (2000a)), is shown in Figure 10.6.

11 Summary and Outlook

A search of the recent literature reveals the impressive progress that numerical relativity and the modeling of compact binaries has made in the past few years. New formulations of the initial value problem (Section 3) and the evolution equations (Section 4), new coordinate conditions and their implementations (Section 5) as well as new diagnostics (including the horizon finders described in Section 6) have led to several advances in the simulation of black holes and neutron stars. Recent breakthroughs include initial data for binary black holes (Section 7) and neutron stars (Section 9), evolution calculations for single and binary black holes (Section 8) and simulations of inspiraling and merging binary neutron stars (Section 10). Some results of astrophysical interest are density profiles of relativistic binary polytropes, the location of the ISCO in binary black holes and neutron stars, the stability properties of neutron stars in close binaries, cusp formation in irrotational binary neutron stars, the stabilizing effect of differential rotation in remnants of binary neutron star coalescence, and the first preliminary gravitational waveforms from coalescing binary neutron stars and black holes.

One of the long-standing goals of numerical relativity is the simulation of the coalescence of binary black holes. While this goal has not been achieved yet,

²⁷ As one might expect, since the gravitational wave emission is dominated by the matter density, which is fairly similar for the corotational and irrotational binaries, while matter current distributions play a less important role.

some preliminary calculations have been performed (Section 8.2). Moreover, with recent progress in the evolution of single black holes (Section 8.1), the simulation of binary black holes seems much more feasible than it did only a few years ago.

It is likely that most of the numerical results reported in this article will be revisited and improved. Some of these possible improvements have already been discussed in the corresponding Sections. For binary black hole initial data (Section 7) it would be desirable to gain a clearer understanding of why different approaches lead to different values of the ISCO. Specific calculations, some of which have already been initiated, include improvements of the thin-sandwich approach of Grandclément, Gourgoulhon and Bonazzola (2002) and the construction of binaries in circular orbit using Kerr-Schild or post-Newtonian background data, which would avoid the assumption of spatial conformal flatness. Avoiding this assumption may also be interesting for binary neutron star initial data (Section 9), in addition to extending sequences of irrotational binaries beyond cusp formation (see Section 9.3). The latter would provide better initial data for dynamical simulations of binary neutron star coalescence (Section 10.3), which could also be improved by using more sophisticated hydrodynamics algorithms. Other future improvements will be the inclusion of more realistic nuclear equations of state, magnetic fields, and possibly neutrino transport. Most of the results that we have discussed adopt the assumption of equal mass binaries, which eventually will also have to be generalized²⁸.

Almost all numerical results discussed in this article would benefit from increased accuracy, and most will need to be significantly more accurate before they can be useful in gravitational wave catalogs as discussed in Section 1. On uniform grids, two competing sources of numerical error are finite difference errors (due to coarse numerical grid resolution) and the location of outer boundaries (if they are imposed at too small a separation). Given the available computational resources and hence the size of the computational grid that can be afforded, a more or less suitable compromise has to be chosen between grid resolution and distance to the outer boundaries. In current simulations, this compromise still leads to significant error, in particular for gravitational wave forms (see Sections 10.3 and 10.4). Two improvements may be possible: instead of uniform grids, nested grids or adaptive mesh refinement (AMR) may be employed. While such techniques have been used in many other fields of computational physics as well as in lower-dimensional numerical relativity (see, e.g. Choptuik (1993)), they have been used sparingly in 3 + 1 numerical relativity so far (e.g. Brügmann (1996, 1999); New *et.al.* (2000); Jansen

²⁸ Note, however, that the mass of most neutron stars in neutron star binaries is close to $1.4 M_{\odot}$ (Thorsett and Chakrabarty, 1999), so that the assumption of equal mass seems quite adequate.

et.al. (2002)). In addition, the handling of the outer boundaries and gravitational radiation extraction could be refined. Some recent efforts include Bishop *et.al.* (1996); Abrahams *et.al.* (1998); Friedrich and Nagy (1999); Szilagyi *et.al.* (2000); Calabrese, Lehner and Tiglio (2002); Szilagyi, Schmidt and Winicour (2002).

Future effort will also be aimed in new directions. For example, it would be very desirable to model the late inspiral of binary black holes with a quasi-adiabatic approximation, similar to the binary neutron star calculations described in Section 10.4.

Lastly, we have only discussed binaries containing two black holes or two neutron stars, while black hole-neutron star binaries have so far been neglected (but see Miller (2001)). The inspiral, coalescence and merger of black hole-neutron star binaries, including the possible tidal disruption of the neutron star, seems like an extremely interesting subject and a promising source of gravitational radiation, and is likely to receive more attention in the future.

Acknowledgements

Over the years we have greatly benefitted from numerous discussions with many colleagues, including Andrew Abrahams, Greg Cook, Matt Duez, Mark Scheel, Masaru Shibata, Saul Teukolsky and Kip Thorne. We would like to thank the Visitors Program in the Numerical Simulation of Gravitational Wave Sources at Caltech for extending their hospitality while a portion of this review was being completed. This work was supported in part by NSF Grants PHY-0090310 and PHY-0205155 and NASA Grant NAG5-10781 at the University of Illinois at Urbana-Champaign and NSF Grant PHY-0139907 at Bowdoin College.

A Notation

We adopt the notation of Wald (1984), which is based on that of Misner, Thorne and Wheeler (1973). By convention, we also adopt the “fortran” convention in which the letters $a - h$ and $o - z$ are four-dimensional indices and run from 0 to 3, while the letters $i - n$ are three-dimensional indices that run from 1 to 3. We use geometrized units in which $c = G = 1$.

Unless stated differently, objects associated with the four-dimensional metric g_{ab} are denoted with a ⁽⁴⁾ in front of the symbol, objects associated with the conformally related (three-dimensional) metric $\bar{\gamma}_{ij}$ carry a bar, and only

objects related to the spatial metric γ_{ij} do not carry any decorations. For example, Γ_{jk}^i is associated with γ_{ij} , $\bar{\Gamma}_{jk}^i$ with $\bar{\gamma}_{ij}$, and ${}^{(4)}\Gamma_{jk}^i$ with g_{ab} . The covariant derivative operator is denoted with D_i and \bar{D}_i when compatible with the spatial metric and the conformally related metric, but with the nabla symbol ∇_a when compatible with the four-dimensional metric g_{ab} . We occasionally use Δ^{flat} for the flat scalar Laplace operator.

We denote the symmetric and antisymmetric parts of a tensor with brackets $()$ and $[\]$, for example

$$T_{(ab)} = \frac{1}{2}(T_{ab} + T_{ba}) \quad \text{and} \quad T_{[ab]} = \frac{1}{2}(T_{ab} - T_{ba}). \quad (\text{A.1})$$

Finally, we write a flat four-dimensional metric as η_{ab} (Minkowski spacetime) and a flat three-dimensional metric as η_{ij} .

B Solving the Vector Laplacian

In this appendix we discuss two approaches to solving the flat vectorial Poisson equation

$$(\Delta_L^{\text{flat}} W)^i = S^i, \quad (\text{B.1})$$

or, in Cartesian coordinates,

$$\partial^j \partial_j W_i + \frac{1}{3} \partial_i \partial^j W_j = S_i. \quad (\text{B.2})$$

We have encountered this operator in the momentum constraint (3.13) and (7.2), in the shift condition of the thin sandwich approach (3.28), in the minimal distortion condition (5.32), and in the Gamma-freezing condition (5.35).

Bowen and York (1980) suggest writing the vector W_i as a sum of a vector V_i and a gradient of a scalar U ,

$$W_i = V_i + \partial_i U. \quad (\text{B.3})$$

Inserting this into (B.2) yields

$$\partial^j \partial_j V_i + \frac{1}{3} \partial_i \partial^j V_j + \partial^j \partial_j \partial_i U + \frac{1}{3} \partial_i \partial^j \partial_j U = S_i. \quad (\text{B.4})$$

We can now choose U such that the two U terms in (B.4) cancel the second V_i term,

$$\partial^j \partial_j U = -\frac{1}{4} \partial_j V^j, \quad (\text{B.5})$$

so that (B.4) reduces to

$$\partial^j \partial_j V_i = S_i. \quad (\text{B.6})$$

We have hence rewritten the vector Poisson equation (B.2) as a set of four scalar Poisson equation for U and the components of V_i .

A second approach has been suggested by Shibata (1999c, see also Oohara, Nakamura and Shibata (1997), Appendix C), who used the ansatz

$$W_i = \frac{7}{8} P_i - \frac{1}{8} (\partial_i U + x^k \partial_i P_k). \quad (\text{B.7})$$

Inserting this into (B.2) yields

$$\frac{5}{6} \partial^j \partial_j P_i - \frac{1}{6} \partial_i \partial^j \partial_j U - \frac{1}{6} x^k \partial_i \partial^j \partial_j P_k = S_i \quad (\text{B.8})$$

If we now choose U so that it satisfies

$$\partial^j \partial_j U = -S_j x^j, \quad (\text{B.9})$$

then (B.8) reduces to

$$\frac{5}{6} \partial^j \partial_j P_i + \frac{1}{6} x^j \partial_i S_j - \frac{1}{6} x^j \partial_i \partial^k \partial_k P_j = \frac{5}{6} S_i \quad (\text{B.10})$$

and is solved by

$$\partial^j \partial_j P_i = S_i. \quad (\text{B.11})$$

The vector equation (B.2) has again been reduced to a set of four scalar Poisson equations, (B.9) and (B.11). While the approach of Shibata (1999c) seems a little more complicated, it has the advantage that the source terms in (B.9) and (B.11) are non-zero only where S_i is non-zero. In some cases (for example for the momentum constraint (3.13)) this may lead to compact sources, which can have advantages for numerical implementations (Grandclément *et.al.*, 2001).

In the approach of Bowen and York (1980), on the other hand, the source term of equation (B.5) is never compact. A third approach has been suggested by Oohara and Nakamura (1999). Numerical implementations (using spectral methods) of the three approaches have been compared by Grandclément *et.al.* (2001).

C Conformally Flat or Not?

Many numerical calculations, especially for the construction of initial data, assume the spatial metric to be conformally flat. Simultaneously, many authors have pointed out the limitations of conformal flatness, and have argued strongly against that simplification. Not all arguments have been correct, and it may be useful to briefly review those both in favor and against conformal flatness.

As we have seen in Section 3, conformal flatness greatly simplifies the initial value equations. Moreover, before the initial value equations can be solved, some form of the conformally related metric has to be chosen. In some cases educated guesses can be made (for example by choosing Kerr-Schild background data (Marronetti and Matzner, 2000) or by adopting a post-Newtonian metric instead of a flat conformally-related background metric as suggested in Section 7.3). However, in most cases it may not be clear what a better choice than conformal flatness might be.

In Section 3 we found that the dynamical degrees of freedom of the gravitational fields can be identified with parts of the conformally related spatial metric and the transverse-traceless part of the extrinsic curvature. This suggests that the assumption of conformal flatness and vanishing of \bar{A}_{ij}^{TT} may “minimize the gravitational radiation content” of a spatial slice Σ . This argument is not strictly true in general; for example it does not even hold for single rotating black holes. Rotating Kerr black holes, for example, which are stationary and do not emit any gravitational radiation, are not conformally flat²⁹. Similarly, conformally flat models of rotating black holes that are constructed in the Bowen-York formalism do contain gravitational radiation (Brandt and Seidel, 1995a,b, 1996; Gleiser *et.al.*, 1998, see also Jansen *et.al.* (2002)).

For rapidly rotating single neutron stars it has been shown that conformal flatness introduces an error of at most a few percent (Cook, Shapiro and Teukolsky, 1996). Similarly small discrepancies were found by Usui, Uryū and

²⁹ At least slices of constant Boyer-Linquist time are not conformally flat, nor are axisymmetric foliations that smoothly reduce to slices of constant Schwarzschild time in the Schwarzschild limit (Garat and Price, 2000)

Eriguchi (1999); Usui and Eriguchi (2002), who compared conformally flat binary neutron star models with models constructed under different assumptions. These small deviations are not surprising, since differences between a conformally flat metric and the “correct” metric appear at second post-Newtonian order (e.g. Rieth and Schäfer (1996)), which are the order of a few percent for neutron stars. It is therefore quite likely that, at least for neutron stars, the error arising from the conformal flatness assumption may be less than other errors typically expected in current simulations, including finite difference errors and effects from the poor handling of the outer boundaries.

Wilson and Mathews (1995, see also Wilson, Mathews and Marronetti (1996)) adopted the conformal flatness approximation in their simulations of binary neutron stars, and found that their neutron stars collapsed to black holes individually prior to merging. Since this result was very counter-intuitive, it was suspected that this surprising result was erroneous and an artifact caused by the assumption of conformal flatness. It was later found that these findings were indeed wrong and that they were caused by an error in the derivation of the equations (Flanagan, 1999; Mathews and Wilson, 2000) and not by conformal flatness.

It has been argued similarly that the disagreement between numerical (Cook, 1994; Baumgarte, 2000) and post-Newtonian (e.g. Damour, Jaranowski and Schäfer (2000)) values for the ISCO of binary black holes could be caused by the assumption of conformal flatness in the numerical calculations. However, the more recent numerical calculations of Grandclément, Gourgoulhon and Bonazzola (2002) achieve much better agreement with the post-Newtonian results, even though they also assume conformal flatness (also Blanchet (2002); Damour, Gourgoulhon and Grandclément (2002)). As we discussed in Section 7.3, it is more likely that the choice of initial value decomposition, which affects the transverse parts of the extrinsic curvature (see the discussion in Pfeiffer, Cook and Teukolsky (2002)), caused the earlier discrepancies. The good agreement between the numerical results of Grandclément, Gourgoulhon and Bonazzola (2002) and post-Newtonian results (Blanchet, 2002; Damour, Gourgoulhon and Grandclément, 2002) may even suggest that the assumption of conformal flatness is quite adequate for binary black hole models, at least as long as the spin of the individual black holes is not too large.

References

- Abrahams, A. M., Anderson, A., Choquet-Bruhat, Y., & York, J. W., Jr., 1995, *Phys. Rev. Lett.* **75**, 3377.
- Abrahams, A. M., & York, J. W., Jr., 1997, in *Relativistic Gravitation and Gravitational Radiation*, ed. J.-A. Marck and J.-P. Lasota (Cambridge University Press, Cambridge).

- Abrahams, A. M. *et. al.* (The Binary Black Hole Grand Challenge Alliance), 1998, *Phys. Rev. Lett.* **80**, 1812.
- Alcubierre, M., 1997, *Phys. Rev. D* **55**, 5981.
- Alcubierre, M., Allen, G., Brügmann, B., Landermann, G., Seidel, E., Suen, W.-M., & Tobias, M., 2000a, *Phys. Rev. D* **61**, 041501.
- Alcubierre, M., Allen, G., Brügmann, B., Seidel, E., & Suen, W.-M., 2000b, *Phys. Rev. D* **62**, 124011.
- Alcubierre, M., Bengert, W., Brügmann, B., Lanfermann, G., Nerges, L., Seidel, E., & Takahashi, R., 2001a, *Phys. Rev. Lett.* **87**, 271103.
- Alcubierre, M., Brandt, S., Brügmann, B., Gundlach, C., Massó, J., Seidel, E., & Walker, P., 2000c *Class. Quantum. Grav* **17**, 2159.
- Alcubierre, M., & Brügmann, B., 2001, *Phys. Rev. D* **63**, 104006.
- Alcubierre, M., Brügmann, B., Diener, P., Koppitz, M., Pollney, D., Seidel, E., & Takahashi, R., 2002, gr-qc/0206072.
- Alcubierre, M., Brügmann, B., Pollney, D., Seidel, E., & Takahashi, R., 2001b, *Phys. Rev. D* **64**, 061501.
- Alcubierre, M., Brügmann, B., Dramlitsch, T., Font, J. A., Papadopoulos, P., Seidel, E., Stergioulas, N., & Takahashi, R., 2000d, *Phys. Rev. D* **62**, 044034.
- Alcubierre, M., Brügmann, B., Miller, M., & Suen, W.-M., 1999, *Phys. Rev. D* **60**, 064017.
- Alcubierre, M., & Massó, J., 1998, *Phys. Rev. D* **57**, 4511.
- Alcubierre, M., & Schutz, B., 1994, *J. Comput. Phys.* **112**, 44.
- Alcubierre, M., & Seidel, E., 2002, private communication.
- Alvi, K., 2001, *Phys. Rev. D* **64**, 104020.
- Anderson, A., & York, J. W., Jr., 1999, *Phys. Rev. Lett.* **82**, 4384.
- Anderson, A., Choquet-Bruhat, Y., & York, J. W., Jr., 1997 *Topol. Methods Nonlinear Anal.* **10**, 353.
- Anninos, P., Bernstein, D., Brandt, S., Libson, J., Massó, J., Seidel, E., Smarr, L., Suen, W.-M., & Walker, P., 1995a, *Phys. Rev. Lett.* **74**, 630.
- Anninos, P., Daues, G., Massó, J., Seidel, E. & Suen, W.-M., 1995b, *Phys. Rev. D* **51**, 5562.
- Anninos, P., Camarda, K., Massó, J., Seidel, E., Suen, W.-M., & Towns, J., 1995c, *Phys. Rev. D* **52**, 2059.
- Anninos, P., Camarda, K., Libson, J., Massó, J., Seidel, E., & Suen, W.-M., 1998, *Phys. Rev. D* **58**, 024003.
- Anninos, P., Hobill, D., Seidel, E., Smarr, L., & Suen, W.-M., 1993, *Phys. Rev. Lett.* **71**, 2851.
- Arnold, R., Deser, S., & Misner, C. W., 1962, in *Gravitation: An Introduction to Current Research*, ed. L. Witten (Wiley, New York).
- Asada, H., 1998, *Phys. Rev. D* **57**, 7292.
- Ashtekar, A., Beetle, C., Dryer, O., Fairhurst, S., Krishnan, B., Lewandowski, J., & Wisniewski, J., 2000 *Phys. Rev. Lett.* **85**, 3564.
- Ashtekar, A., Beetle, C., & Fairhurst, S., 1999, *Class. Quant. Grav* **16**, L1.
- Baierlein, R. F., Sharp, D. H., & Wheeler, J. A., 1962, *Phys. Rev.* **126**, 1864.

- Baker, B. D., 2002, gr-qc/0205082.
- Baker, J., Brüggmann, B., Campanelli, M., Lousto, C. O., & Takahashi, R., 2001, *Phys. Rev. Lett* **87**, 121103.
- Baker, J., Campanelli, M., Lousto, C. O., & Takahashi, R., 2002, astro-ph/0202469.
- Balakrishna, J., Daues, G., Seidel, E., Suen, W.-M., Tobias, M., & Wang, E., 1996, *Class. Quantum Grav.* **13**, L135.
- Bardeen, J. M., & Piran, T., 1983, *Phys. Rep.* **96**, 205.
- Baumgarte, T. W., 2000, *Phys. Rev. D* **62**, 084020.
- Baumgarte, T. W., 2001, in *Astrophysical Sources for Ground-Based Gravitational Wave Detectors*, ed. J. M. Centrella, AIP Conference Proceedings 575.
- Baumgarte, T. W., Cook, G. B., Scheel, M. A., Shapiro, S. L., & Teukolsky, S. A., 1996, *Phys. Rev. D* **54**, 4849.
- Baumgarte, T. W., Cook, G. B., Scheel, M. A., Shapiro, S. L., & Teukolsky, S. A., 1997, *Phys. Rev. Lett.* **79**, 1182.
- Baumgarte, T. W., Cook, G. B., Scheel, M. A., Shapiro, S. L., & Teukolsky, S. A., 1998a, *Phys. Rev. D* **57**, 6181.
- Baumgarte, T. W., Cook, G. B., Scheel, M. A., Shapiro, S. L., & Teukolsky, S. A., 1998b, *Phys. Rev. D* **57**, 7299.
- Baumgarte, T. W., Hughes, S. A., & Shapiro, S. L., 1999, *Phys. Rev. D* **60**, 087501.
- Baumgarte, T. W., Hughes, S. A., Rezzolla, L., Shapiro, S. L., & Shibata, M., 1999, in *General Relativity and Relativistic Astrophysics – Eighth Canadian Conference*, edited by C. P. Burgess and R. C. Myers, AIP Conference Proceedings 493 (Melville, New York).
- Baumgarte, T. W., & Shapiro, S. L., 1999, *Phys. Rev. D* **59**, 024007.
- Baumgarte, T. W., Shapiro, S. L., & Abrahams, A. M., 1998, Lecture Notes on Numerical Relativity, unpublished.
- Baumgarte, T. W., Shapiro, S. L., & Shibata, M., 2000, *Astrophys. J.* **528**, L29.
- Baumgarte, T. W., Shapiro, S. L., & Teukolsky, S. A., 1995, *Astrophys. J.* **443**, 717.
- Beig, R., 1978, *Phys. Lett.* **69A**, 153.
- Bekenstein, J. D., 1999, in *Black Holes, Gravitational Radiation and the Universe*, edited by B. R. Iyer and B. Bhawal (Kluwer, Dordrecht).
- Berger, B. K., & Moncrief, V., 1993, *Phys. Rev. D* **48**, 4676.
- Bernstein, D., 1993, PhD thesis, University of Illinois at Urbana-Champaign.
- Bildsten, L., & Cutler, C., 1992, *Astrophys. J.* **400**, 175.
- Bishop, N. T., 1984, *Gen. Relativ. Gravit.* **16**, 589.
- Bishop, N. T., Gomez, R., Lehner, L., Szilagyi, B., Winicour, J., & Isaacson, R., 1996, *Phys. Rev. Lett.* **76**, 4303.
- Blackburn, J. K., & Detweiler, S., 1992, *Phys. Rev. D* **46**, 2318.
- Blanchet, L., 2002, gr-qc/0112056.
- Blanchet, L., Damour, T., Iyer, B. R., Will, C. M., & Wiseman, A. G., 1995,

- Phys. Rev. Lett.* **74**, 3515.
- Bona, C., & Massó, J., 1988, *Phys. Rev. D* **38**, 2419.
- Bona, C., & Massó, J., 1992, *Phys. Rev. Lett.* **68**, 1097.
- Bona, C., Massó, J., Seidel, E., & Stela, J., 1995, *Phys. Rev. Lett.* **75**, 600.
- Bona, C., Massó, J., Seidel, E., & Stela, J., 1997, *Phys. Rev. D* **56**, 3405.
- Bona, C., Massó, J., Seidel, E., & Walker, P., 1998, gr-qc/9804052.
- Bonazzola, S., Gourgoulhon, E., & Marck, J.-A., 1997, *Phys. Rev. D* **56**, 7740.
- Bonazzola, S., Gourgoulhon, E., & Marck, J.-A., 1999a, *Phys. Rev. Lett.* **82**, 892.
- Bonazzola, S., Gourgoulhon, E., & Marck, J.-A., 1999b, *J. Comput. Appl. Math.* **109**, 433.
- Bowen, J. M., 1982, *Gen. Rel. and Grav.* **14**, 1183.
- Bowen, J. M., & York, Jr., J. W., 1980, *Phys. Rev. D* **21**, 2047.
- Brady, P. R., Creighton, J. D. E., & Thorne, K. S., 1998, *Phys. Rev. D* **58**, 061501.
- Brandt, S. R., and Brügmann, B., 1997, *Phys. Rev. Lett.* **78**, 3606.
- Brandt, S., Correll, R., Gomez, R., Huq, M., Laguna, P., Lehner, L., Maronetti, P., Matzner, R. A., Neilsen, D., Pullin, J., Schnetter, E., Shoemaker, D., & Winicour, J., 2000, *Phys. Rev. Lett.* **85**, 5496.
- Brandt, S. R., & Seidel, E., 1995, *Phys. Rev. D* **52**, 856.
- Brandt, S. R., & Seidel, E., 1995, *Phys. Rev. D* **52**, 870.
- Brandt, S. R., & Seidel, E., 1996, *Phys. Rev. D* **54**, 1403.
- Brodbeck, O., Frittelli, S., Hübner, P., & Reula, O., 1999, *J. Math. Phys.* **40**, 909.
- Brügmann, B., 1996, *Phys. Rev D* **54**, 7361.
- Brügmann, B., 1999, *Int. J. Mod. Phys. D* **8**, 85.
- Buananno, A., & Damour, T., 2000, *Phys. Rev. D* **62**, 084036.
- Čadež, A., 1971, Ph.D. dissertation, University of North Carolina.
- Čadež, A., 1974, *Ann. Phys.* **83**, 449.
- Calabrese, G., Lehner, L., & Tiglio, M., 2002, *Phys. Rev. D* **65**, 104031.
- Calabrese, G., Pullin, J., Sarbach, O., & Tiglio, M., 2002, gr-qc/0205073.
- Chandrasekhar, S., 1992, *The Mathematical Theory of Black Holes* (Oxford University Press, New York).
- Christodoulou, C., 1970, *Phys. Rev. Lett.* **25**, 1596.
- Choquet-Bruhat, Y., 1952, *Acta. Math.* **88**, 141.
- Choquet-Bruhat, Y., 1962, in *Gravitation: An Introduction to Current Research*, ed. L. Witten (Wiley, New York).
- Choquet-Bruhat, Y., & Ruggeri, T., 1983, *Commun. Math. Phys.* **89**, 269.
- Choptuik, M. W., 1993, *Phys. Rev. Lett.* **70**, 9 (1993)
- Cook, G. B., 1990, Ph.D. thesis, University of North Carolina.
- Cook, G. B., 1991, *Phys. Rev. D* **44**, 2983.
- Cook, G. B., 1994, *Phys. Rev. D* **50**, 5025.
- Cook, G. B., 2000, *Living Rev. Rel.* **5**, 1.
- Cook, G. B., 2002, *Phys. Rev. D* **65**, 084003.
- Cook, G. B., Choptuik, M. W., Dubal, M. R., Klasky, S., Matzner, R. A., &

- Oliveira, S. R., 1993, *Phys. Rev. D* **47**, 1471.
- Cook, G. B., and Scheel, M. A., 1997, *Phys. Rev. D* **56**, 4775.
- Cook, G. B., Shapiro, S. L., & Teukolsky, 1994, *Astrophys. J.* **422**, 227.
- Cook, G. B., Shapiro, S. L., & Teukolsky, 1996, *Phys. Rev. D* **53**, 5533.
- Cook, G. B. *et. al.* (The Binary Black Hole Grand Challenge Alliance), 1998, *Phys. Rev. Lett.* **80**, 2512.
- Cook, G. B., & York, J. W., Jr, 1990, *Phys. Rev. D* **41**, 1077.
- Cutler, C., Apostolatos, T. A., Bilsten, L., Finn, L. S., Flanagan, E. E., Kennefick, D., Markovic, D. M., Ori, A., Poisson, E., Sussman, G. J., & Thorne, K. S., 1993, *Phys. Rev. Lett.* **70**, 2984.
- Damour, T., Gourgoulhon, E., & Grandclément, P., 2002 *Phys. Rev. D*, in press (also gr-qc/0204011).
- Damour, T., Jaranowski, P., & Schäfer, G., 2000, *Phys. Rev. D* **62**, 084011.
- Daues, G., 1996, Ph.D. thesis, Washington University.
- Detweiler, S., 1987, *Phys. Rev. D* **35**, 1095.
- De Donder, T., 1921, *La gravifique einsteinienne* (Gauthier-Villars, Paris).
- Dreyer, O., Krishnan, B., Schnetter, E., & Shoemaker, D., 2002 gr-qc/0206008.
- Duez, M. D., Engelhard, E. T., Fregeau, J. M., Hufferberger, K. M., & Shapiro, S. L., 1999, *Phys. Rev. D* **60**, 104024.
- Duez, M. D., Baumgarte, T. W., & Shapiro, S. L., 2001, *Phys. Rev. D* **63**, 084030.
- Duez, M. D., Baumgarte, T. W., Shapiro, S. L., Shibata, M., & Uryū, K., 2002, *Phys. Rev. D* **65**, 024016.
- Eardley, D. M., 1982, talk at *Numerical Astrophysics: a Symposium in Honor of James R. Wilson*, University of Illinois, unpublished.
- Eardley, D. M., 1998, *Phys. Rev. D* **57**, 2299.
- Eardley, D. M., & Smarr, L., 1979, *Phys. Rev. D* **19**, 2239.
- Einstein, A., and Rosen, N., 1935, *Phys. Rev.* **48**, 73.
- Eppey, K., 1977, *Phys. Rev. D* **16**, 1609.
- Estabrook, F. B., Wahlquist, H. D., Christensen, S., DeWitt, B., Smarr, L., & Tsiang, E., 1973, *Phys. Rev. D* **7**, 2814.
- Estabrook, F. B., Robinson, R. S., & Wahlquist, H. D., 1997, *Class. Quantum Grav.* **14**, 1237.
- Evans, C. R., 1984, Ph.D. thesis, University of Texas at Austin.
- Faber, J. A., & Rasio, F. A., 2002, *Phys. Rev. D* **65**, 084042.
- Fischer, A., & Marsden, J., 1972, *Comm. Math. Phys.* **28**, 1.
- Flanagan, E. E., 1999, *Phys. Rev. Lett.* **82**, 1354.
- Flanagan and S. A. Hughes, 1998, *Phys. Rev. D* **57**, 4566.
- Font, J. A., 2000, *Living Rev. Rel.* **3**, 2.
- Font, J. A., Goodale, T., Iyer, S., Miller, M., Rezzolla, L., Seidel, E., Stergioulas, N., Suen, W.-M., & Tobias, M., 2001, gr-qc/0110047.
- Font, J. A., Miller, M., Suen, W.-M., & Tobias, M., 2000, *Phys. Rev. D* **61**, 044011.
- Friedman, J. L., Uryū, K., & Shibata, M., 2002, *Phys. Rev. D* **65**, 064035.
- Friedrich, H., 1981a, *Proc. R. Soc. London* **A375**, 169.

- Friedrich, H., 1981b, *Proc. R. Soc. London* **A378**, 401.
- Friedrich, H., 1985, *Commun. Math. Phys.* **100**, 525.
- Friedrich, H., 1986a, *Commun. Math. Phys.* **103**, 35.
- Friedrich, H., 1986b, *Commun. Math. Phys.* **107**, 587.
- Friedrich, H., 1996, *Class. Quantum Grav* **13**, 1451.
- Friedrich, H., & Nagy, G., 1999, *Commun. Math. Phys.* **201**, 619.
- Frittelli, S., 1997, *Phys. Rev. D* **55**, 5992.
- Frittelli, S., & Gomez, R., 2000, *J. Math. Phys.* **41**, 5535
- Frittelli, S., & Reula, O., 1994, *Commun. Math. Phys* **166**, 221.
- Frittelli, S., & Reula, O., 1996, *Phys. Rev. Lett.* **76**, 4667.
- Frittelli, S., & Reula, O., 1999, *J. Math. Phys.* **40**, 5143.
- Garat, A., & Price, R. H., 2000, *Phys. Rev. D* **61**, 124011.
- Garfinkle, D., 2002 *Phys. Rev. D* **65**, 044029.
- Garfinkle, D., & Gundlach, C., 1999, *Class. Quantum Grav* **16**, 4111
- Garfinkle, D., Gundlach, C., Isenberg, J., & Ó Murchadha, N., 2000, *Class. Quantum Grav* **17**, 3899.
- Gleiser, R. J., Nicasio, C. O., Price, R. H., & Pullin, J., 1998, *Phys. Rev. D* **57**, 3401.
- Gomez, R., *et. al.* (The Binary Black Hole Grand Challenge Alliance), 1998, *Phys. Rev. Lett.* **80**, 3915.
- Gourgoulhon, E., 1998, gr-qc/9804054.
- Gourgoulhon, E., Grandclément, P., & Bonazzola, S., 2002, *Phys. Rev. D* **65**, 044020.
- Gourgoulhon, E., Grandclément, P., Taniguchi, K., Marck, J.-A., & Bonazzola, S., 2001, *Phys. Rev. D* **63**, 064029.
- Grandclément, P., Bonazzola, S., Gourgoulhon, E., & Marck, J.-A., 2001, *J. Comput. Phys.* **170**, 231.
- Grandclément, P., Gourgoulhon, E., & Bonazzola, S., 2002, *Phys. Rev. D* **65**, 044021.
- Gundlach, C., 1998, *Phys. Rev. D* **57**, 863.
- Gundlach, C., & Walker, P., 1999, *Class. Quantum Grav* **16**, 991.
- Hachisu, I., 1986, *Astrophys. J. Suppl.* **61**, 479.
- Hawking, S. W., & Ellis, G. F. R., 1973, *The Large Scale Structure of Space-time* (Cambridge University Press, Cambridge).
- Hawley, J. F., Smarr, L. L., & Wilson, J. R., 1984a, *Astrophys. J.* **277**, 296.
- Hawley, J. F., Smarr, L. L., & Wilson, J. R., 1984b, *Astrophys. J. Suppl.* **55**, 211.
- Hübner, P., 1996, *Phys. Rev. D* **53**, 701.
- Hughes, S., Keeton II, C. R., Walker, P., Walsh, K., Shapiro, S. L. & Teukolsky, S. A., 1994, *Phys. Rev. D* **49**, 4004.
- Huq, M. F., Chopuik, M. W., & Matzner, R. A., 2000, gr-qc/0002076.
- D’Inverno, R., 1992, *Introducing Einstein’s Relativity* (Oxford University Press, Oxford).
- Jackson, J. D., 1975, *Classical Electrodynamics*, Second Edition (Wiley, New York).

- Jansen, N., Diener, P., Khokhlov, A., & Novikov, I., 2002, gr-qc/0103109.
- Kemball, A. J., & Bishop, N. T., 1991, *Class. Quantum Grav.* **8**, 1361.
- Kelly, B., Laguna, P., Lockitch, K., Pullin, J., Schnetter, E., Shoemaker, D., & Tiglio, M., 2001 *Phys. Rev. D* **64**, 084013.
- Khokhlov, A. M., & Novikov, I. D., 2002, *Class. Quant. Grav.* **19**, 827.
- Kidder, L. E., Scheel, M. A., & Teukolsky, S. A., 2001 *Phys. Rev. D* **64**, 064017.
- Kidder, L. E., Scheel, M. A., Teukolsky, S. A., Carlson, E. D., & Cook, G. B., 2000, *Phys. Rev. D* **62**, 064017.
- Knapp, A. M., Walker, E. J., & Baumgarte, T. W., 2002, *Phys. Rev. D* **65**, 064031.
- Komar, A., 1959, *Phys. Rev.* **113**, 934.
- Kochanek, C. S., 1992, *Astrophys. J.* **398**, 234.
- Kulkarni, A. D., Shepley, L. C., & York, J. W., Jr., 1983, *Phys. Lett.* **96A**, 228.
- Laguna, P., 1999, *Phys. Rev. D* **60**, 084012.
- Laguna, P., & Shoemaker, D., 2002, gr-qc/0202105.
- Lai, D., Rasio, F. A., & Shapiro, 1993, *Astrophys. J. Suppl.* **88**, 205.
- Lanczos, C., 1922, *Phys. Z.* **23**, 537.
- Landry, W., & Teukolsky, S. A., 1999, gr-qc/9912004.
- Lehner, L., Huq, M., Anderson, M., Bonning, E., Schaefer, D., & Matzner, R., 2000, *Phys. Rev. D* **62**, 044037.
- Lehner, L., Huq, M., & Garrison, D., 2000, *Phys. Rev. D* **62**, 084016.
- Lehner, L., 2001, *Class. Quantum Grav.* **18**, R25.
- Libson, J., Massó, J., Seidel, E., & Suen, W.-M., 1996a, in *The Seventh Marcel Grossmann Meeting*, Proceedings, Stanford, California, 1994, ed. R. Jantzen *et.al.* (World Scientific, Singapore, 1996).
- Libson, J., Massó, J., Seidel, E., Suen, W.-M., & Walker, P., 1996b, *Phys. Rev. D* **53**, 4335.
- Lichnerowicz, A., 1944, *J. Math. Pure Appl.* **23**, 37.
- Lightman, A. P., Press, W. H., Price, R. H. & Teukolsky, S. A., 1975 *Problem Book in Relativity and Gravitation* (Princeton University Press, Princeton).
- Lindblom, L., & Scheel, M. A., 2002, gr-qc/0206035.
- Linquist, R. W., 1963, *J. Math. Phys.* **4**, 938.
- Lombardi, F. C., Rasio, F. A., & Shapiro, S. L., 1997, *Phys. Rev. D* **56**, 3416.
- Lousto, C. O., & Price, R. H., 1998, *Phys. Rev. D* **57**, 1073.
- Marronetti, P., Mathews, G. J., & Wilson, J. R., 1998, *Phys. Rev. D* **58** 107503.
- Marronetti, P., Mathews, G. J., & Wilson, J. R., 1999, *Phys. Rev. D* **60**, 087301.
- Marronetti, P., & Matzner, R. A., 2000, *Phys. Rev. Lett.* **85**, 5500.
- Marronetti, P., Huq, M., Laguna, P., Lehner, L., Matzner, R., & Shoemaker, D., 2000, *Phys. Rev. D* **62**, 024017.
- Marsa, R. L., & Choptuik, M. W., 1996, *Phys. Rev. D* **54**, 4929.
- Martí, J. M., Ibáñez, J. M., & Miralles, J. A., 1991, *Phys. Rev. D* **43**, 3794.
- Martí, J. M., & Müller, E., 1999, *Living Rev. Rel.* **2**, 3.
- Mathews, G. J., & Wilson, J. R., 2000, *Phys. Rev. D* **61**, 127304.

- Matzner, R. A., Huq, M. F., & Shoemaker, D., 1999, *Phys. Rev. D* **59**, 024015.
- Matzner, R. A., Seidel, E., Shapiro, S. L., Smarr, L., Suen, W.-M., Teukolsky, S. A., & Winicour, J., 1995, *Science* **270**, 941.
- May, M., & White, R. H., 1966, *Phys. Rev.* **141**, 1232.
- Miller, M., 2000, gr-qc/0008017.
- Miller, M., 2001, gr-qc/0106017.
- Misner, C. W., 1960, *Phys. Rev.* **118**, 1110.
- Misner, C. W., 1963, *Ann. Phys.* **24**, 102.
- Misner, C. W., Thorne, K., & Wheeler, J. A., 1973, *Gravitation* (Freeman, San Francisco).
- Nakamura, T., Kojima, Y., & Oohara, K., 1984, *Phys. Lett.* **106A**, 235.
- Nakamura, T., Kojima, Y., & Oohara, K., 1985, *Phys. Lett.* **107A**, 452.
- Nakamura, T., Oohara, K., & Kojima, Y., 1987, *Prog. Theor. Phys. Suppl.* **90**, 76.
- von Neumann, J., and Richtmyer, R. D., 1950, *J. Appl. Phys.* **21**, 232.
- New, K. C. B., 2002, gr-qc/0206041
- New, K. C. B., Choi, D.-I., Centrella, J. M., MacNeice, P., Huq, M. F., & Olson, K., *Phys. Rev. D* **62**, 084039.
- Norman, M. L., & Winkler, K.-H. A., 1986, in *Astrophysical Radiation Hydrodynamics*, edited by M. L. Norman and K.-H. A. Winkler (Reidel Publishing Company, Amsterdam).
- Oechslein, R., Rosswog, S., and Thielemann, F.-K., 2002, *Phys. Rev. D* **65**, 103005.
- Ó Murchadha, N., & York, Jr., J. W., 1974, *Phys. Rev. D* **10**, 2345.
- Oohara, K., & Nakamura, T., 1997, in *Relativistic Gravitation and Gravitational Radiation*, edited by J.-A. Marck and J.-P. Lasota (Cambridge Contemporary Astrophysics).
- Oohara, K., & Nakamura, T., 1999, *Prog. Theor. Phys. Suppl.* **136**, 270.
- Oohara, K., Nakamura, T., & Shibata, M., 1997, *Prog. Theor. Phys. Suppl.* **128**, 183.
- Oppenheimer, J. R., & Volkoff, G., 1939, *Phys. Rev.* **55**, 374.
- Ori, A., & Thorne, K. S., 2000, *Phys. Rev. D* **62**, 124022.
- Petrich, L. I., Shapiro, S. L., & Teukolsky, S. A., 1985, *Phys. Rev. D* **31**, 2459.
- Petrich, L. I., Shapiro, S. L., & Teukolsky, S. A., 1986, *Phys. Rev. D* **33**, 2100.
- Pfeiffer, H. P., Cook, G. B., & Teukolsky, S. A., 2002, gr-qc/0203085.
- Pfeiffer, H. P., Teukolsky, S. A., & Cook, G. B., 2000, *Phys. Rev. D* **62**, 104018.
- Press, W. H., Teukolsky, S. A., Vetterling, W. T., & Flannery, B. P., 1992 *Numerical Recipes* (Cambridge University Press, Cambridge).
- Price, R. H., & Pullin, J., 1994, *Phys. Rev. Lett.* **72**, 3297.
- van Putten, M. H. P. M., & Eardley, D. M., 1996, *Phys. Rev. D* **53**, 3056.
- Rasio, F. A., & Shapiro, S. L., 1999, *Class. Quant. Grav.* **16**, R1.
- Reula, O., 1998, *Living Rev. Rel.* **1**, 3.
- Rezzolla, L., Abrahams, A. M., Baumgarte, T. W., Cook, G. B., Scheel, M. A., Shapiro, S. L., & Teukolsky, S. A., 1998, *Phys. Rev. D* **57**, 1084.
- Rieth, R., & Schäfer, G., 1996, gr-qc/9603043.

- van Riper, K., 1979, *Astrophys. J.* **232**, 558.
- Sarbach, O., Calabrese, G., Pullin, J., & Tiglio, M., 2002, gr-qc/0205064.
- Scheel, M. A., 2000, talk given at the ITP Miniprogram *Colliding Black Holes: Mathematical Issues in Numerical Relativity*, January 10 - 28, 2000 (online version available at <http://doug-pc.itp.ucsb.edu/online/numrel00/scheel/>).
- Scheel, M. A., Shapiro, S. L., & Teukolsky, S. A., 1995a, *Phys. Rev. D* **51**, 4208.
- Scheel, M. A., Shapiro, S. L., & Teukolsky, S. A., 1995b, *Phys. Rev. D* **51**, 4236.
- Scheel, M. A., Baumgarte, T. W., Cook, G. B., Shapiro, S. L., & Teukolsky, S. A., 1997, *Phys. Rev. D* **56**, 6320.
- Scheel, M. A., Baumgarte, T. W., Cook, G. B., Shapiro, S. L., & Teukolsky, S. A., 1998, *Phys. Rev. D* **58**, 044020.
- Schinder, P. J., Bludman, S. A., & Piran, T., 1988, *Phys. Rev. D*, **37**, 2722.
- Schnetter, E., 2002, gr-qc/0206003.
- Schutz, B. F., 1980, *Geometrical Methods of Mathematical Physics* (Cambridge University Press, Cambridge).
- Seidel, E., & Suen, W.-M., 1992, *Phys. Rev. Lett.* **69**, 1845.
- Shapiro, S. L., 1998, *Phys. Rev. D* **57**, 908.
- Shapiro, S. L., 2000, *Astrophys. J.* **544**, 397.
- Shapiro, S. L. & Teukolsky, S. A., 1980, *Astrophys. J.* **235**, 199.
- Shapiro, S. L. & Teukolsky, S. A., 1985a, *Astrophys. J.* **298**, 34.
- Shapiro, S. L. & Teukolsky, S. A., 1985b, *Astrophys. J.* **298**, 58.
- Shapiro, S. L. & Teukolsky, S. A., 1986, *Astrophys. J.* **307**, 575.
- Shapiro, S. L. & Teukolsky, S. A., 1992, *Phys. Rev. D*, **45**, 2739.
- Shibata, M., 1997, *Phys. Rev. D* **55**, 2002.
- Shibata, M., 1998, *Phys. Rev. D* **58**, 024012.
- Shibata, M., 1999a, *Phys. Rev. D* **60**, 104052.
- Shibata, M., 1999b, *Prog. Theor. Phys.* **101**, 251.
- Shibata, M., 1999c, *Prog. Theor. Phys.* **101**, 1199.
- Shibata, M., Baumgarte, T. W., & Shapiro, S. L., 1998, *Phys. Rev. D*, **58**, 023002.
- Shibata, M., Baumgarte, T. W., & Shapiro, S. L., 2000a, *Phys. Rev. D*, **61**, 044012.
- Shibata, M., Baumgarte, T. W., & Shapiro, S. L., 2000b, *Astrophys. J.* **542**, 453.
- Shibata, M., & Nakamura, T., 1995, *Phys. Rev. D*, **52**, 5428.
- Shibata, M., & Uryū, K., 2000a, *Phys. Rev. D* **61**, 064001.
- Shibata, M., & Uryū, K., 2000b, *Phys. Rev. D* **62**, 087501.
- Shibata, M., & Uryū, K., 2001, *Phys. Rev. D* **64**, 104017.
- Shibata, M., & Uryū, K., 2002, *Prog. Theor. Phys.* **107**, 265.
- Shinkai, H., & Yoneda, G., 2000, *Class. Quantum Grav.* **17**, 4799.
- Shinkai, H., & Yoneda, G., 2002, *Class. Quant. Grav.* **19**, 1027.
- Shoemaker, D. M., Huq, M. F., & Matzner, R. A., 2000, *Phys. Rev. D* **62**, 124005.

- Smarr, L., 1975, Ph.D. thesis, University of Texas at Austin.
- Smarr, L., 1979, in *Sources of Gravitational Radiation*, ed. L. Smarr, (Cambridge University Press, Cambridge).
- Smarr, L., & York, Jr., J. W., 1978a, *Phys. Rev. D* **17**, 1945.
- Smarr, L., & York, Jr., J. W., 1978b, *Phys. Rev. D* **17**, 2529.
- Szilagyi, B., Gomez, R., Bishop, N. T., & Winicour, J., 2000, *Phys. Rev. D* **62**, 104006.
- Szilagyi, B., Schmidt, B., & Winicour, J., 2002, *Phys. Rev. D* **65**, 064015.
- Tagoshi, H., *et.al.* (The TAMA collaboration), 2001, *Phys. Rev. D* **63**, 062001.
- Teukolsky, S. A., 1982, *Phys. Rev. D* **26**, 745.
- Teukolsky, S. A., 1998, *Astrophys. J.* **504**, 442.
- Thorneburg, J., 1987, *Classical Quantum Grav.* **4**, 1119.
- Thorneburg, J., 1996, *Phys. Rev. D* **54**, 4899.
- Thorsett, S. E., & Chakrabarty, D., 1999, *Astrophys. J.* **512**, 288.
- Tichy, W., Brügmann, B., Cambanelli, M., & Diener, P., 2002, gr-qc/0207011.
- Tod, K. D., 1991, *Class. Quantum Grav.* **8**, L115.
- Unruh, W., 1984, as cited in Thorneburg (1987).
- Uryū, K., & Eriguchi, Y., 1998a, *Mon. Not. Royal. A. Soc.* **299**, 575.
- Uryū, K., & Eriguchi, Y., 1998b, *Astrophys. J. Suppl.* **118**, 563.
- Uryū, K., & Eriguchi, Y., 2000, *Phys. Rev. D* **61**, 124023.
- Uryū, K., Shibata, M., & Eriguchi, Y., 2000, *Phys. Rev. D* **62**, 104015.
- Usui, F., & Eriguchi, Y., 2002, *Phys. Rev. D* **65**, 064030.
- Usui, F., Uryū, K., & Eriguchi, Y., 2000, *Phys. Rev. D* **61**, 024039.
- Wald, R. M., 1984, *General Relativity* (University of Chicago Press, Chicago).
- Wald, R. M., and Iyer, V., 1991, *Phys. Rev. D* **44**, 3719.
- Whelan, J. T., & Romano, J. D., 1999 *Phys. Rev. D* **60**, 084009.
- Whelan, J. T., Krivan, W., & Price, R. H., 2000, *Class. Quant. Grav.* **17**, 4895.
- Wilson, J. R., 1972, *Astrophys. J.* **173**, 431.
- Wilson, J. R., & Mathews, G. J., 1989, in *Frontiers in Numerical Relativity* ed. C. R. Evans, L. S. Finn & D. W. Hobill, (Cambridge University Press, Cambridge).
- Wilson, J. R., & Mathews, G. J., 1995, *Phys. Rev. Lett.*, **75**, 4161.
- Wilson, J. R., Mathews, G. J., & Marronetti, P., 1996, *Phys. Rev. D* **54**, 1317.
- Yo, H.-J., Baumgarte, T. W., & Shapiro, S. L., 2001a, *Phys. Rev. D* **63**, 064035.
- Yo, H.-J., Baumgarte, T. W., & Shapiro, S. L., 2001b, *Phys. Rev. D* **64**, 124011.
- Yo, H.-J., Baumgarte, T. W., & Shapiro, S. L., 2002, *Phys. Rev. D*, in press (also gr-qc/0209066).
- Yoneda, G., & Shinkai, H., 1999, *Phys. Rev. Lett.* **82**, 263.
- Yoneda, G., & Shinkai, H., 2000, *Int. J. Mod. Phys. D* **9**, 13.
- Yoneda, G., & Shinkai, H., 2001a, *Class. Quantum Grav.* **18**, 441.
- Yoneda, G., & Shinkai, H., 2001b, *Phys. Rev. D* **63**, 124019.
- Yoneda, G., & Shinkai, H., 2002, gr-qc/0204002.
- York, Jr., J. W., 1971, *Phys. Rev. Lett.* **26**, 1656.

- York, Jr., J. W., 1972, *Phys. Rev. Lett.* **28**, 1082.
- York, Jr., J. W., 1973, *J. Math. Phys.* **14**, 456.
- York, Jr., J. W., 1979, in *Sources of Gravitational Radiation*, ed. L. Smarr (Cambridge University Press, Cambridge).
- York, Jr., J. W., 1980, in *Essays in General Relativity*, ed. F. J. Tipler (Academic, New York).
- York, Jr., J. W., 1989, in *Frontiers in Numerical Relativity* ed. C. R. Evans, L. S. Finn & D. W. Hobill, (Cambridge University Press, Cambridge).
- York, Jr., J. W., 1999, *Phys. Rev. Lett.* **82**, 1350.